INTERACTIONS OF MATRIX METALLOPROTEASE-1 WITH WATER-INSOLUBLE AGGREGATES OF ALPHA-SYNUCLEIN AND AMYLOID-BETA PEPTIDE

by

Sumaer Kamboj

A thesis submitted to the Faculty and the Board of Trustees of the Colorado School of Mines in partial fulfillment of the requirements for the degree of Doctor of Philosophy (Quantitative Biosciences and Engineering).

Golden, Colorado

Date _____

Signed: _____
Sumaer Kamboj

Signed: _____
Dr. Susanta K. Sarkar
Thesis Advisor

Golden, Colorado

Date _____

Signed: _____
Dr. John Spear
Professor and Director
Quantitative Biosciences and Engineering

ABSTRACT

Alzheimer's Disease (AD), Parkinson's Disease (PD), and Lewy body dementia (LBD) are the leading causes of neurodegeneration [1]. Currently, the cost of PD patient care is $52 billion per year and the cost of AD patient care is expected to reach $1.1 trillion per year by 2050. Irrespective of the debate about whether protein aggregates are the cause or consequence [2-4], ~50% of patients with AD [5], most patients with PD [6], and all patients with LBD [7] show intraneuronal cytoplasmic protein aggregates (primarily aSyn) that are toxic to cells [8]. In the context of AD, most patients also show extracellular aggregates with amyloid-beta peptide (Aβ), where Aβ is partially cleaved Aβ precursor protein (APP). As aggregates accumulate within or on neurons, the neurons are no longer able to function properly, leading to the symptoms associated with AD, PD, and LBD [9]. However, there is currently no drug to dissolve or degrade protein aggregates of neurodegeneration. Our central hypothesis is that it may be possible to degrade aggregates by leveraging broad-spectrum protease activity of matrix metalloproteases (MMPs). MMPs have diverse functions in the human body and are known to degrade extracellular matrix and non-matrix proteins [10, 11] and have intracellular functions [12]. Tetracycline and its derivatives, well-known inhibitors of MMPs [13], have shown therapeutic potential in AD [14] and PD [15]. MMPs can partially cleave aSyn [16-20], amyloid-beta precursor protein (APP) [21, 22], and Aβ [23-26]. This thesis takes the first step and presents experimental and computational results to show how MMP1, a collagenase in the 23-member human MMP family, interacts with aggregates of aSyn and Aβ at the single-molecule level. We have discussed how

molecular insights into MMP1 interactions with aggregates can inform virtual screening of drugs for potential targeting of MMPs for a specific substrate and function.

Briefly, we report quantification of allostery (communication between distant locations in the protein) using single-molecule measurements of MMP1 dynamics on aSyn- and Aβ-induced aggregates by calculating Forster Resonance Energy Transfer (FRET) between two dyes attached to the catalytic and hemopexin domains of MMP1. While MMP1 prefers open conformations with its two domains well-separated on aSyn, MMP1 prefers close conformations with the domains closer on Aβ. For both aSyn and Aβ, a two-state Poisson process describes the interdomain dynamics, where the two states and kinetic rates of interconversion between them are obtained from histograms and autocorrelations of FRET values. Since crystal structures of aSyn- and Aβ-bound MMP1 are not available, we performed molecular docking of MMP1 with aSyn and Aβ using ClusPro. We simulated MMP1 dynamics using different docking poses and matched the experimental and simulated interdomain dynamics to identify the appropriate poses. We used experimentally validated simulations to define conformational changes at the catalytic site and identify allosteric residues in the hemopexin domain having strong correlations with the residues at the catalytic site. We defined Shannon entropy to quantify MMP1 conformational fluctuations. We performed virtual screening of drugs against a site on selected aSyn- and Aβ-MMP1 binding poses and showed that lead molecules differ between free MMP1 and substrate-bound MMP1. In other words, virtual screening needs to take substrates into account for substrate-specific control of MMP1 activity. Molecular understanding of MMP1 interactions with

aSyn- and Aβ-induced aggregates may open up the possibility of degrading aggregates by targeting MMPs.

We have organized the thesis into five chapters. Chapter one provides an overview of the current literature and places the thesis in the context of neurodegeneration. Chapter two describes our novel and patented method for purifying recombinant aSyn in *E. coli* and forming aSyn-induced protein aggregates without using chromatography. Chapter three presents interactions of MMP1 with aSyn-induced aggregates at the single-molecule level. Chapter four presents interactions of MMP1 with Aβ-induced aggregates at the single-molecule level. At last, Chapter five summarizes the results in the thesis and proposes a framework for testing the relevance of the results in *C. elegans*.

TABLE OF CONTENTS

LIST Of FIGURES

LIST OF TABLES

TABLE OF COMMON ABBREVIATIONS

AD	Alzheimer’s Disease
APP	Amyloid-beta precursor protein
aSyn	Alpha-synuclein
Aβ	Amyloid-beta
FRET	Förster resonance energy transfer
IDP	Intrinsically disordered protein
kDa	kilo-Dalton
MMP	Matrix metalloprotease
NAC	non-amyloid component
PD	Parkinson’s Disease
PDB	Protein Data Bank
QBE	Quantitative Biosciences and Engineering
SDS-PAGE	sodium dodecylsulfate polyacrylamide gel electrophoresis
smFRET	single molecule Förster resonance energy transfer

ACKNOWLEDGMENTS

I would like to first thank my committee members for their patience and guidance as I navigated my graduate degree in Quantitative Biosciences and Engineering. I thank Prof. Klein-Seetharaman for her valuable support and teaching in all protein expression and characterization pursuits. I thank Prof. Leiderman for her knowledge, advice, and enthusiastic support as my committee chairperson. I thank Prof. Spear for his guidance and ability to always make time, even while running the first biology program on campus. I thank my Advisor, Prof. Susanta K. Sarkar for always making me a priority, pushing me to pursue new and challenging ideas, and for entertaining my hypotheses even when they were far-fetched.

Now for the people in my life who have been my support system, and have allowed this work to come to fruition, I say thanks. To my friends who have stuck by me, and always been available to blow off steam, get drinks, or go for a walk. To Athena for patiently waiting for and listening to me after a long night in the lab. To my QBE classmates who made the first few years of this program enjoyable, even during a pandemic. To my fellow labmates: Chase Harms, Derek Wright, and Dr. Lokender Kumar, all of whom aided in this research and have made this thesis a possibility.

Finally, I would like to thank my entire family, there is no way I would be physically/emotionally/mentally here without them. Their level of support and dedication to all of my pursuits has been unwavering and unquestioning.

To my entire family, who have always supported my academic pursuits

CHAPTER ONE

INTRODUCTION

1.1 Introduction

AD and PD are the leading causes of neurodegeneration [1]. Currently, the cost of PD patient care is $52 billion per year and the cost of AD patient care is expected to reach $1.1 trillion per year by 2050. The staggering cost of these diseases goes beyond monetary value and affects the quality of life for nearly 7 million Americans and their families [27, 28].

Irrespective of the debate about whether protein aggregates are the cause or consequence, ~50% of patients with AD and most patients with PD show protein aggregates that are toxic to cells [3, 5, 6]. In PD, the aggregates, referred to as Lewy Bodies, are intracellular and rich in the protein alpha-synuclein (aSyn). In AD, the aggregates, referred to as plaques, are extracellular and rich in amyloid-beta peptide (Aβ). A common feature of both protein aggregates is that they adopt a similar structure known as an amyloid fibril. The inherent presence of aggregates does not exclusively define all these diseases but may indicate a subset of each disease that shares a common trigger and neuropathology.

The aggregates share additional commonalities beyond the amyloid fibril structures. As aggregates accumulate within or on neurons, the neurons are no longer able to function properly, leading to the symptoms associated with AD and PD. The clearance and management of these aggregates are essential to preventing disease

progression. The overexpression of aSyn and Aβ peptide is associated with PD and AD respectively. There is a growing body of evidence that the proteolytic cleavage of Aβ peptide and aSyn aggregates plays an important role in understanding AD and PD. Matrix metalloproteases have shown capable of degrading these aggregates [9, 29].

Within our lab, we utilize biophysical methodologies to study matrix-metalloproteases (MMPS). Matrix-metalloproteases are a 23-member family of zinc-dependent enzymes with a conserved catalytic motif. MMPs are broad-spectrum proteases known to degrade extracellular matrix and non-matrix proteins [21, 22]. Inhibitors of MMPs, such as tetracycline and its derivatives, have shown therapeutic potential in AD and PD [12, 13]. MMP1 has shown the ability to cleave other non-extracellular substrates such as fibrin and bacterial biofilms [30, 31]. A major component of bacterial biofilms is an amyloid fibril structure [32]. If MMP-1 can breakdown bacterial biofilms, which are rich in amyloid fibrils, this may hint at its ability to break down the amyloid aggregates present in ~50% of AD and PD patients [6, 33]. Additionally, MMPs and their analogs have also been studied for their ability to cleave aSyn, APP, and Aβ [34, 35].

1.2 Protein structure and function

In this section, I discuss the structure and functions of the significant proteins for my study. In addition to the individual proteins, I also discuss amyloid fibrils because understanding their structure is also important to this study.

1.2.1 Matrix-metalloprotease

MMPs are a family of 23 broad-spectrum proteases known to degrade extracellular matrix and non-matrix proteins, but a growing body of evidence suggests proteolytic and non-proteolytic intracellular functions of MMPs [12] [10, 11]. MMPs are found throughout the body in the extracellular space, intracellular space, blood, intestine, brain, and can alter the blood-brain barrier [36-41]. MMPS can be found in the pro-form and activated forms in physiological conditions [42-47].

MMPs have a highly conserved catalytic domain and are often expressed as a zymogen with a pro domain blocking the catalytic site. Activation of MMP1 is achieved by removal of the pro domain by serine protease such as trypsin or other MMPs [48, 49]. MMP1 is a 447 amino acid protein consisting of 4 domains (PDB 4AUO) [50]. The domains are the pro-domain from 1-80, the catalytic domain from 81-241, the linker region 242-259, and the hemopexin domain 260-447.

1.2.2 Alpha-synuclein

The structure of monomeric full-length aSyn is categorized into three regions: the N-terminal region, the NAC region (non-amyloid component), and the C-terminal region. The N-terminal region (residues 1-60) contains seven 11 residue repeats that form a sequence predicted alpha-helix in the presence of synthetic membranes [51, 52]. The NAC region (residues 61-95) undergoes the conformation change necessary for the random coil to form a beta-sheet structure. The C-terminal region (residues 96-140) contains many acidic residues and is thought to be involved in inhibiting aggregation by interacting with the NAC region [53].

aSyn is considered an intrinsically disordered protein (IDP) as it lacks a stable three-dimensional structure in its native state. The monomeric form is known to adopt an alpha helix in the presence of artificial and natural membranes as well as forming a tetramer of alpha-helices [51, 54]. The instability of aSyn in its native state may contribute to its ability to perform the wide variety of functions mentioned previously, but it also contributes to its ability to misfold and produce “toxic” states [54]. During pathology, the native monomeric state undergoes a structural change leading to the stacking of beta-sheets characteristic of Lewy Bodies. It has been further suggested that misfolded aSyn may propagate through a prion-like mechanism [55].

aSyn was thought to be localized to the presynaptic terminal of neurons but since its discovery has been known to be produced in other non-neuronal cells such as red blood cells [56, 57]. aSyn has been implicated as a regulator of exocytosis through inhibition of phospholipase D2 and as a chaperone similar to cysteine string protein (CSPα), which indicates a role in SNARE-complex assembly [58, 59]. Studies in knock-out mice indicate the absence of aSyn leads to either an increase or inhibition in dopamine release indicating that aSyn has some role in dopamine release regulation [60-62]. Although the exact native function of aSyn is unknown it has been consistently indicated that aSyn has a role in dopamine metabolism, SNARE complex assembly in neurotransmitter release, and regulation of ATP synthase efficiency in the mitochondria [54, 63].

1.2.3 Amyloid-Beta peptide

Aβ peptide is a smaller fragment of a protein known as amyloid-beta precursor protein (APP). APP in a membrane protein expressed in many tissues including the

synapse of neurons. It has a structure consisting of a large glycosylated extracellular N-terminus and a smaller C-terminus. In humans, there are three other large proteins in the same gene family of APP. The other two are APP-related proteins known as APLP1 and APLP2 [64]. Different isoforms of APP exist ranging from 695 to 770 amino acids but the most abundant is 695 which is mainly expressed in neurons [65]. Other isoforms of 751 and 770 contain a serine protease inhibitor domain and are mainly expressed in platelets and peripheral cells [66, 67]. APP's function is not fully understood, but it is implicated in synapse formation, synapse repair, iron export, anterograde neuronal transport, and neuroplasticity [68-70].

During natural processing within the body, APP is secreted and cleaved into the extracellular space by multiple forms of secretase. If β-secretase is used followed by γ-secretase a 42 amino acid fragment of APP is yielded. This is what is known as Aβ peptide, and it is prone to aggregation. Methods of Aβ peptide aggregation, breakdown, and transport across the blood-brain barrier are being studied as part of AD pathology [71, 72]. Balancing the levels of Aβ peptide in the brain is achieved by proteolytic degradation and active transport out of the brain. There is a growing body of evidence that the proteolytic cleavage of Aβ peptide and its aggregate play an important role in understanding AD [73].

Aβ is commonly thought to be intrinsically disordered but it does have some distinguishable features. Using NMR-guided simulation researchers have suggested different conformational states of Aβ with the C-terminus being more structured. Between residues 31-34 and 38-41 a β-hairpin is found that reduces C-terminal

flexibility and may be responsible for the propensity 42 amino acid form of Aβ to form amyloids [74].

1.2.4 Amyloid fibrils

Amyloid fibrils (not to be confused with Aβ or APP) are a type of protein structure in which protein monomers misfold into β- sheets, and stack in an offset manner, forming a twisted fibril. Amyloid fibrils are commonly seen in bacterial biofilms, infectious prions, and aggregates involved in neurodegeneration [6, 28, 32, 33, 75, 76]. The amyloid fibril formation associated with neurodegeneration is currently thought to be caused by overexpression, genetic mutation, or cleavage of precursors affecting the stability of the protein in its native form [71, 72]. A common protein found in PD and AD amyloid aggregates is aSyn and there is evidence that the C-terminal truncation of aSyn by protease leads to aggregation and fibril formation [77]. In PD and some forms of dementia, these fibrils can aggregate into larger intracellular structures known as Lewy Bodies. Aβ peptide is mainly implicated in the amyloid fibril formation into extracellular plaques associated with AD [33].

1.3 Role of MMPs in the aggregation of aSyn and Aβ

Proteolytic degradation of aSyn and Aβ peptide is not only important to their aggregated forms but their monomeric forms as well. The cleavage, or lack of cleavage, of monomeric aSyn and Aβ peptide by proteases has implications in aggregate formation. Both intracellular and extracellular proteolytic systems take part in the cleavage of aSyn [78]. Dysfunctions of the two major functionally interconnected intracellular proteolytic systems, i.e., the ubiquitin-proteasome system and the

autophagy-lysosome pathway, are considered to be involved in the cleavage and aggregation of aSyn [78-80]. For example, the lysosomal protease cathepsin D (CathD) can degrade aSyn, and mutations in CathD encoding the gene *ctsd* lead to the misprocessing of aSyn [81]. Trypsin and trypsin-like serine proteases in the brain are also potential candidates for degrading aSyn [82]. Proteases such as calpains and neurosin have also been shown to cleave aSyn [83-87]. In particular, neurosin (also known as human kallikrein-6, KLK6, Zyme, and Protease M) is a serine protease expressed throughout the body, including the central nervous system (CNS), and can cleave aSyn [88, 89]. However, in the context of AD and PD, proteases of particular interest are those that partially cleave aSyn and APP to create amyloidogenic fragments. There are two critical enzymes for the partial cleavage of aSyn and APP. First, asparaginyl endopeptidase (AEP or legumain), an age-dependent lysosomal cysteine protease that cleaves protein substrates on the C-terminal side, can cleave aSyn at N103 and APP [88, 90]. Second, matrix metalloproteases (MMPs), which are also known to degrade many components of the extracellular matrix, including age-dependent collagen, can cleave aSyn and APP [16-20]. Of the MMP family, MMP1, MMP2, MMP3, MMP9, and MT1-MMP can partially cleave aSyn, with the possible cleavage sites for MMP1, MMP3, and MMP9 identified [18, 19]. The implication of MMPs in neurodegeneration is significant. Tetracycline and its derivatives, known to inhibit MMPs, have shown therapeutic potential in AD and PD [13, 18, 19].

1.4 Interactions of MMPs with aSyn and Aβ *in vivo*

MMP3, a member of the MMP family, cleaves aSyn *in vivo* and colocalizes with aSyn in Lewy bodies in the postmortem brains of PD patients [14]. Although aSyn is a

cytosolic protein, extracellular aSyn is found in cerebrospinal fluid, blood plasma and can be secreted by normal cells [15, 91-95]. Similarly, both extracellular and intracellular Aβ have been implicated in AD [96-98]. Since MMPs can be activated in intracellular and extracellular spaces, MMPs are likely to interact with aSyn to produce aSyn fragments, leading to aggregation. MMPs are also implicated in PD and AD by their contributions to blood-brain barrier breakdown and association with dementia [21, 22].

Another emerging thought is that Lewy body pathology can start in the enteric nervous system (ENS) of the gut and spread to the central nervous system (CNS) [99]. Holmqvist et al. showed that aSyn in the human PD brain lysate and recombinant aSyn could be transported from the gut to the brain via the vagus nerve and reach the dorsal motor nucleus of the vagus in the brainstem after injection into the intestinal wall of rats [100]. Hoffmann et al. provided a mechanism of trafficking extracellular aSyn aggregates into intracellular space and initiating aggregation of endogenous aSyn [101]. This phenomenon is not just for aSyn; Harach et al. showed a reduction of Aβ peptide (amyloidogenic fragment of APP) pathology in transgenic mouse models in the absence of gut microbiota [102]. The presence of aSyn and Aβ in the intestine has been reported [103, 104]. MMPs represent a suitable target for bringing these aggregate-prone proteins and their amyloidogenic fragments into contact with neurons in the enteric nervous system (ENS). Mechanisms underlying intestinal wall breakdown are unclear, with hypotheses ranging from tissue hypoxia to collagen breakdown by MMPs [102]. However, collagen degradation by MMPs must be an integral part of intestinal tissue breakdown because collagen is a major component of the extracellular matrix in the intestines as it is in most tissues [104].

1.5 Allosteric control of proteases

Proteases can be viewed as a system of loosely structured amino acids that communicate by electrostatic forces to alter peptide bonds in other proteins. The electrostatic forces within a protease serve to change the conformation of the protease. The movement of a protease during activity is known as its conformational dynamics and involves the entire protease, not just the catalytic pocket. MMPs have a highly conserved catalytic pocket, yet each protease can act on different substrates such as MMP1 on triple-helical type collagen and MMP9 on gelatin [50, 105, 106]. The difference in substate specificity suggests that domains away from the catalytic site are essential for substrate recognition. Recently, Kumar et al. has shown that MMP1 is capable of allosteric communication between the hemopexin and catalytic domain even in the absence of a linker region [78]. Identification of the allosteric residues involved in the substrate recognition and conformation dynamics of MMP1 could serve as a target for ligand binding to modulate the activity of MMP1.

1.6 Thesis Objective

Within our lab, we have used an interdisciplinary approach to study MMP1 on a variety of substrates including collagen, fibrinogen, fibrin, and bacterial biofilms [30, 31, 48, 78]. Characterization of MMP1 conformational dynamics on each substrate using single-molecule Förster resonance energy transfer has shown that the open conformation of MMP1 is functionally relevant and that the magnitude of conformational change is unique to each substrate. This suggests substrate-specific allosteric communication between the hemopexin domain and catalytic domain of MMP1.

The objective of this thesis is to elucidate the mechanics of MMP1 activity on aggregates present in PD and AD. Our interdisciplinary approach will utilize single-molecule biophysical methods, molecular dynamic simulations, virtual screening of lead molecules, and ensemble biochemical assays. We hypothesize that we can allosterically control fragmentation of aSyn and Aβ by MMPs to modulate aggregation and possibly degrade existing aggregates.

CHAPTER TWO [1]

PURIFICATION OF ALPHA SYNUCLEIN WITHOUT CHROMATOGRAPHY

2.1 Introduction

More than 50% of patients with AD and almost all patients with PD show Lewy bodies, intraneuronal cytoplasmic protein aggregates[6]. The typical protein in Lewy bodies that may be causally related to the etiology of AD and PD is aSyn [107]. The physiological functions of aSyn remain unclear, but its primary localization in the cytoplasm of mainly neuronal cells and at presynaptic terminals implies a role in neuronal function [108-113]. Also, aSyn is associated with the distal reserve pool of synaptic vesicles [110, 114, 115]. An overexpression or knockout of aSyn leads to dysregulation of synaptic transmission [60, 116-119]. These studies suggest that aSyn plays an essential role in regulating neurotransmitter release and synaptic function [120]. A growing body of evidence from *in vitro* and *in vivo* genetic, biochemical, and biophysical studies suggests that aSyn oligomerization and fibrillation play a central role in Lewy body pathologies, including AD and PD [121-124]. There is evidence that the C-terminal truncation of aSyn by proteases leads to protein aggregation and Lewy body formation. Research has shown that asparaginyl endopeptidase (AEP) causes partial cleavage of aSyn [90]. A growing body of evidence suggests that matrix metalloproteases can also partially cleave aSyn [16-20]. However, the mechanisms and cellular pathways leading to neurodegeneration caused by aSyn-induced aggregation remain unknown despite many biophysical studies [125-127]. Addressing these

[1] Content in this chapter was formally published in [183]; see Appendix A

knowledge gaps will require further biophysical and biochemical studies of the mechanisms underlying protein aggregation induced by aSyn [128], which in turn would require purified aSyn as well as a model of protein aggregates.

Since the first identification of synucleins in the human brain and *E. coli* based purification of recombinant synucleins in 1994, several reports of recombinant purification have been reported for aSyn [52, 112, 129-131]. Protein purification usually requires time-consuming and expensive steps of chromatography to separate proteins of interest from other proteins. Generally, cell lysate goes through a series of purification steps such as precipitation by ammonium sulfate or acid, ion exchange, and size exclusion chromatography [132]. For higher specificity, several fusion strategies such as the glutathione S-transferase (GST) system and the chitin-binding domain-intein system are also useful [133, 134]. Leveraging periplasmic localization of expressed aSyn in *E. coli*, a shorter purification protocol was developed [135]. For NMR studies, isotopically labeled aSyn was purified in *E. coli* [136]. For the delivery of aSyn inside cells, researchers have purified Tat-fused recombinant aSyn in *E. coli* [137]. For purifying aSyn with post-translational modifications, Gerding et al. reported a method of purifying aSyn with 3-nitrotyrosine in *E. coli* [138]. These methods can provide good purity and homogeneity of purified aSyn within three or more days. Recombinant aSyn purified in *E. coli* has enabled many *in vitro* and even *in vivo* studies revealing many insights into structure-function relationships of aSyn. Based on these studies using recombinant protein, aSyn is generally considered a "natively unfolded" ~14.6 kDa monomer that can form secondary α-helical structures upon binding to lipid membranes and detergents [51, 52].

In contrast to the monomeric form of recombinant protein, aSyn purified from the human brain, live human cells, neuronal and non-neuronal cell lines predominantly show a "natively folded" ~58 kDa tetrameric form [139, 140]. The additional efforts to purify aSyn destabilize the tetrameric forms, leading to the monomeric form [139]. Several factors affect aSyn studies, including purification, denaturing step, high concentration, and post-translational modification [132, 139, 141]. To enable further studies of the structure-function relationships of aSyn, we developed a quick and inexpensive method of aSyn purification in *E. coli*. We describe a method to purify untagged recombinant aSyn within 24 h, where we have eliminated chromatography from aSyn purification by exploiting the propensity of aSyn to form aggregates. Our core technology involves "self-purification" of aSyn, which is possible because aSyn leads to aggregation of *E. coli* proteins leaving soluble full-length aSyn. As a result, we obtained purified aSyn and a model of aSyn-induced protein aggregates to enable further biochemical and biophysical studies.

2.2 aSyn is toxic for *E. coli*

We expressed full-length recombinant human aSyn with 140 residues in *E. coli*. The molecular weight of full-length aSyn is ~14.5 kDa. We inserted the sequence of aSyn into the pET11a vector between NdeI (N-terminal) and HindIII (C-terminal) restriction sites. We transformed the plasmid into Rosetta (DE3) pLysS competent *E. coli* strain for aSyn expression. The aSyn in the plasmid is under the control of the lac operator, and as such, we induced aSyn expression using 1 mM Isopropyl β-d-1-thiogalactopyranoside (IPTG) at Optical Density (OD_{600})=0.17.

As shown in Figure 2.1a, IPTG-induced production of aSyn inhibited *E. coli* growth. However, *E. coli* growth was unaffected for 2.5 h after IPTG induction, indicating a threshold concentration of intracellular aSyn for toxicity. We used Congo red, a stain for amyloid [142, 143], to test if aSyn production after IPTG induction leads to amyloid formation. *E. coli* culture without IPTG induction served as the control.

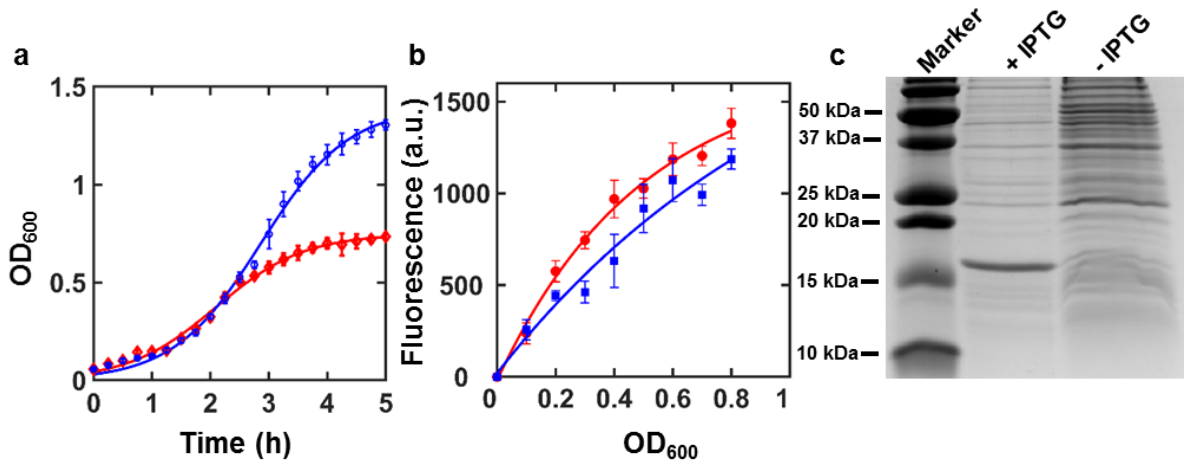

Figure 2.1. Expression of aSyn in *E. coli*. (**a**) Growth of *E. coli* strain Rosetta(DE3) pLysS with (red diamond) and without (blue circle) IPTG. The data are fitted to the logistic equation for bacterial growth, $a/[1+b\exp(-kt/60)]$, with (solid red line) and without (solid blue line); the best-fit parameters are $a=0.8\pm0.1$ (with IPTG), 1.5 ± 0.3 (without IPTG); $b=15\pm22$ (with IPTG), 24 ± 26 (without IPTG); $k=1.3\pm0.7$ (with IPTG), 1.0 ± 0.5 (without IPTG). The error bars represent the standard deviations of three replicates. Induction by IPTG produces aSyn, which is toxic for *E. coli,* as indicated by the reduced growth in the presence of IPTG. (**b**) Fluorescence from Congo red stain between 565 nm and 650 nm with (solid red circle) and without (solid blue circle) IPTG upon excitation at 470 nm. The data are fitted to the equation, $d-e\times\exp(-f\times x)$, with (solid red line) and without (solid blue line); the best-fit parameters are $d=1680\pm178$ (with IPTG), 2263 ± 1479 (without IPTG); $e=1699\pm161$(with IPTG), 2243 ± 1430 (without IPTG); $f=2.01\pm0.42$ (with IPTG), 0.91 ± 0.52 (without IPTG). The error bars represent standard deviations of four replicates. (**c**) Expression of aSyn with and without IPTG. A comparison of protein expression with and without IPTG showed a band at ~16 kDa due to aSyn, which is higher than the actual mass. Published reports have shown aSyn indicating a little higher weight in SDS PAGE and expected value in SDS PAGE [18, 19, 135, 136, 144].

We incubated cultures with and without IPTG induction at the same OD, centrifuged and discarded supernatant, reconstituted the cells in water, and measured

Congo red fluorescence (see methods for detailed procedure). Figure 2.1b shows that Congo red fluorescence with IPTG induction is higher than without IPTG induction at each OD, suggesting that aSyn forms amyloid inside *E. coli* and reduces growth observed in Figure 2.1a. The supernatant of centrifuged cell lysates was analyzed using SDS PAGE, as shown in Figure 2.1c, which showed a band at ~15 kDa due to aSyn after induction with IPTG. As a negative control, cells without IPTG induction did not produce aSyn. A comparison of protein bands with and without IPTG revealed that *E. coli* protein bands were of lighter intensity when aSyn was present. In combination with the reduced growth (Figure 2.1a), this observation suggests that aSyn leads to aggregation of *E. coli* proteins and causes toxicity.

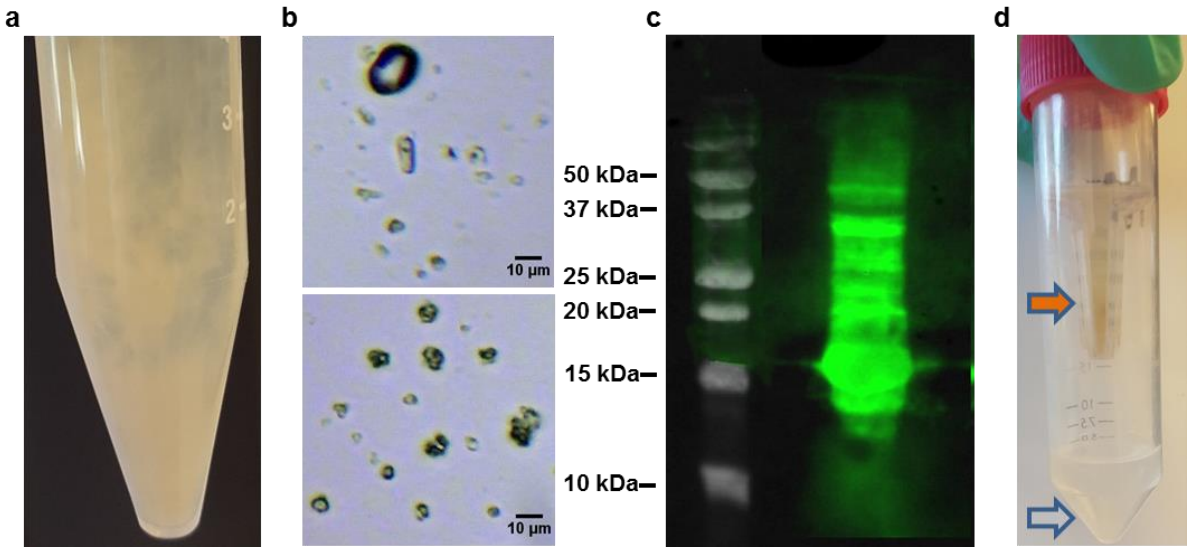

Figure 2.2. Aggregation of aSyn. (**a**) Water-insoluble but suspended aggregates of *E. coli* proteins induced by aSyn. (**b**) Examples of structures observed under a light microscope. (**c**) WB of the soluble proteins in Figure 2.2a shows oligomers of aSyn. A calorimetric image (gray bands on the left) of the molecular weight markers superimposed with the WB image. (**d**) Centrifugation of the soluble proteins in Figure 2.2a using a 30 kDa cut-off filter leads to further aggregation (orange arrow) and a clear flow-through (gray arrow). Filtration of the flow-through using a 10 kDa cut-off centrifugation filter gives purified aSyn.

2.3 aSyn leads to water-suspended structures

We observed that the centrifugation of *E. coli* lysate at 10000 rpm in a 15 mL tube led to water-suspended structures that did not precipitate (Figure 2.2a). The water-suspended structures revealed different morphologies under a light microscope (Figure 2.2b). The soluble portion in Figure 2.2a showed oligomers in Western blot (WB) imaging (Figure 2.2c). The soluble part's centrifugation using a 30 kDa filter led to further aggregation and a clear flow-through (Figure 2.2d). Interestingly, the water-suspended structures did not form in a 50 mL tube, suggesting that centrifugal force in combination with narrow diameters leads to the water-suspended aggregation.

2.4 aSyn induced aggregation of *E. coli* proteins facilitates purification

We leveraged the aggregation of *E. coli* proteins to purify aSyn without chromatography using 30 kDa and 10 kDa centrifugation filters (Figure 2.3a). The identity of aSyn was confirmed by WB using an anti-aSyn antibody (Figure 2.3b). We used the Bradford assay to quantify the concentration of purified aSyn. Figure 2.3c shows the standard curve generated using bovine serum albumin (BSA), where the red symbol indicates the data point due to aSyn. We obtained ~60 μg of purified aSyn in solution from 500 mL culture within 24 h. Note that we got a lower amount of purified aSyn because we also formed aggregates of native *E. coli* proteins leveraging the amyloidogenic property of aSyn. Also, we performed mass spectrometry and Edman sequencing of purified aSyn at the Tufts Core Facility (Figure 2.4). Mass spectrometry (Figure 2.3d) confirmed that the purified aSyn did not have higher molecular weight contamination. Further, Edman sequencing confirmed the first seven amino acids to be MDVFMKG as expected (see Figure 2.4).

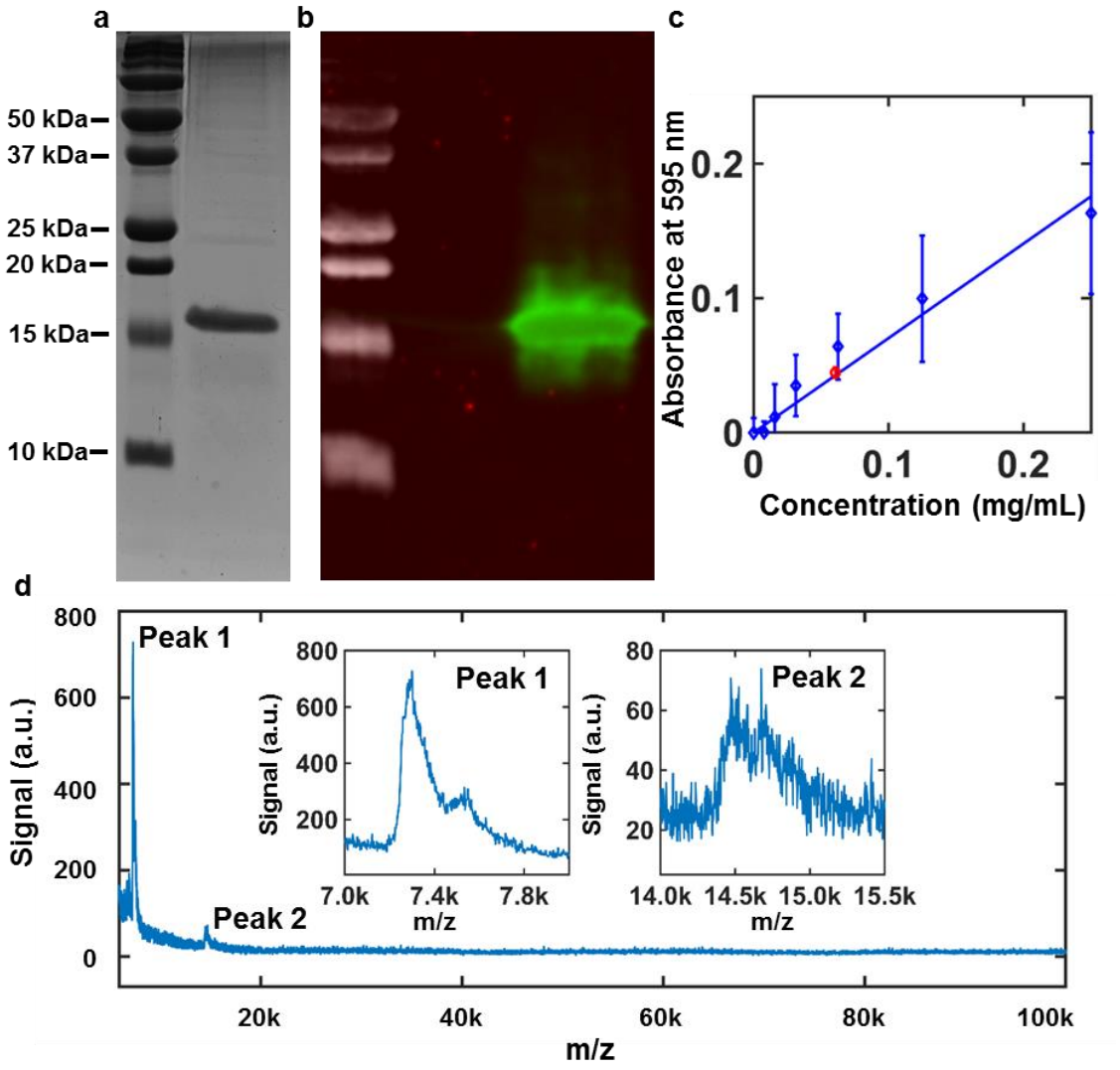

Figure 2.3. Purification, quantification, and identification of aSyn. (**a**) Purified aSyn. Left lane: molecular weight marker; right lane: aSyn. (**b**) WB using an anti-aSyn antibody. A calorimetric image (gray bands on the left) of the markers superimposed with the WB image. (**c**) Bradford standard curve generated using BSA as the standard. The solid line is the best fit to a line $y = ax$; the best-fit parameter is $a = 0.7 \pm 0.1$ (standard deviation of three replicates). The red square due to aSyn results in a concentration of ~60 μg/mL. (**d**) MALDI-TOF mass spectrum of aSyn shows the purity of aSyn. Two peaks appear due to aSyn: peak 1 (7.3 kDa and 7.5 kDa) and peak 2 (14.5 kDa and 14.7 kDa).

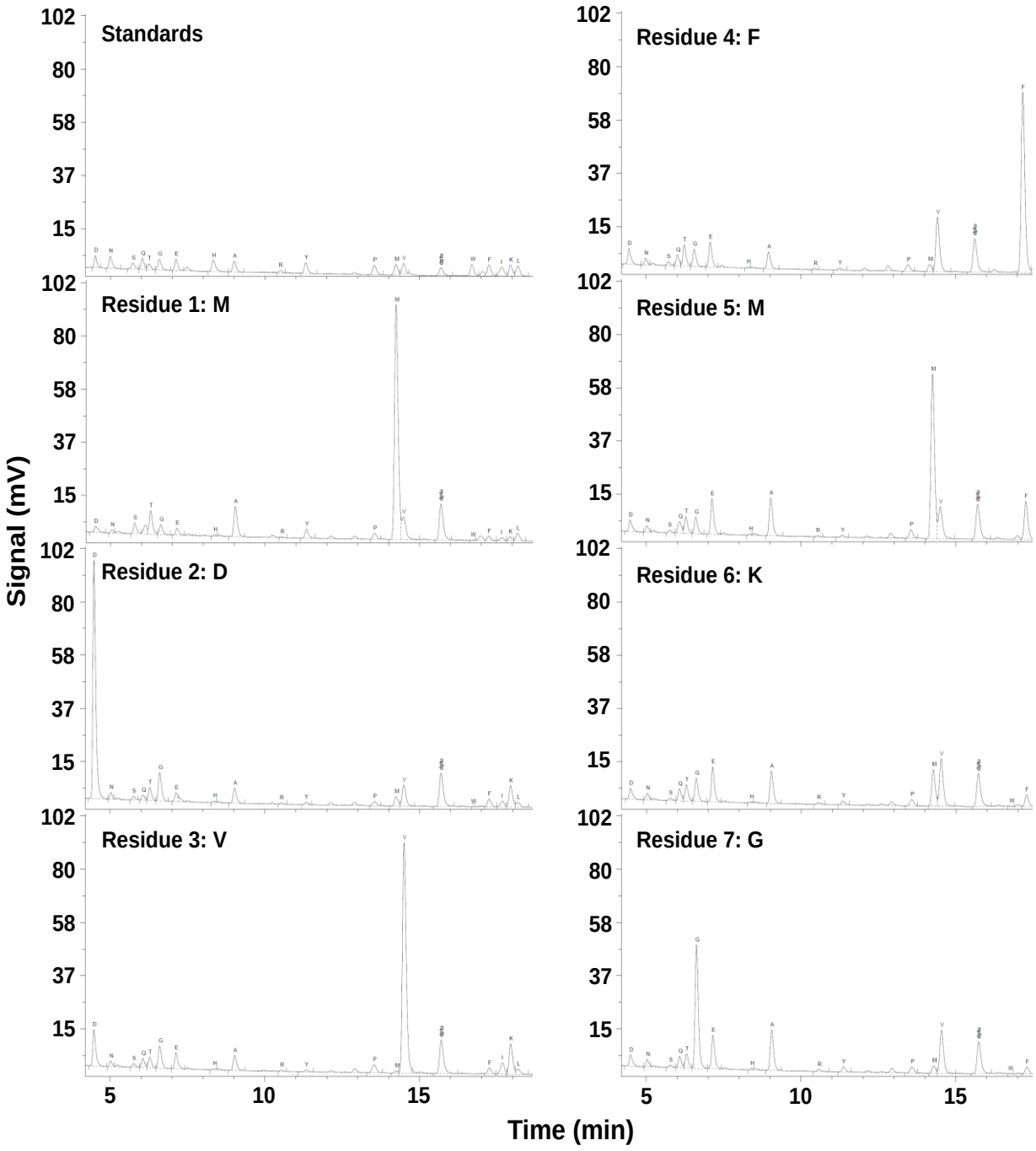

Figure 2.4. Edman sequencing of purified aSyn. The first seven residues from the N-terminal are MDVFMKG. Edman sequencing was performed at the Tufts Core Facility, Tufts Medical School, 136 Harrison Ave, Boston, MA 02111.

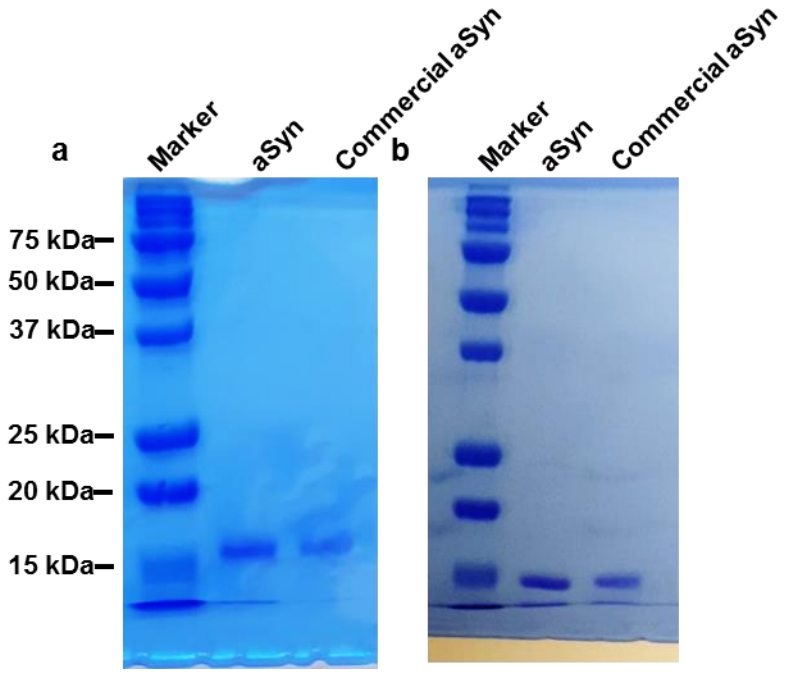

Figure 2.5. The molecular weight of aSyn in SDS PAGE depends on the experimental conditions. (**a**) SDS PAGE with the running buffer at pH=8.2. (**b**) SDS PAGE with the running buffer at pH=9.2.

2.5 Higher molecular weight of aSyn in the SDS PAGE profile is likely due to the running buffer pH

Figure 2.5 shows that aSyn can indicate different molecular weights in SDS PAGE depending on the experimental conditions. Highly acidic and low molecular weight (less than 15 kDa) proteins often run abnormally in SDS-PAGE [145]. aSyn with a pI of 5.1 and a molecular weight of 14.6 kDa shows abnormal electrophoretic mobility and appears to have a molecular weight of ~17 kDa [144]. The literature indicates that aSyn can run at a higher molecular weight and the expected molecular weight in SDS PAGE [18, 19, 135, 136, 144]. To resolve the issue, we changed the running buffer's pH (Figure 2.5) and kept the other conditions the same, which resulted in a shift in the position of aSyn relative to the 15 kDa band. The commercial aSyn (Abcam, Cat#

ab218818) and purified aSyn using our method show similar band positions (Figure 2.5).

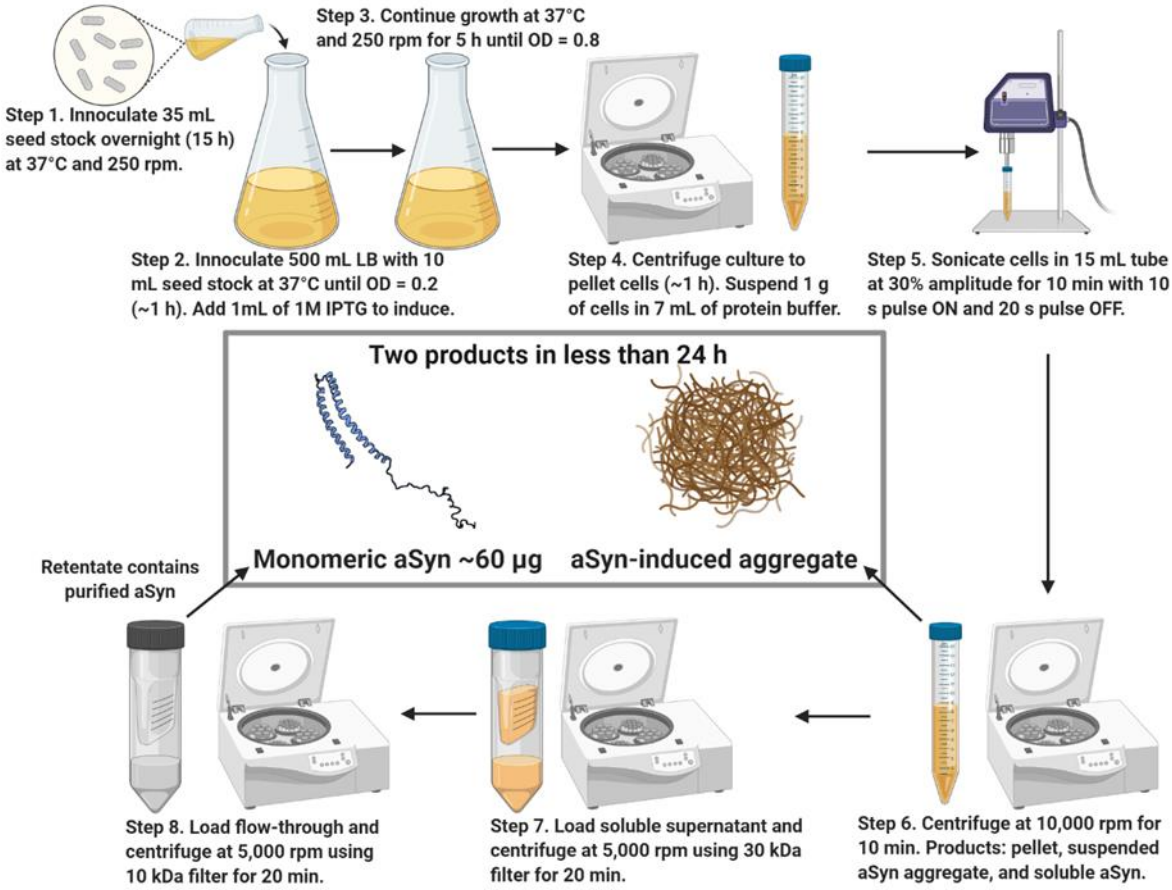

Figure 2.6. Flowchart of aSyn purification in *E. coli*. In less than 24 h, it is possible to purify 60 µg of monomeric aSyn from 500 mL of *E. coli* culture and obtain aSyn-induced aggregates. The use of sonication in Step 5 and narrow diameter tubes (15 mL) for centrifugation in Step 6 are essential for optimum results. Created with BioRender.com.

2.6 Summary

In conclusion, we have developed an inexpensive and quick method of purifying ~60 µg recombinant aSyn in *E. coli* within 24 h. Figure 2.6 shows the purification flowchart. Two critical steps are the use of sonication and narrow diameter tubes for

centrifugation. We compared purified aSyn with commercially available aSyn (Figure 2.5), which shows comparable purity. In the future, functional studies such as fibrillation kinetics are needed to compare the two sources of aSyn. In contrast to the chromatography-free method in this paper, chromatography-based purification techniques using denaturing agents take a few days. Recently, Gerding et al. reported a process of purifying ~1 mg of aSyn in *E. coli* [138] involving two chromatographic steps. Although 60 μg of aSyn from 500 mL of *E. coli* culture in our paper is significantly less than ~1 mg of aSyn, aSyn-induced protein aggregates are an important byproduct of the method described in this paper. The formation of aggregates enables chromatography-free purification but leads to the lower yield of purified aSyn. These aggregates might be useful as a model of Lewy bodies. However, further studies are needed to confirm whether or not these aggregates can be used as a model of Lewy bodies. The production of aSyn-induced aggregates, in addition to purified monomeric aSyn, is unique relative to the prior reports on aSyn purification. We have observed oligomers of aSyn in the supernatant, as suggested by WB (Figure 2.2c), before purifying monomeric aSyn (Figure 2.3a). The observation of aSyn oligomers is consistent with previous reports of the tetrameric form of aSyn [139, 140]. However, we cannot conclude the precise stoichiometry because we did not perform any size exclusion chromatography in our chromatography-free method. The dramatic substrate promiscuity of aSyn enables purification and affects *E. coli* growth (Figure 2.1a). We used Congo red [142, 143] to detect amyloid formation in *E. coli* (Figure 2.1b). In the future, we need functional data to define the toxicity of purified aSyn in mammalian cells and animal models. To this end, thioflavin T (ThT) [142] and 1-anilinonaphthalene-8-sulfonic acid (ANS) [143] may

provide additional information about fibrillation. Both ThT and ANS emit enhanced fluorescence upon binding fibrils. However, ThT emits stronger fluorescence upon binding the β-sheet conformation of amyloid fibrils. In contrast, ANS emits enhanced fluorescence upon attaching to hydrophobic surfaces. As such, ANS is a suitable probe for partially unfolded protein conformations. The promiscuity of aSyn with *E. coli* proteins suggests that aSyn may have more physiological implications than neurodegeneration.

2.7 Methods

In this section, I discuss the methods used within the chapter. This includes a method of purification for aSyn beginning with the insertion if the plasmid and ending with a purified protein as well as an aggregate rich in aSyn.

2.7.1 Transformation of the plasmid

MDVFMKGLSKAKEGVVAAAEKTKQGVAEAAGKTKEGVLYV

GSKTKEGVVHGVATVAEKTKEQVTNVGGAVVTGVTAVAQKT

VEGAGSIAAATGFVKKDQLGKNEEGAPQEGILEDMPVDPDNE

AYEMPSEEGYQDYEPEA

Figure 2.7. Amino acid sequence for aSyn. Contains 140 residues.

ATGGACGTTTTCATGAAAGGTCTGTCTAAAGCTAAAGAAGG
TGTTGTTGCTGCTGCTGAAAAAACCAAACAGGGTGTTGCTG
AAGCTGCTGGTAAAACCAAAGAAGGTGTTCTGTACGTTGGT
TCTAAAACCAAAGAAGGTGTTGTTCACGGTGTTGCTACCGTT
GCTGAAAAAACCAAAGAACAGGTTACCAACGTTGGTGGTGC
TGTTGTTACCGGTGTTACCGCTGTTGCTCAGAAAACCGTTGA
AGGTGCTGGTTCTATCGCTGCTGCTACCGGTTTCGTTAAAAA
AGACCAGCTGGGTAAAAACGAAGAAGGTGCTCCGCAGGAA
GGTATCCTGGAAGACATGCCGGTTGACCCGGACAACGAAGC
TTACGAAATGCCGTCTGAAGAAGGTTACCAGGACTACGAAC
CGGAAGCT

Figure 2.8. The DNA sequence for aSyn. The sequence was optimized for expression in E.coli K12 using Java Codon Adaption Tool (JCat) [146].

The plasmid contains the DNA sequence for 140-residue wild type aSyn inserted into the pET11a vector between NdeI (N-terminal) and HindIII (C-terminal) restriction sites. We transformed the plasmid into Rosetta (DE3) pLysS *E. coli* (Millipore, Cat# 70956-4). We thawed 50 µL of cells on ice. 10 µL of plasmid at 100 ng/mL concentration was added to the cells and kept on ice for 30 min. We transferred cells to a hot water bath at 42ºC for 45 s and moved back to the ice for 5 min. 950 µL of super optimal broth with catabolite repression (SOC) media (Sigma-Aldrich, Cat# S1797) was added to the cells and incubated for 2 h at 37ºC. We spread 100 µL of growth on a plate containing ImMedia Amp Blue (Invitrogen, Cat# 45-0038) and allowed it to grow for 48 h. After 48 h, we selected one colony of *E.coli* and transferred it into 35 mL of Luria Broth (LB) media with 35 µL of ampicillin at 100 mg/mL concentration and 35 µL of chloramphenicol at 34 mg/mL concentration. Cells were grown for an additional 16 h until OD_{600} reached 1.5. To make glycerol stock, we added 800 µL of *E. coli* culture to 500 µL of 50% glycerol (Sigma-Aldrich, Cat# G5516) and stored it at -80ºC.

2.7.2 Growth of Rosetta (DE3) pLysS cells.

We prepared 35 mL of seed culture in LB media (Sigma-Aldrich L7658) from 3 mL of E. coli cells' glycerol stocks. We added 35 µL of ampicillin at 100 mg/mL concentration and 35 µL of chloramphenicol at 34 mg/mL concentration. The seed culture was grown overnight for 15 h in shaker-incubator at 37ºC with 250 rpm orbital agitation until growth reached OD_{600}=1.8. 10 mL of the seed culture was added to 500 mL sterile LB media with the same final concentrations of antibiotics in two 1 L conical flat-bottom glass flasks and grown at 37ºC with 250 rpm orbital agitation. After the growth reached OD_{600}=0.2, we induced the cells in one flask with 500 µL of 1 M IPTG (ChemCruz, Cat# SC-202185B). The cells in the other flask were not induced with IPTG to serve as the negative control. After induction, we grew cells in both flasks for 5 h in the incubator-shaker at 37ºC with 250 rpm orbital agitation. We measured OD using a cell density meter (WPA Biowave, Model# C0800) to quantify the growth, as shown in Figure 2.1a. The cells were harvested and centrifuged in 15 mL centrifuge tubes at 10000 rpm for 10 minutes using a fixed angle centrifuge (Sorvall Lynx 4000 centrifuge with F12-6X500 rotor, Cat# 75006580). Note that LB media was sterilized by an autoclave (Panasonic, Model# MLS-3781L) following the preset liquid sterilization program (121°C for 15 min).

2.7.3 Congo red staining

We collected 1 mL of culture from 500 mL stock cultures with and without IPTG at OD_{600} = 0.1, 0.2, 0.3, 0.4, 0.5, 0.6, 0.7, and 0.8. We centrifuged the 1 mL cultures in 1.5 mL microcentrifuge tubes at 10,000 rpm for 10 min. After discarding the

supernatant, we added 200 µL of Congo Red stain (Abcam, Cat# ab150663) to each sample tube and vortexed briefly to reconstitute cells. We incubated the cells with Congo red at 37°C for 10 min. After centrifugation of samples at 10,000 rpm for 10 min, we removed the excess stain and added 500 uL of deionized water to reconstitute the stained *E. coli* by brief vortexing. We loaded 200 µL of each sample into thin-walled PCR tubes and measured the Congo red emission in the range of 565 - 650 nm using a DeNovix Fluorometer QFX with 470 nm excitation (Figure 2.1b).

2.7.4 Cell lysis and SDS PAGE to confirm the expression of aSyn

We took 10 mL of each growth and disrupted the cells using a sonicator (Branson Digital Sonifier, Model# BBT16031593A) at 30% amplitude for 10 min with a sequence of 10 s pulse ON and 20 s pulse OFF. We centrifuged the cell lysates and collected the supernatant containing soluble proteins. These samples were prepared for SDS PAGE by 1:1 dilution in sample buffer with β-mercaptoethanol (Sigma-Aldrich, Cat# M3148) made from 2x Laemmli buffer (Biorad, Cat# 161-0737). We boiled the samples with the dye for 10 min and loaded 30 µL of each sample into the wells of a 15% polyacrylamide gel. The gel was run in 1X SDS running buffer at 70 V and 40 mA. After 30 min, we increased the voltage to 120 V and allowed the gel to run for an additional 1 h. Gels were removed from the running tank and stained in 100 mL of stain prepared using 30% ethanol, 10% acetic acid, and 0.5% Coomassie Brilliant Blue R-250 (Biorad, Cat# 161-0436). The gel was stained for 2 h and washed twice in DI water to remove excess dye, followed by destaining in 200 mL of 30% ethanol and 10% acetic acid for 18 h. We imaged the gel using an imager (Figure 2.1c).

2.7.5 Protein aggregation induced by centrifugation in narrow tubes

We caused protein aggregation by aSyn as an integral part of our purification to pull down native *E.coli* proteins, and aSyn effectively self-purified itself. We reconstituted 1 g cell pellet in 6 mL of protein buffer (50 mM Tris, 100 mM NaCl, pH 9.0) in a 15 mL tube and disrupted the cells using a sonicator as described before. The step of lysate centrifugation in a 15 mL tube at 10000 rpm for 10 min is critical. After centrifugation, we observed water-suspended structures. Note that the water-suspended structures did not form when we centrifuged the cell lysate in a 50 mL tube. We also noted that even with longer centrifugation, the water-suspended structures did not precipitate and form a pellet at the bottom of the tube and remained suspended in solution. The suspended insoluble structures were highly viscous and cohesive, like mucus. We could pull out the structures from the solution using a 1 mL pipet tip. The soluble supernatant was filtered using a 30 kDa Amicon filter tube (Millipore, Cat# UFC903024) at 5000 rpm for 20 min. The flow-through of filtration was then loaded into a 10 kDa Amicon filter tube (Millipore, Cat# ACS501012) and centrifuged at 5000 rpm for 20 min. The retentate from this filtration contained purified aSyn, which we checked using a 15% SDS PAGE. The gel was run at 150 V for 10 min and then 200 V for 45 min. After purification, we obtained 1 mL of ~60 µg/mL aSyn. We quantified the protein concentration using the Bradford assay (Figure 2.3c).

2.7.6 Identification of aSyn using Western blotting

We ran the SDS PAGE of the protein sample in 15% polyacrylamide gel as before. Then, we transferred the proteins to a nitrocellulose membrane using the Trans-Blot Turbo transfer system (Biorad, Model# 170-4155). Then, we dipped the membrane

with transferred proteins into 30 mL of blocking buffer (skim milk) and placed it on a shaker for 2 h. After removing the blocking buffer, we added the primary anti-aSyn antibody (Abcam, Cat# 138501) to a final concentration of 0.5 µg/mL in 10 ml of blocking buffer and placed it on a shaker at 4ºC for 16 h. After removing the primary antibody solution, we washed the blot 3 times with 30 mL of protein buffer (50 mM Tris, 100 mM NaCl, pH 9.0). After washing, we dipped the membrane into 50 mL of the secondary antibody (Bosterbio, Cat# BA1054) at a final concentration of 0.5 µg/mL for 2 h. We removed the secondary antibody solution and rewashed the blot with 30 mL of protein buffer. 12 ml of the chemiluminescent substrate (Biorad, Clarity Western ECL substrate, Cat# 170-5060) was added to the blot and imaged using a Biorad imager.

2.7.7 Identification and quantification of aSyn

In addition to WB, we confirmed the identity of purified aSyn using mass spectroscopy and Edman sequencing performed by the Tufts Core Facility at Tufts Medical School. Edman sequencing, developed by Pehr Edman, is a standard method of identifying proteins [147-149]. Although mass spectrometry provides one way of identifying proteins, the sequence obtained from Edman sequencing offers a complementary and more direct confirmation of the protein's identity. Figure 2.4 shows the first seven residues of purified aSyn, confirming the identity of aSyn and validating the purification method. To quantify aSyn concentration, we used Pierce Detergent Compatible Bradford Assay Kit (Thermo Scientific, Cat# 23246). We created a standard curve using BSA with known concentrations in protein buffer (100 mM NaCl, 50 mM Tris, pH 9.0). We measured the absorbance at 595 nm and subtracted the blank

reading without BSA from the absorbance measurements. We fitted the standard curve to a linear model and quantified the aSyn concentration from the best-fit parameters.

CHAPTER THREE

INTERACTIONS OF MATRIX METALLOPROTEASES WITH ALPHA-SYNUCLEIN

3.1 Introduction

Lewy bodies, intraneuronal cytoplasmic protein aggregates, are commonly observed in the brains of patients with AD and PD [6]. ASyn is often the common protein detected in Lewy bodies observed in AD and PD [107]. An established body of evidence shows that the C-terminal truncation of aSyn by proteases leads to protein aggregation and Lewy body formation. Both intracellular and extracellular proteolytic systems take part in the breakup of aSyn [6]. As such, partial cleavage of aSyn explains aggregates due to fibrillation and misfolding [107, 150, 151]. Although aggregates could be a consequence instead of a cause of AD and PD, the uncontrolled aggregation will lead to cell death and worsening of effects[2, 152-154]. As such, there is a need to find ways to degrade existing aggregates.

A growing body of evidence shows that matrix metalloproteases (MMPs) can partially cleave aSyn [16-20]. Prior reports have shown that MMP1, MMP2, MMP3, MMP9, and MT1-MMP can partially cleave aSyn with the possible cleavage sites identified [18, 19]. MMPs are broad-spectrum proteases known to degrade extracellular matrix and non-matrix proteins, but a growing body of evidence suggests proteolytic and non-proteolytic intracellular functions of MMPs [10, 18, 19]. MMPs are found in extracellular space, intracellular space, blood, intestine, brain, and can alter the blood-brain barrier [11, 12, 36-39]. The implication of MMPs in partial cleavage of aSyn is significant because tetracycline, a well-known inhibitor of MMPs, has shown therapeutic

potential in AD and PD [13, 40, 41, 155, 156]. The broad-spectrum protease activity of MMPs not only leads to aSyn-induced aggregation, but it might also be useful in degrading existing aSyn-induced aggregates. However, it is not clear yet how MMPs might affect aSyn-induced aggregates, which are water-insoluble and challenging to study using standard biochemical assays. To this end, we have developed a single-molecule tracking approach and weight-based activity assay to study water-soluble MMPs interacting with water-insoluble substrates. As such, it is possible to study MMP activity on aSyn-induced aggregates at the single-molecule level.

However, it is not enough to know how MMP interacts with aggregates. Due to broad-spectrum activity, targeting MMPs for improving human health is challenging because MMPs interact with and degrade many proteins in the human body [14]. Due to such diverse functions, any drug used for inhibiting MMPs results in adverse side effects [15]. As such, there is only one FDA-approved MMP inhibitor (doxycycline hyclate) [157]. To circumvent this problem, we need to understand the mechanisms behind diverse functions. The catalytic domain sequence of MMP1 is very similar to other MMPs in the family. However, the hemopexin domain sequence varies [158, 159], suggesting that differences in activity and substrate specificity among MMPs are due to allosteric (distant from the catalytic site) communications [160, 161]. Recently, we reported activity-dependent MMP1 dynamics and allosteric communications on type-1 collagen fibrils and fibrin [11, 162]. We showed that functionally relevant conformations have the catalytic and hemopexin domains of MMP1 well-separated. These open conformations often accompany a larger catalytic pocket opening of MMP1, enabling the substrates to get closer to the active site of MMP1. Building on this, we have the

opportunity to define dynamics and allosteric communications of MMP1 on aSyn-induced aggregates.

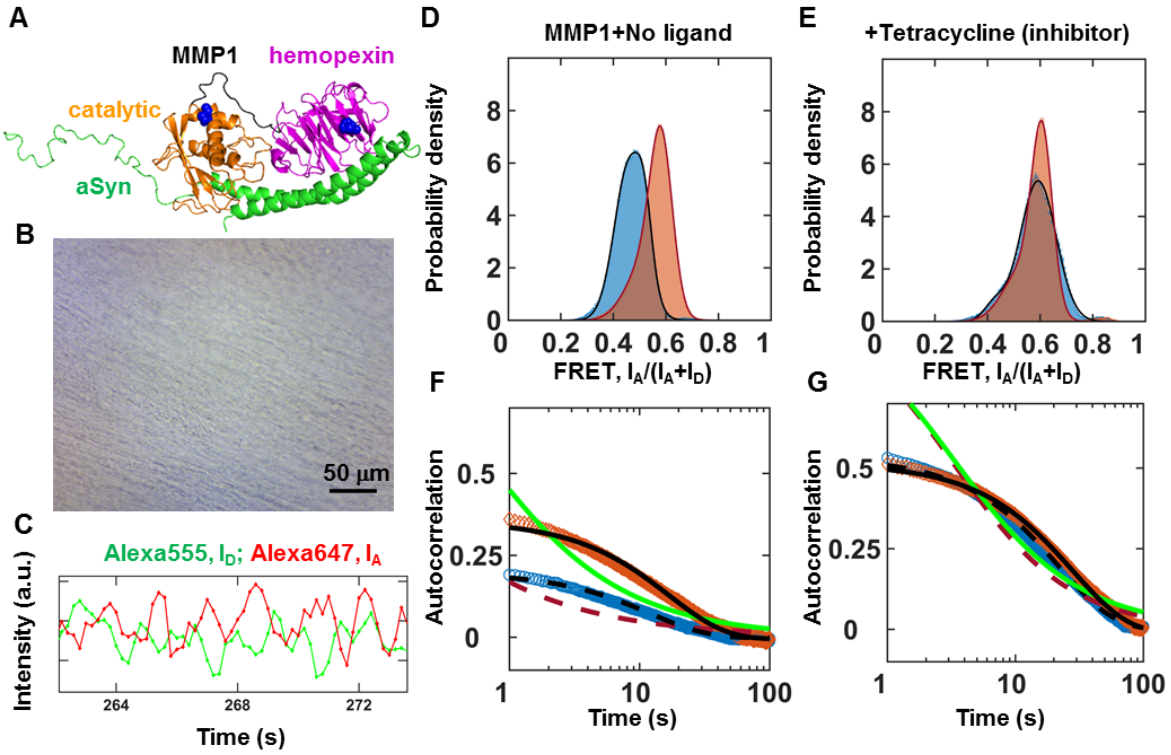

Figure 3.1. Activity-dependent interdomain dynamics of MMP1 on aSyn-induced aggregates at 22 ºC with 100 ms time resolution. (**a**) Relative positions of the MMP1 domains and residues created using PDB ID 4AUO. (**b**) Light microscopy image of aSyn-induced aggregates on a slide. For MMP1-treated aggregates, see Figure 3.2. (**c**) Emission intensities of the two dyes attached to active MMP1. (**d**) and (**e**) Area-normalized histograms of MMP1 interdomain distance (bin size=0.005) without ligand and in the presence of tetracycline (an inhibitor), respectively, for active (blue) and inactive (orange) MMP1. All histograms are fitted to a sum of two Gaussians (active: solid blue line; inactive: solid red line). (**f**) and (**g**) Autocorrelations of MMP1 interdomain distance without ligand and in the presence of tetracycline, respectively, for active (blue) and inactive (orange) MMP1. All autocorrelations are fitted to exponentials and power laws (exponential fit to active: dashed black line; power-law fit to active: dashed red line; exponential fit to inactive: solid black line; power-law fit to inactive: solid green line). The error bars in histograms and autocorrelations represent the square roots of the bin counts and the standard errors of the mean (SEM) and are too small to be seen. For best-fit parameters for histograms and autocorrelations, see Table 3.1 through Table 3.3.

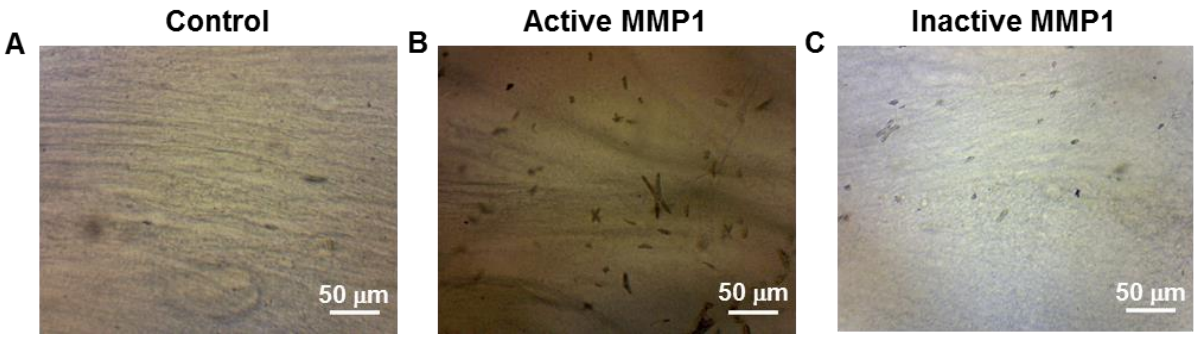

Figure 3.2. Light microscope images of aSyn-induced aggregates stained with Congo red. (**a**) Aggregates on a slide treated with protein buffer. (**b**) Aggregates on a slide treated with active MMP1 at 22 °C for 30 min. (**c**) Aggregates on a slide treated with inactive MMP1 at 22 °C for 30 min.

We report measurements of activity-dependent MMP1 interdomain dynamics on aSyn-induced aggregates of *E. coli* proteins at the single-molecule level. MMP1 prefers open conformations on aSyn-induced aggregates, and these conformations are inhibited by tetracycline. A two-state Poisson process describes the interdomain dynamics of MMP1 on aggregates. Since aSyn-bound MMP1 crystal structures are not available, we used ClusPro for molecular docking of MMP1 with aSyn. We performed all-atom simulations of different binding poses to calculate the interdomain dynamics and compare them with experimental dynamics. It appears that the pose with MMP1 bound to the middle U-shaped region of aSyn structure leads to dynamics similar to experimental dynamics. We used this experimentally guided binding pose to quantify allosteric communications. We also determined the potential ligand binding sites and performed virtual screening against one of these binding sites to compare the lead molecules for free and aSyn-bound MMP1, which showed substrate dependence of virtual screening. Our results pave the way for substrate-dependent virtual screening

guided by molecular insights that may enable inhibition of aggregation and degradation of aggregates.

3.2 Activity-dependent MMP1 dynamics on aSyn aggregates

We purified catalytically active (E219) and inactive (Q219) MMP1 using a protease-based method described in our previous publication. Both active and inactive MMP1 had SER142CYS mutation in the catalytic domain and SER366CYS mutation in the hemopexin domain for labeling with the Alexa555 (donor)-Alexa647 (acceptor) FRET pair. Labeling does not affect the activity of MMP1. To distinguish the effects of enzymatic activity despite potential problems due to the labeling of dyes' photophysical properties, we used inactive MMP1 as control. Since aSyn-induced aggregates are water-insoluble, we created a thin layer of aggregates on a quartz slide. We flowed water-soluble MMPs to image the dynamics of MMP1 using a TIRF microscope. We used a laser at 532 nm to excite Alexa555 (see methods). MMP1 undergoes interdomain dynamics and the distance between Alexa555 and Alexa647 changes. As a result, the non-radiative energy transfer due to FRET between the two dyes changes. Low FRET conformations lead to high Alexa555 emission, whereas high FRET conformations lead to low Alexa555 emission. Anticorrelated Alexa647 and Alexa555 emissions, I_A and I_D, respectively, indicate the conformational dynamics of MMP1. We calculated FRET using the equation $I_A/(I_A+I_D)$, where each FRET value determines the separation between the two MMP1 domains. We plotted the distribution of FRET values to determine the MMP1 conformations. We calculated the correlation between conformations to determine how a conformation at one time is related to another conformation at a later time. A sum of two Gaussians fits the histograms, whereas an

exponential fits the correlations. We fitted both power-law and exponential to the autocorrelations because these are the most common decay types of correlations. The best-fit parameters are in Table 3.1. The fit parameters b1 and b2 are the two states, S1 and S2, respectively. We fitted exponential and power-law distributions to the experimental autocorrelations in Figure 3.1**.** Power law distribution does not fit the experimental autocorrelations. The best-fit parameters for the exponential fits are in Table 3.2. The kinetic rates of interconversion between S1 and S2 are in Table 3.3. The error bars represent the standard errors of the mean.

Table 3.1. Gaussian best-fit parameters for experimental histograms.

	MMP1 without ligands		MMP1 with tetracycline	
	Active	Inactive	Active	Inactive
a1	6.03±0.05	1.94±0.15	0.64±0.04	1.95±0.07
b1/S1	0.46±0.01	0.51±0.01	0.43±0.01	0.53±0.01
c1	0.08±0.01	0.10± 0.01	0.06±0.01	0.10±0.01
a2	1.87±0.09	6.24±0.22	5.36±0.03	6.52±0.14
b2/S2	0.52±0.01	0.58±0.01	0.59±0.01	0.61±0.01
c2	0.04±0.01	0.06±0.01	0.10±0.01	0.06±0.01

Table 3.2. Exponential best-fit parameters for experimental correlations.

	MMP1 without ligands		MMP1 with tetracycline	
	Active	Inactive	Active	Inactive
d	0.20±0.01	0.36±0.01	0.53±0.01	0.53±0.01
e	0.08±0.01	0.06±0.01	0.05±0.01	0.04±0.01
f	-0.01±0.01	-0.01±0.01	-0.01±0.01	-0.01±0.01

Table 3.3. Kinetic rates calculated from histograms and correlations.

	MMP1 without ligands		MMP1 with tetracycline	
	Active	Inactive	Active	Inactive
k1 (s^{-1})	0.0107	0.0396	0.0428	0.0231
k2 (s^{-1})	0.0708	0.0196	0.0030	0.0126

3.3 A two-state Poisson process describes MMP1 dynamics

Recently, we published a quantitative analysis of MMP1 dynamics on collagen fibrils [163] and fibrin [164]. The histograms reveal conformations of MMP1, and the autocorrelations show the relation between conformations at different time points. A sum of two Gaussians fits the histograms of smFRET values, and an exponential fits the autocorrelations. As such, a two-state Poisson process describes the conformational dynamics of MMP1 and enables a straightforward interpretation of the decay rates of correlations [163]. We can establish a quantitative connection between the two states obtained from the Gaussian fits and the exponential fits' decay rates. We defined the two Gaussian centers as the two states, S1 (low FRET) and S2 (high FRET). Also, we defined the two kinetic rates as k1 (S1→S2) and k2 (S2→S1) for interconversion between S1 and S2. For a two-state system, the ratio of rates (k1/k2) is the ratio of Gaussian area(S2)/area(S1), and the sum of rates (k1+k2) is the decay rate of autocorrelation. We calculated k1 and k2 from k1/k2 and k1+k2 for both active and inactive MMP1. Using experimentally determined S1, S2, k1, k2, and noise (widths of the histograms), we simulated smFRET trajectories and analyzed the simulated data similar to the experimental data. Comparing experimentally determined inputs (Table 3.1 – Table 3.3) and recovered parameters from two-state simulations (Table 3.5 –

Table 3.7) shows that a two-state Poisson process describes MMP1 interdomain dynamics.

Table 3.4 Input parameters for simulated histogram and autocorrelations in Figure 3.2.

	Active MMP1 (No ligand)	**Inactive MMP1 (No ligand)**
S1	0.46	0.51
S2	0.52	0.58
k1	0.01 s^{-1}	0.04 s^{-1}
k2	0.07 s^{-1}	0.02 s^{-1}
k1 + k2	0.08 s^{-1}	0.06 s^{-1}
σ1	0.08	0.10
σ2	0.04	0.06

The two states are S1=0.46 and S2=0.52 on aSyn-induced aggregates for active MMP1 without ligand (Table 3.1). In comparison, the two states are S1=0.44 and S2=0.55 on collagen [164] and S1=0.42 and S2=0.51 on fibrin [164] for active MMP1 without ligand. The correlation decay rate of 0.08 s^{-1} on aSyn-induced aggregates for active MMP1 without ligand (Table 3.1). In comparison, the decay rates are 0.13 s^{-1} on collagen [163] and 0.08 s^{-1} on fibrin [164] for active MMP1 without ligand. In the presence of tetracycline, the two-state description still applies even though the two states and interconversion rates between them change compared to the dynamics without ligand (Table 3.4). We performed two-state simulations with and without noise to study how noise affects the histograms and autocorrelations. Both power law and exponential fit the autocorrelations of simulated smFRET trajectories without noise (Figure 3.3f). However, only an exponential fits the autocorrelations with noise. In other words, the presence of noise can convert a power-law correlation into an exponential correlation. This effect is similar to the conversion of a Lorentzian line shape into a

Gaussian line shape [165]. Note that an exponential fit recovers the simulated kinetic rates' underlying sum with and without noise (Table 3.5 – Table 3.7).

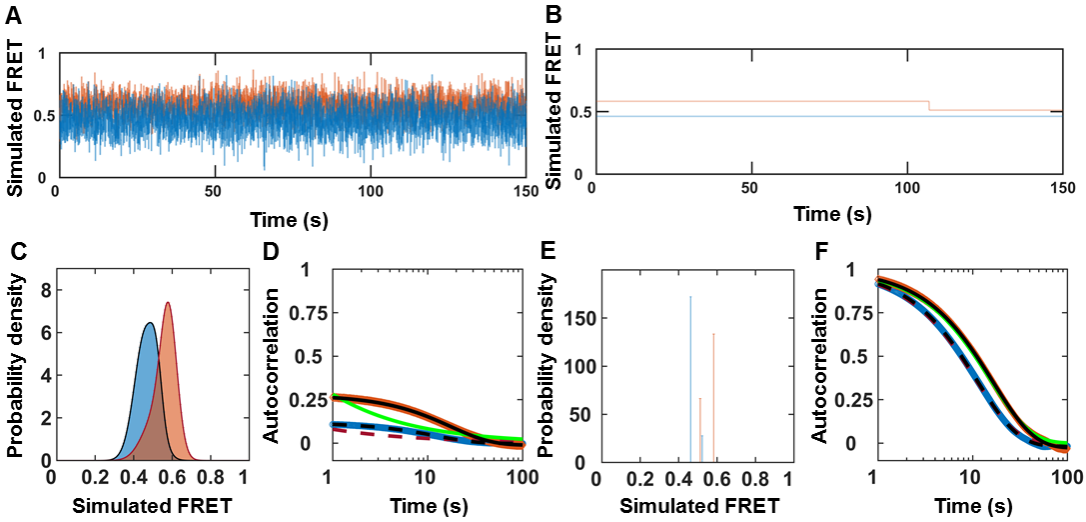

Figure 3.3. Stochastic simulation of MMP1 interdomain dynamics as a two-state system. (**a**) and (**b**) Examples of simulated smFRET trajectories with and without noise, respectively, for active MMP1 (blue) and inactive MMP1 (orange) using experimentally determined parameters for MMP1 without ligands. (**c**) Area-normalized histograms of simulated smFRET values with noise (active: blue; inactive: orange) with best fits to a sum of two Gaussians (solid black line). (**d**) Autocorrelations of simulated smFRET trajectories with noise (active: blue; inactive: orange) with best fits to exponentials (active: dashed black line; inactive: solid black line). Power law does not fit autocorrelations (active: dashed red line; inactive: solid green line). (**e**) Area-normalized histograms of simulated smFRET values without noise (active: blue; inactive: orange) with best fits to a sum of two Gaussians (solid black line). (**f**) Autocorrelations of simulated smFRET trajectories without noise (active: blue; inactive: orange) with best fits to exponentials (active: dashed black line; inactive: solid black line). Both exponential and power-law fit autocorrelations (active: dashed red line; inactive: solid green line). The error bars are the SEMs for histograms and autocorrelations and are too small to be seen.

Table 3.5 Recovered Gaussian fit parameters from simulated histograms.

	Without noise		With noise	
	Active	Inactive	Active	Inactive
a1			6.06±0.01	1.95±0.01
b1/S1	0.46	0.51	0.46±0.01	0.51±0.01
c1			0.08±0.01	0.10±0.01
a2			1.97±0.01	6.25±0.02
b2/S2	0.52	0.58	0.52±0.01	0.58±0.01
c2			0.04±0.01	0.06±0.01

Table 3.6. Power law recovered parameters.

	Without noise		With noise	
	Active	Inactive	Active	Inactive
a	0.01±0.01	0.01±0.01	NA	NA
b	1.8±8.8	1.8±8.6	NA	NA

Table 3.7. Exponential fit recovered parameters.

	Without noise		With noise	
	Active	Inactive	Active	Inactive
d	1.02±0.01	1.03±0.01	0.12±0.01	0.29±0.01
e	0.09±0.01	0.06±0.01	0.08±0.01	0.06±0.01
f	-0.02±0.01	-0.03±0.01	-0.01±0.01	-0.01±0.01

3.4 MMP1 dynamics depend on the aSyn-MMP1 binding pose

Since crystal structures of aSyn-bound MMP1 do not exist, we determined the binding poses of aSyn (PDB ID 1XQ8) and MMP (PDB ID 4AUO) computationally using molecular docking software ClusPro [164, 165]. Figures 3.4a-c show three such binding poses. We selected these poses based on known cleavage sites of aSyn targeted by MMP1 because the computational binding energy may not be the best indicator of appropriate docking poses [166]. We performed all-atom MD simulations for the three binding poses (Figure 3.4) and calculated the catalytic pocket opening (Figures 3.4d-f) and interdomain separation (Figures 3g-i) of MMP1. Since MMP1 stabilized within ~5 ns (Figure 3.6), we performed simulations for 20 ns.

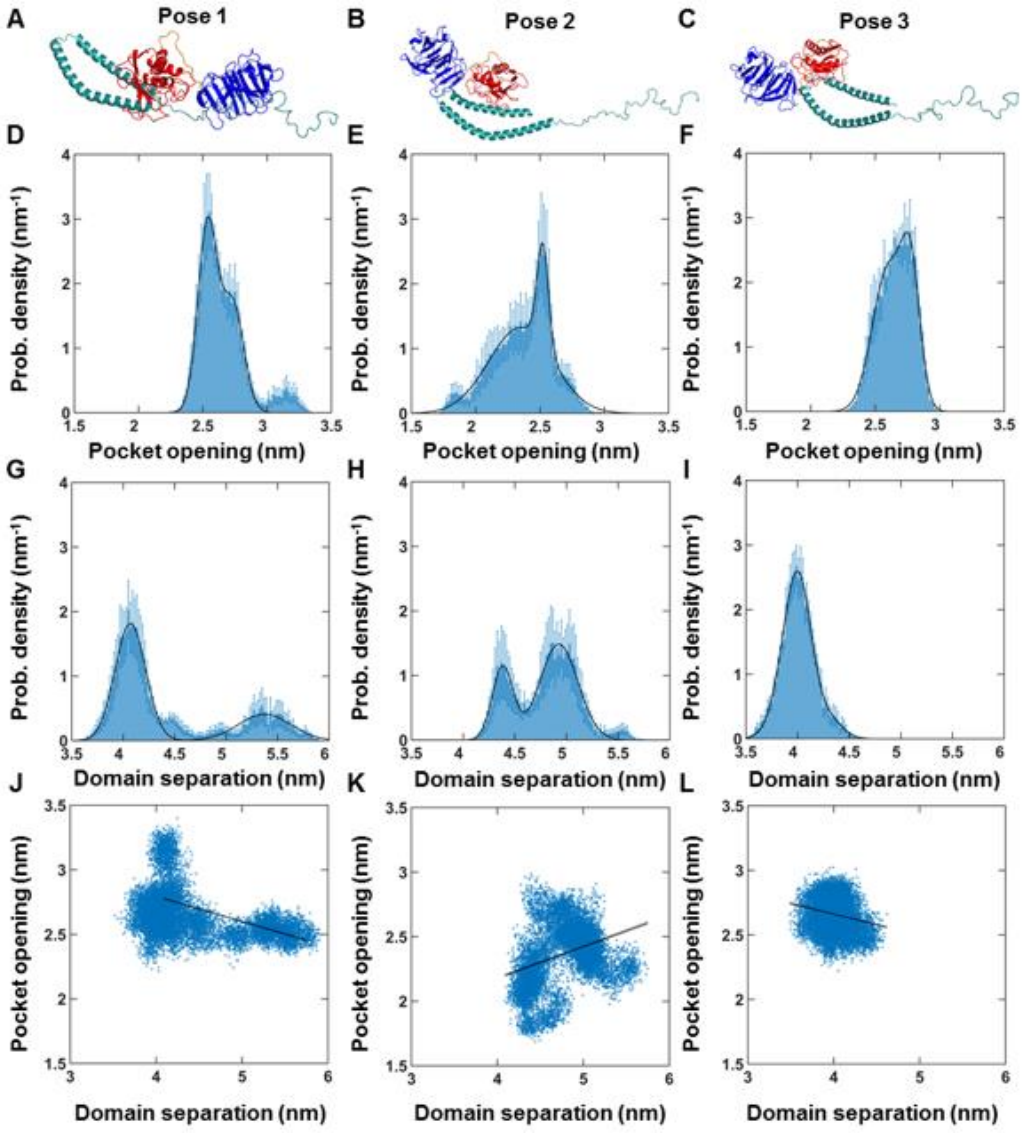

Figure 3.4. MMP1-aSyn binding pose-dependent dynamics of active MMP1 at 37 °C. (**a**), (**b**), and (**c**) Three binding poses of MMP1 at different locations of aSyn. (**d**), (**e**), and (**f**) Area-normalized histograms of the catalytic pocket opening of MMP1 for poses 1, 2, and 3, respectively. (**g**), (**h**), and (**i**) Area-normalized histograms of interdomain separation of MMP1 for poses 1, 2, and 3, respectively. (**j**), (**k**), and (**l**) Linear correlation plots of catalytic pocket opening and interdomain distance for poses 1, 2, and 3, respectively. The data were fitted to $y_i = b_0 + b_1 \times x_i$. Note that a larger domain separation corresponds to a lower FRET value. Time resolution=2 fs, Data saved every 5 ps, RMSD stabilization time for MMP1=~5 ns, Total simulation duration=20 ns. For best-fit parameters, see Table 3.8 – Table 3.9.

Table 3.8. Gaussian best-fit parameters for simulated histograms.

Catalytic pocket opening			
	Pose 1	**Pose 2**	**Pose 3**
a1	1.03±0.19	1.44±0.03	3.29±2.18
b1/S1 (nm)	3.15±0.02	2.71±0.01	2.76±0.01
c1	0.12±0.03	0.09±0.01	0.11±0.01
a2	2.30±0.06	5.97±0.04	1.53±1.53
b2/S2(nm)	2.72±0.01	2.53±0.01	2.67±0.11
c2	0.18±0.02	0.07±0.01	0.14±0.04

Table 3.9. Linear correlation best-fit parameters.

Linear correlation			
	Pose 1	**Pose 2**	**Pose 3**
b0	2.72±0.13	3.28±0.06	2.72±0.05
b1	0.02±0.03	-0.15±0.01	0.01±0.01

Previously, we reported a positive correlation between the catalytic pocket opening and interdomain separation for MMP1 dynamics on collagen [167] and fibrin [168]. Based on the criterion of positive correlation, it appears that binding pose 3 is likely to be one of the most appropriate binding poses. Previous reports of MMP1 cleavage sites on aSyn are consistent with our suggestion that pose 3 is a suitable binding pose.

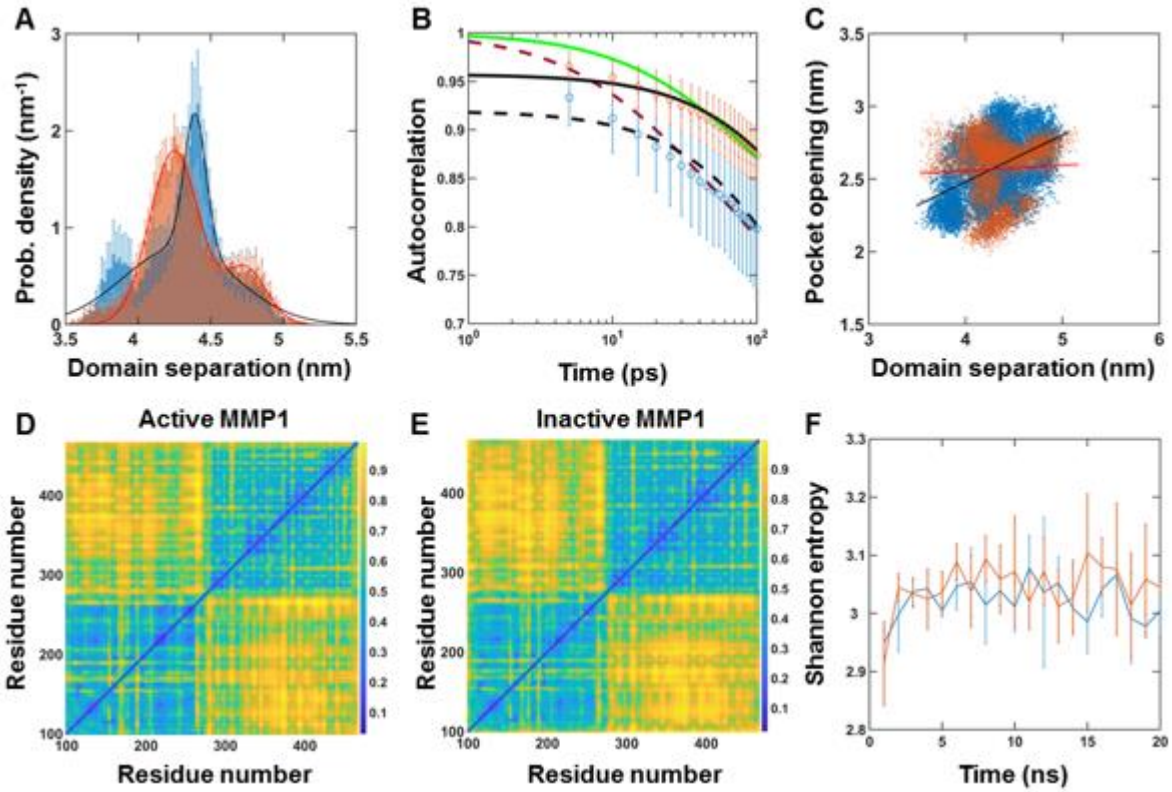

Figure 3.5. All-atom MD simulation of MMP1 interdomain dynamics at 22 °C. (**a**) Area-normalized histograms of simulated interdomain distance (active: blue; inactive: orange) with best fits to a sum of two Gaussians (solid black line). (**b**) Autocorrelations of simulated interdomain distance (active: blue; inactive: orange) with best fits to exponentials (active: dashed black line; inactive: solid black line). Power law does not fit autocorrelations (active: dashed red line; inactive: solid green line). (**c**) Linear correlation plots of catalytic pocket opening and interdomain distance. (**d**) and (**e**) Correlations between residues for active and inactive MMP1, respectively. (**f**) Shannon entropy calculated from correlation plots for active (S=3.01±0.01, mean±SEM) and inactive (S=3.06±0.01, mean±SEM).

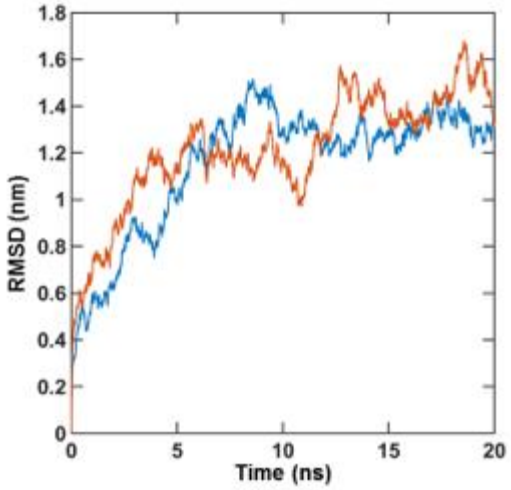

Figure 3.6. Stabilization of dynamics. RMSD for active (blue) and inactive (orange) MMP1 without ligands at 22 °C. We defined the input structure at t=0 as the reference structure and calculated the root-mean-square-displacement (RMSD) to check the simulations' stabilization. Simulations of MMP1 dynamics stabilize in ~5 ns. As such, we simulated 20 ns long dynamics for different conditions.

3.5 Shannon entropy enables quantification of allosteric communications

Proteins are inherently flexible biomolecules having both intra- and interdomain motions. Two types of randomness appear as proteins interact with their surroundings and substrates. At a particular time point, the amino acids' locations and angles have a spatially random component. As time progresses, proteins sample through different conformations leading to temporal randomness. Such correlated or collective fluctuations are essential for functions, including allosteric regulation, generation of mechanical work, catalysis, ligand binding, and protein folding [164, 169-174]. Correlated allosteric motions decrease the conformational entropy and affect the kinetics and thermodynamics of biological processes [175]. Shannon entropy is a quantitative measure to describe randomness in computer science and pattern

recognition and has been successfully applied to quantify allostery in proteins to gain insights into their functional relevance [176-179].

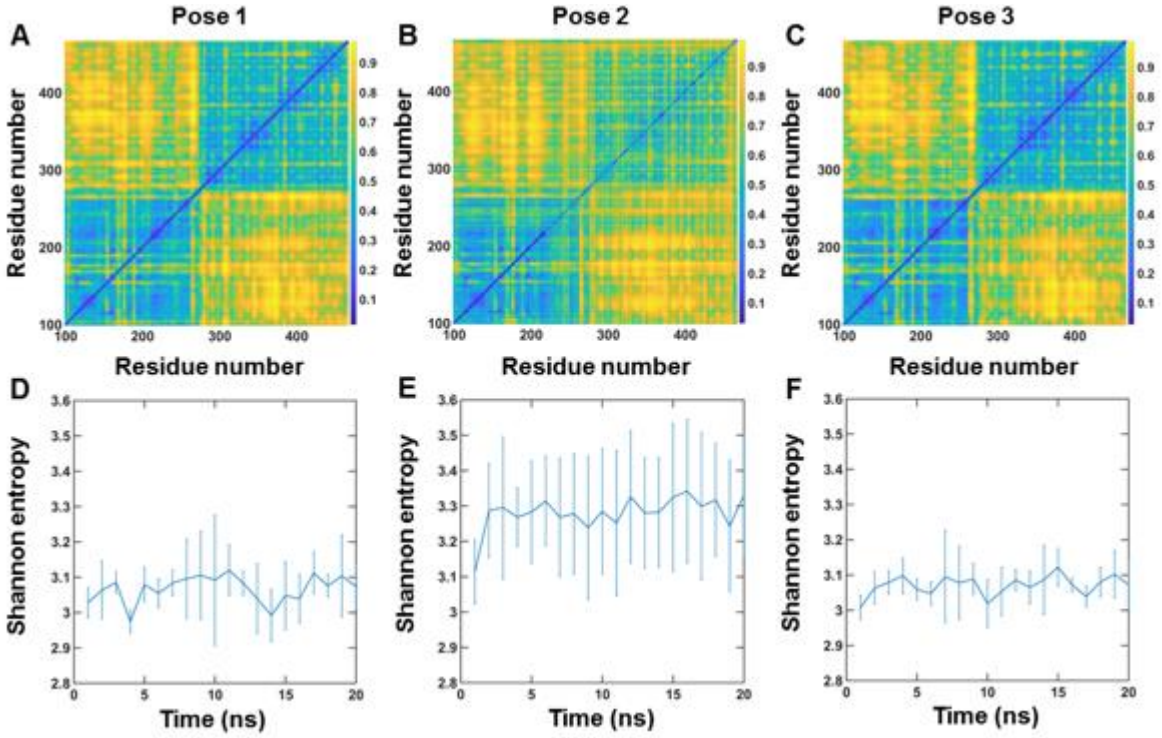

Figure 3.7. Pose-dependent correlation between residues of active MMP1 and quantification of allostery using Shannon entropy. (**a**), (**b**), and (**c**) Correlations between residues for poses 1, 2, and 3, respectively, at 37 °C. (**d**), (**e**), and (**f**) Shannon entropy calculated from correlation plots for poses 1 (S=3.07±0.02, mean±SEM), 2 (S=3.10±0.01, mean±SEM), and 3 (S=3.05±0.01, mean±SEM), respectively. For details, see Calculation of Entropy in section 3.9.7.

Since a correlated motion suggests a decrease in randomness or lower entropy, we calculated correlations between each pair of residues in MMP1 and estimated entropy (Figure 3.7). We divided all-atom simulations into 1 ns long windows. In each 1 ns window, there were 200 radial coordinates for residues. We calculated the correlations between every pair of residues and normalized them to a range of 0 to 1 by subtracting the minimum and then dividing by the maximum. Figures 3.7a-c show the matrix of correlation values at lag number 1, averaged over 20 ns. We divided the

correlation values to create 10 bins of width 0.1, calculated 10×10 gray-level co-occurrence matrix (GLCM), and defined Shannon entropy $S = -\sum p_i \ln p_i$, where p_i is the probability of a microstate i. The catalytic domain residues (F100-Y260) have strong correlations with the hemopexin domain residues (D279-C466), suggesting allosteric communications in MMP1 (Figures 3.7a-c). The time-evolutions of Shannon entropy are shown in Figures 3.7d-f. Pose 3 has the lowest entropy consistent with the functionally relevant binding pose.

3.6 Experimentally-measured dynamics agree with MD simulation dynamics

We performed all-atom MD simulations of the binding pose 3 at 22 °C for active and inactive MMP1. Figure 3.5a shows the distributions of the interdomain distance between S142 and S366. In agreement with experiments (Figure 3.1d), active MMP1 adopts conformations with the two domains separated more than inactive MMP1. Also, simulated dynamics correlations (Figure 3.5b) follow the experimental pattern (Figure 3.1f), with inactive MMP1 having higher values with longer correlation times. We used experimentally consistent simulations to gain further insights. First, the correlation between the catalytic pocket opening and interdomain separation for active MMP1 is higher than inactive MMP1 (Figure 3.5c). A larger catalytic pocket opening enables substrates to get closer to the active site. Second, the two-dimensional correlation plots show allosteric communications between the two domains (Figures 3.5c-d). Third, Shannon entropy describing the randomness of two-dimensional correlations plots shows a lower value for active MMP1 than inactive MMP1 (Figure 3.5f).

3.7 Catalytic site changes and identification of allosteric residues on MMP1

We performed MD simulations for free MMP1 (Figure 3.8a) and compared them with the simulations (Figure 3.7c) for pose 3 (Figure 3.4c) of aSyn-bound MMP1. The comparison revealed how the conformations of MMP1 catalytic motif HELGHSLGLSH changed. We considered the catalytic residue E219 as the origin and then plotted the pairwise distance with the catalytic motif residues in three dimensions. The symbol size of the locations is proportional to the standard deviation of the pairwise distance (Figure 3.8b). The configuration at the MMP1 catalytic site changes considerably as free MMP1 binds aSyn.

We plotted histograms of correlation values for free and aSyn-bound MMP1 and determined the threshold correlation values at 0.8 (peak probability density (~2.3) divided by e) (Figure 3.8c). We found all the residues with normalized correlations greater than 0.8 in Figure 3.7c and Figure 3.8a with the catalytic motif residues HELGHSLGLSH and compared the residues between free MMP1 and aSyn-bound MMP1. We identified that 377 and 466 have exclusive correlations with the catalytic motif residues only MMP1 binds aSyn. This is significant because it may be possible to identify exclusive residues for other substrates of MMP1 and control one MMP1 function without affecting the other functions.

3.8 Lead molecules from virtual screening differ upon substrate binding

Guided by experiments and simulations, we determined that pose 3 is likely a relevant binding pose between MMP1 and aSyn. We used the experimentally-informed binding pose for the virtual screening of molecules. Virtual screening enables testing

considerably more ligands economically and faster than high-throughput experimental screening. A wide range of strategies can be divided into ligand-based and structure-based virtual screening [180].

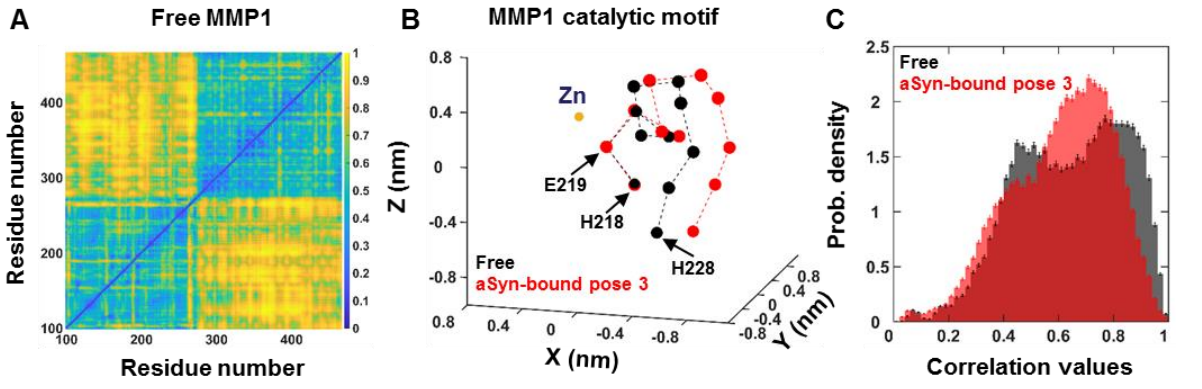

Figure 3.8. Conformational changes near the catalytic motif and identification of allosteric residues on MMP1. (**a**) Normalized correlations between each pair of residue for free active MMP1 at 37 °C. (**b**) Three-dimensional configurations of the catalytic motif residues for free active MMP1 (black) and aSyn-bound MMP1 (red) at 37 °C. (**c**) Histograms of correlation values of free MMP1 (black) and aSyn-bound MMP1 (red).

In ligand-based virtual screening, known ligands against a target serve as benchmarks to screen for more ligands with similar properties. In contrast, structure-based screening uses the binding sites on a target to screen molecules leveraging the conformational changes and energetic complementarity upon ligand binding. Since MMP1 has broad-spectrum protease activity, we determined the binding sites on free MMP1 and aSyn-bound MMP1 to investigate a substrate's effects. We predicted the potential ligand-binding sites using AutoLigand and MGLTools 1.5.7 and selected a potential binding site in the hemopexin domain of MMP1 to screen for allosteric ligands (Figure 3.9).

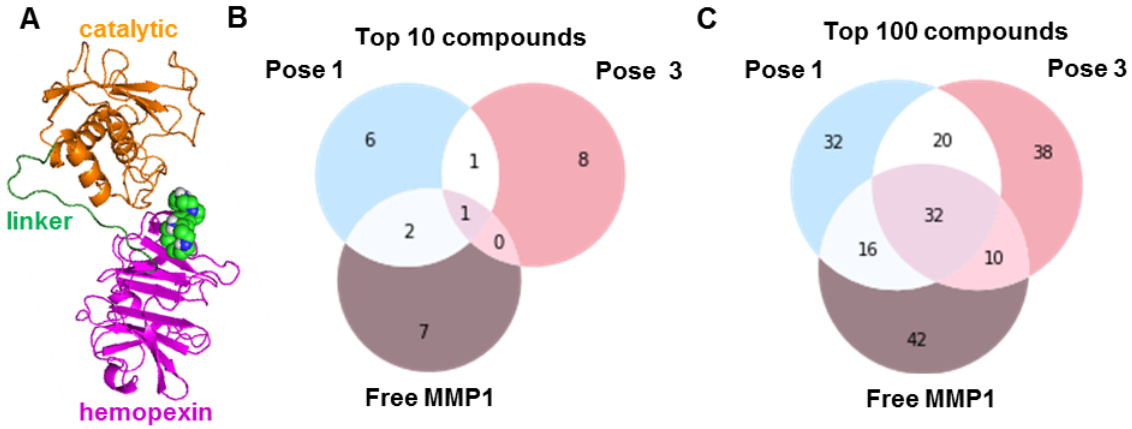

D

Free MMP1		aSyn-MMP1 Pose 1		aSyn-MMP1 Pose 3	
Drug	Affinity (kcal/mol)	Drug	Affinity (kcal/mol)	Drug	Affinity (kcal/mol)
Plerixafor	-9.76	Plerixafor	-9.84	Altabax	-9.35
Vorapaxar	-9.09	Irinotecan	-9.66	Topotecan	-9.16
Adapalene	-9.01	Lurasidone	-9.27	Naldemedine	-9.15
Ursodeoxycholic acid	-8.99	Imatinib	-8.99	Plerixafor	-9.12
Bosutinib	-8.95	Alectinib	-8.92	Abiraterone	-9.03
Dihydroergotamine	-8.92	CID 454469	-8.85	Sildenafil	-8.98
Pancuronium	-8.77	Obeticholic Acid	-8.71	Alectinib	-8.94
Lifitegrast	-8.75	L-Thyroxine	-8.64	Retapamulin	-8.93
Ciclesonide	-8.65	Ciclesonide	-8.53	Ponatinib	-8.92
Irinotecan	-8.64	Vecuronium	-8.52	Ergotamine	-8.87

Figure 3.9. Substrate- and pose-dependent virtual screening against MMP1. (**a**) MMP1 bound to Plerixafor (green and blue spheres), the top hit against free MMP1. We performed virtual screening against the same site for free MMP1, pose 1, and pose 3. (**b**) and (**c**) Venn diagrams of top 10 and 100 molecules show unique and common ligands. (**d**) Identities and affinities for the top 10 molecules. For docking parameters, see Figure 3.10.

We performed screening against the selected site in the hemopexin domain for free MMP1 and two poses of aSyn-bound MMP1. We performed molecular docking using AutoDock and set up the virtual screening with Raccoon 1.1. We used default AutoDock docking parameters (see supplementary information) to determine the binding affinities for a collection of 1,400 FDA-approved compounds from the ZINC15 database.

```
autodock_parameter_version 4.2          # used by autodock to validate parameter set
outlev 1                                # diagnostic output level
intelec                                 # calculate internal electrostatics
seed pid time                           # seeds for random generator
ligand_types A C HD N OA SA             # atoms types in ligand
fld MMP1aSyn01.maps.fld                 # grid_data_file
map MMP1aSyn01.A.map                    # atom-specific affinity map
map MMP1aSyn01.C.map                    # atom-specific affinity map
map MMP1aSyn01.HD.map                   # atom-specific affinity map
map MMP1aSyn01.N.map                    # atom-specific affinity map
map MMP1aSyn01.OA.map                   # atom-specific affinity map
map MMP1aSyn01.SA.map                   # atom-specific affinity map
elecmap MMP1aSyn01.e.map                # electrostatics map
desolvmap MMP1aSyn01.d.map              # desolvation map
move ZINC000001536779.pdbqt             # small molecule – **change for each ligands**
about -3.608 -2.104 1.030               # small molecule center
tran0 random                            # initial coordinates/A or random
quaternion0 random                      # initial orientation
dihe0 random                            # initial dihedrals (relative) or random
torsdof 6                               # torsional degrees of freedom
rmstol 2.0                              # cluster_tolerance/A
extnrg 1000.0                           # external grid energy
e0max 0.0 10000                         # max initial energy; max number of retries
ga_pop_size 150                         # number of individuals in population
ga_num_evals 2500000                    # maximum number of energy evaluations
ga_num_generations 27000                # maximum number of generations
ga_elitism 1                            # top individuals to survive to next generation
ga_mutation_rate 0.02                   # rate of gene mutation
ga_crossover_rate 0.8                   # rate of crossover
ga_window_size 10                       #
ga_cauchy_alpha 0.0                     # Alpha parameter of Cauchy distribution
ga_cauchy_beta 1.0                      # Beta parameter Cauchy distribution
set_ga                                  # set the above parameters for GA or LGA
sw_max_its 300                          # iterations of Solis & Wets local search
sw_max_succ 4                           # consecutive successes before changing rho
sw_max_fail 4                           # consecutive failures before changing rho
sw_rho 1.0                              # size of local search space to sample
sw_lb_rho 0.01                          # lower bound on rho
ls_search_freq 0.06                     # probability of performing local search on individual
set_psw1                                # set the above pseudo-Solis & Wets parameters
unbound_model bound                     # state of unbound ligand
ga_run 10                               # do this many hybrid GA-LS runs
analysis                                # perform a ranked cluster analysis
```

Figure 3.10. Small molecule virtual screening. An example of Autodock parameters shared amongst ligands

We used FDA-approved molecules because those provide a smaller set of commercially available molecules. We fixed the otherwise flexible side chains. Flexible side chains would have given slightly more accurate screening but would require more computational time. We found that the lead molecules against MMP1 change depending on the substrate and pose. Figures 3.8b-d show the top molecules for free MMP1 and the two aSyn-MMP1 binding poses, suggesting that substrate binding and different poses can lead to different results. Venn diagrams of molecules (Figure 3.8a) show that there are molecules unique to each case. The ligand-binding site was common to free MMP1, pose 1, and pose 3. However, conformational differences in the three cases impact the virtual screening. The unique molecules for each case suggest that we should perform substrate-specific screening to identify unique ligands, thus resolving problems arising from MMP promiscuity.

3.9 Summary

In summary, we measured the interdomain dynamics of MMP1 on aSyn-induced protein aggregates and modeled the dynamics as a two-state Poisson process. Distributions of conformations and correlation decay rates of MMP1 on aSyn-induced aggregates follow the general pattern that we previously reported for collagen and fibrin, i.e., open MMP1 conformations are functionally relevant, and there are time-dependent correlations of conformations [181, 182].

Since there is no crystal structure for aSyn-bound MMP1, we determined the binding poses using molecular docking. We performed all-atom simulations of dynamics for different binding poses between aSyn and MMP1 and compared them with single-molecule measurements of dynamics. A comparison of experiments and simulations

suggests that the pose in which MMP1 binds to aSyn near TYR39 (pose 3) leads to a better match with experiments. However, there are two important caveats. First, we performed simulations on aSyn monomer, but the experiments were done on aggregates. We took a similar approach for collagen and found that simulations on collagen monomer agreed with experiments on collagen fibril when the collagen backbone was restrained, suggesting strains in collagen monomers inside collagen fibrils. For aSyn, we did not have to restrain the aSyn backbone for agreement between simulations and experiments, suggesting a lack of strain in aSyn-induced aggregates [163]. Second, aSyn is considered an intrinsically disordered protein that assumes structure upon binding substrate [51, 164]. Also, aSyn purified from neuronal and non-neuronal cell lines generally suggests a "natively folded" ~58 kDa tetrameric form [139, 140]. Nevertheless, the combined experiment-simulation approach using the monomer structure of aSyn provides a starting point for molecular-level understanding.

We used experimentally guided simulations to quantify the randomness of dynamics by calculating correlations between each pair of residues in MMP1. We defined another matrix called GLCM to define Shannon entropy from the correlation matrix to quantify the randomness with a single number at each time point. The entropy for active MMP1 is smaller than inactive MMP1, suggesting that MMP1 activity may be entropy-driven because a lower entropy (stabilized conformations) is likely essential for substrates to get closer to the active site for a long enough duration for catalysis.

We performed virtual screening of molecules against aSyn-bound MMP1 and compared it with free MMP1. To this end, we found that the potential ligand-binding sites change upon binding aSyn and depend on the binding pose. As such, we selected

an allosteric binding site on MMP1 and screened 1,400 FDA-approved molecules against the site for free MMP1 and two binding poses with aSyn. The lead molecules and their scores change upon binding the substrate and depend on the binding pose. Therefore, substrate-dependent binding sites and lead molecules suggest that any effort to target MMP1 may need to consider the substrate, the binding pose, and the ligand-binding site. The synergistic combination of experiments and simulations enables modulation of MMP1 activity using molecular insights at the single-molecule level. It may pave the way for substrate-specific control of MMP activity using allosteric ligands.

3.10 Materials and Methods

This section will outline the material and methods for the experiments described in chapter 3. This includes reference to chapter 1 for the formation of the aggregate, the methodology for the biochemical assays and conditions for MD and other *in silico* simulations.

3.10.1 Purification of MMP1 and aSyn

The MMP1 and aSyn sequences were inserted into the pET21b+ and pET11a vectors, respectively, between NdeI (N-terminal) and HindIII (C-terminal) restriction sites. We transformed the plasmids into Rosetta (DE3) pLysS *E. coli* (Millipore, Cat# 70956-4) for protein expression. We purified MMP1 and aSyn, as described in our previous publications [48, 183]. The method of purifying aSyn also produced aSyn-induced aggregates used in experiments.

3.10.2 Measurements of MMP1 interdomain dynamics

For smFRET measurements of MMP1 interdomain dynamics, we mutated two serine residues in MMP1 at locations 142 and 366 to cysteines for labeling with Alexa555 and Alexa647 dyes. In addition, we introduced the E219Q mutation in the catalytic domain to create a catalytically inactive mutant of MMP1. We spread aSyn-induced aggregates and made a thin layer on a quartz slide. We made a flow cell for single-molecule experiments using a piece of double-sided adhesive tape sandwiched between the quartz slide and a glass coverslip. Labeled MMPs were flowed into the flow cell and excited at 532 nm wavelength using the evanescent wave created at the quartz slide and sample buffer interface in a Total Internal Reflection Fluorescence (TIRF) microscope. We acquired two-channel movies to detect emissions from Alexa555 and Alexa647. Any relative motion between the two MMP1 domains would lead to a non-radiative transfer of energy from Alexa555 to Alexa647 due to FRET, increasing the emission from Alexa647 (I_A) and simultaneously reducing the emission from Alexa555 (I_D). We calculated FRET efficiency by $I_A/(I_A+ I_D)$ [184]. Single-molecule experiments and analyses have been described in our previous publications [185-188].

3.10.3 All-atom simulations

We removed all zinc and calcium ions and the water molecules from PDB ID 4AUO and replaced the missing side-chain atoms using Chimera's rotamer tool. PDB files for active and inactive MMP1 were created by replacing A219 with E219 and Q219, respectively, using Pymol's mutagenesis function. We used Gromacs 2019.6 with the Gromos96 43a1 force field to perform the MD simulations. We ignore the hydrogen atoms while creating the topology file. Each simulation ran 20 ns long, simulated at 2 fs/step, and sampled every 5 ps. Each MMP1 crystal was placed in a cubic box with 3D

period boundary conditions and solvated with water (using a single point charge model (SPC)) and Na counter-ions to create a neutral system. We then used the steepest descent algorithm to minimize the solution's energy. To equilibrate the solution with the protein complex, we used NVT and NPT ensemble simulations. First, we performed the NVT simulation and set the mean temperature at the desired temperature of 295 K (22 °C) or 310 K (37 °C) using a Berendsen thermostat for 100 ps. We used the Verlet cut-off scheme for neighbor searching and updated the neighbor list every 20 fs. We used the particle mesh Ewald scheme to calculate the electrostatic interactions with a cubic interpolation order of 4 and a cut-off at 1 nm. We assigned initial velocities using a Maxwell distribution from the corresponding temperature. In the NPT simulation, we maintained velocities from the NVT simulation output, and the pressure was set to 1 bar using a Parrinello-Rahman barostat for an additional 100 ps. Once the NVT and NPT simulations finished and the system equilibrated, we removed the position restraints and ran the production MD for 20 ns. We edited the final coordinates in the trajectory file to correct for periodicity and center the protein complex. The distances between the catalytic pocket residues and the serine residues (interdomain distance) are then measured at every time step using the Gromacs distance function. We measured the interdomain separation between the nitrogen atoms of residues S142 and S366 and the catalytic pocket opening between the nitrogen atoms of residues N171 and T230. To calculate the correlation and Shannon entropy, we recorded the nitrogen atom's coordinates in each residue of MMP1.

3.10.4 Analysis of experimental and simulated interdomain dynamics

We chose the histograms' bin width to be at least the inverse of the sample size's square root, i.e., $1/\sqrt{N}$, N is the number of data points. We calculated the error of count in each bin as the square root of the bin count. Both the bin counts and errors were divided by the area of the histogram to create the area-normalized histogram (probability density function). The area under the normalized histogram equals 1. We fitted a sum of two Gaussians to the histograms:

$$y = a_1 \times e^{-\frac{(x-b_1)^2}{c_1^2}} + a_2 \times e^{-\frac{(x-b_2)^2}{c_2^2}} \tag{3.1}$$

where a's, b's, and c's are amplitudes, centers, and widths of the Gaussians. The parameters b1 and b2 are the two states, S1 and S2.

To calculate correlations, we subtracted the average value from each trajectory and used the following equation to calculate correlations:

$$C_\tau = \frac{1}{N-\tau} \sum_{t=0}^{N-\tau} \left\{ I(t) - \frac{1}{N-\tau} \sum_{t'=0}^{N-\tau} I(t') \right\} \times \left\{ I(t+\tau) - \frac{1}{N-\tau} \sum_{t'=\tau}^{N} I(t') \right\} \tag{3.2}$$

where C_τ is the correlation at lag number τ, N is the number of points in a FRET trajectory, and $I(t)$ is the FRET value at t. For autocorrelations, both factors in curly brackets were from the same time series. For cross-correlations, the two factors in curly brackets were from different time series.

We normalized correlations by dividing correlation values at each lag by $C_{\tau=0}$. We fitted correlations between $\tau = 1$ and $\tau = 1000$ to both power-law and exponential

distributions. For power law, we used a form of Pareto distribution [189] that satisfies the boundary conditions, i.e., $C_{\tau=0}=1$ at $t=0$ and $C_{\tau=\infty}=0$ at $t=\infty$.

We fitted the following equations of power-law and exponential functions:

$$C_{\tau}=\left(a\times\tau+1\right)^{-b} \tag{3.3}$$

$$C_{\tau}=d\times\exp^{-e\times\tau}+f \tag{3.4}$$

To quantify correlations between the catalytic pocket opening and interdomain separation from simulations, we used the interdomain distance as the single predictor variable for the catalytic pocket distance in a linear model. A linear model describes a response variable as a function of predictor variables. Linear models are often fit using a method known as statistical regression. There are different regression methods used, depending on the number of predictor variables. When using only one predictor variable, the regression method is known as the simple linear regression, which we used for quantifying correlations. We used the following equation:

$$y_i=b_0+b_1\times x_i \tag{3.5}$$

Where b_0 and b_1 are the estimated fit parameters. There are also a few different methods to estimate the parameters of the linear model. The most-used approach is the least-squares operator, which finds the slope through the data that minimizes the squared distance between the fit and the residues. There is still uncertainty in these estimations, no matter which method we used. Confidence bands visually represent the uncertainty in linear models by showing the range of possible slopes. We calculated the 95% confidence interval of each predictor value's mean.

3.10.5 Small molecule putative binding sites on MMP1

For virtual screening, we selected free MMP1 and two poses of aSyn-MMP1 binding. First, we predicted potential putative binding sites using AutoLigand and MGLTools 1.5.7. We assigned hydrogen atoms (including polar hydrogens) and Gasteiger partial charges to each of the two aSyn-bound MMP1 poses and free MMP1. Zinc and calcium ions were removed. A grid map with 1Å spacing was then applied to the hemopexin and catalytic domains in addition to the linker region, making the docking unbiased for different binding sites, especially allosteric ones. AutoLigand was then used to define four binding site calculations per structure, beginning with 100 points to define the volume of the binding envelope, then increasing the number of points to 200, 300, and finally 400. The binding envelopes defined were analyzed using AutoDock, and results visualized using MGLTools and VMD.

3.10.6 Virtual screening of small molecules against a putative site on MMP1

We performed molecular docking using AutoDock, and the virtual screening was set up with Raccoon 1.1. The receptor was considered rigid, and rotatable bonds imparted flexibility to the ligands. We used default AutoDock docking parameters (see supplementary information) to determine the small-molecule binding affinities. A collection of 1,400 FDA-approved compounds were obtained from the ZINC15 database. We began by importing the ligand multiple structure MOL2 file into Raccoon. Each ligand was automatically converted into a separate PDBQT while settling hydrogen atoms and partial charges. We calculated a set of new grid map files with a grid spacing of 0.37Å to include the selected putative binding site from the binding site prediction. For each of the three cases (free MMP1 and two aSyn-MMP1 poses), 100

ligands with the lowest binding affinities were identified. The lead molecules' ZINC IDs were converted to chemical IDs (CIDs) for comparison. The top 10 ligands were identified by their common names.

3.10.7 Calculation of Entropy

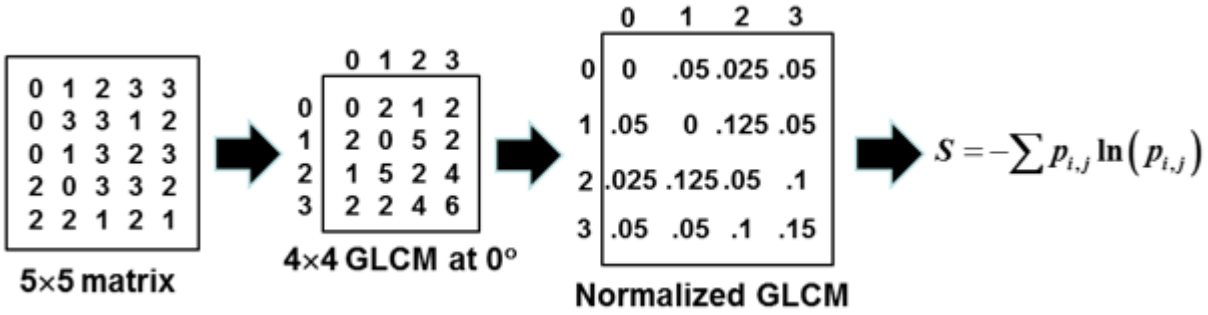

Figure 3.11. Calculation of GLCM and entropy.

We calculated the Gray-Level Co-Occurrence Matrix (GLCM) [190] from the two-dimensional correlation plots. Then, we defined the Shannon entropy [191] from the GLCM. We describe the steps for calculating the Shannon entropy of MMP1 conformational dynamics in Figure 3.10 using an arbitrary 5×5 matrix, where each element of the matrix has a value between 0 and 3. In other words, we have a 2-bit 5×5 matrix in Figure 3.10. The dimension of GLCM depends on the number of possible values (0, 1, 2, 3), i.e., 4×4 for the 5×5 matrix in Figure 3.10.

We calculated the GLCM at 0°, i.e., we only considered the next neighbor on the left and right. For example, we calculated the (0,0) element of GLCM by finding the value 0s in the original 5×5 matrix and counting the number of times 0s appear on the left and right. The number is 0, and as such, the (0,0) element of GLCM is 0. To

calculate the (0,1) element of GLCM, we found the value 0s in the original 5×5 matrix and counting the number of times 1s appear on the left and right. The number is 2, and as such, the (0,1) element of GLCM is 2. We repeated this process for all the elements of GLCM and obtained the matrix in the middle (Figure 3.11). We calculated the sum of all elements and divided each element by the sum to obtain the normalized GLCM at the left (Figure 3.11). We used $S = -\sum p_{i,j} \ln\left(p_{i,j}\right)$, where $p_{i,j}$ is the (i,j) element of GLCM to quantify the Shannon entropy. By definition, we considered $\ln\left(p_{i,j}\right) = 0$ for $p_{i,j} = 0$. Note that one can calculate GLCM at other angles [190]. For MMP1 conformational dynamics, the dimension of correlation matrices is 267×267. We divided the correlation values between 0 and 1 into 10 bins of width 0.1. As such, the dimension of GLCM for MMP1 dynamics is 10×10.

CHAPTER FOUR

INTERACTIONS OF MATRIX METALLOPROTEASES WITH AMYLOID-BETA

4.1 Introduction

Extracellular amyloid plaques, a key hallmark of AD [192], are mostly composed of Aβ [193]. Proteolytic cleavage of amyloid precursor protein (APP) by α-secretase leads to non-amyloidogenic fragments, neuroprotection, and memory enhancement [194]. With age, non-specific fragmentation by β-secretase and γ-secretase becomes prevalent and amyloidogenic fragments, including Aβ(1–40) and Aβ(1–42), appear in the extracellular space [195]. Soluble monomers, polymers, and fibrils of extracellular Aβ aggregate to form the amyloid plaques [196, 197].

MMPs are one class of Aβ-degrading enzymes [25]. Several MMPs in the 23-member human MMP family interact with Aβ and have relevance in AD and neurodegeneration [198-200]. MMPs are broad-spectrum proteases with diverse proteolytic and non-proteolytic intracellular functions [10-12]. MMPs are ubiquitous throughout the human body and are found in extracellular space [36], intracellular space, blood, intestine, and brain [37-40]. The implication of MMPs AD and PD is significant because tetracycline, an inhibitor of MMPs, has shown therapeutic potential in AD and PD [13-15, 155, 156]. In the context of AD, an enhanced MMP1 activity correlates with dysfunction of the blood-brain barrier [201]. MT-MMP1 cleaves Aβ between H14 and Q15 [26]. MMP9 is known to degrade Aβ fibrils *in vitro*, Aβ plaques *in situ*, and Aβ *in vivo* [9, 24, 202-204].

Degradation of Aβ by MMPs may lead to aggregation, but the broad-spectrum activity of MMPs may also be useful in degrading existing Aβ-induced aggregates. However, it is unclear how water-soluble MMPs interact with water-insoluble Aβ-induced aggregates. Since standard biochemical assays are not suitable for studying water-insoluble substrates, we have developed a single-molecule tracking approach and weight-based activity assay. We focused on MMP1, a well-studied MMP of the 23-member human MMP family, to study how MMP1 interacts with Aβ-induced aggregates at the single-molecule level. Since MMP1 interacts with diverse substrates, we need to put the insights into Aβ-MMP1 interactions in the broader context of MMP1 promiscuity for substrate-specific targeting of MMPs in the future. The catalytic domain sequence across the MMP family is very similar, but the hemopexin domain sequence varies, suggesting a role of communications in substrate diversity and specificity [11, 160-162]. Recently, we reported activity-dependent MMP1 dynamics and allosteric communications on type-1 collagen fibrils, fibrin, and aSyn-induced aggregates [163, 164]. We found that functionally relevant conformations on the three substrates are open MMP1 conformations with the catalytic and hemopexin domains well-separated. These open conformations often accompany a larger catalytic pocket opening of MMP1, facilitating the substrates to get closer to the active site of MMP1. However, we need to investigate whether the preference for the open conformations of MMP1 is true for all substrates and allosteric communications are substrate-specific.

In this chapter, we report measurements and analyses of MMP1 interdomain dynamics on water-insoluble Aβ-induced aggregates using smFRET. We mutated S142 and S366 to CYS for labeling with Alexa555 and Alexa647, a FRET pair of dyes. We

calculated the interdomain distance between S142C and S366C from the anticorrelated emission of the two dyes and quantitatively described the dynamics by a two-state Poisson process. A two-state description enables the determination of kinetic rates of interconversion, k_1, and k_2, between the two states because histograms provide the ratio of (k_1/k_2) and correlations of FRET values provide the sum (k_1+k_2). We performed MD simulations of Aβ-bound MMP1 and matched them with experiments. We created a two-dimensional map of fluctuation correlations between every pair of MMP1 residues to show strong allosteric communications in MMP1 and calculated a Gray Level Co-occurrence Matrix to quantify Shannon entropy of the conformational fluctuations. We identified Aβ-specific allosteric residues in the hemopexin domain by comparing residues having a normalized correlation greater than 0.8 with the catalytic motif residues for free and Aβ-bound MMP1. Our method of identifying substrate-specific and functionally relevant allosteric residues may enable modulating one MMP1 function without affecting the other functions and thereby making it possible to target MMPs with fewer side effects.

4.2 MMP1 dynamics on Aβ-induced aggregates

Using a prism-type TIRF microscope, we measured FRET between two dyes attached to the two domains of MMP1 (Figure 1A). To this end, we created mutants of active (E219) and inactive (Q219) MMP1 with two point mutations SER142C and S366C (Figure 1B) for labeling with Alexa555 (donor) and Alexa647 (acceptor), a pair of dyes used for FRET measurements. Previously, we showed that labeling does not affect the activity of MMP1. Inactive MMP1 acts as a control to distinguish the effects of enzymatic activity from the effects of the microenvironment and photophysical

properties of the dyes. We created a thin layer of water-insoluble Aβ-induced aggregates on a quartz slide (Figure 4.1c). We excited labeled MMPs using a 532 nm laser inside a flow cell as they interacted with Aβ aggregates. As MMP1 undergoes interdomain dynamics, the distance and hence, FRET between Alexa555 (donor) and Alexa647 (acceptor) changes leading to the anticorrelated emission from the two dyes (Figure 4.1d). When the two MMP1 domains are distant (open conformation), we get low FRET values due to high Alexa555 (I_D) and low Alexa647 (I_A) emissions. In contrast, when the two MMP1 domains are closer (closed conformation), we get high FRET values due to low Alexa555 (I_D) and high Alexa647 (I_A) emissions. We calculated FRET values using the equation $I_A/(I_A+I_D)$, where each FRET value determines the distance between the two MMP1 domains. Area-normalized histograms of FRET values without ligands (Figure 4.1e) suggest that MMP1 prefers closed conformation on Aβ aggregates. This is in contrast to the MMP1's preference for the open conformations on collagen, fibrin, and aSyn. Although we need more studies in the future to identify the reason for the substrate-dependent preference for the open and closed conformations, it is clear that substrates play an active role in MMP1 function. A sum of two Gaussians fits the histograms, suggesting an equilibrium of the open and closed conformations. In the presence of tetracycline, a known MMP inhibitor, both active and inactive MMP1 prefer the closed conformations more (Figure 4.1f). Previously, we argued that tetracycline holds the two MMP1 domains via hydrogen bonds, facilitating the preference for the closed conformations. We also calculated the correlation between conformations at different time points. We fitted both power-law and exponential

distributions to the autocorrelations and found that an exponential distribution fits the experimental autocorrelations (Figures 4.1g-h).

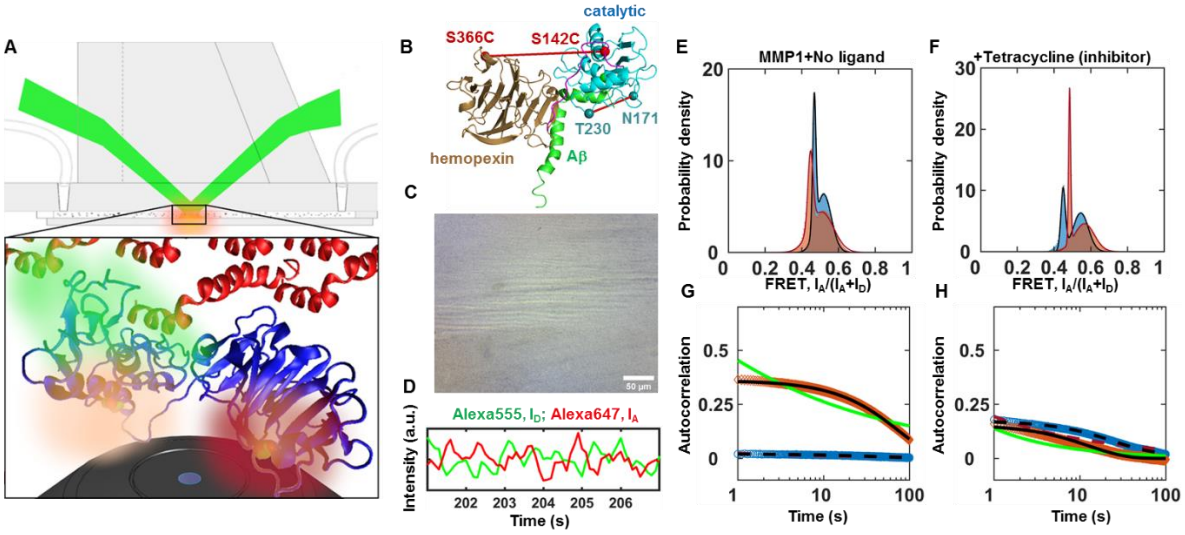

Figure 4.1. Interdomain dynamics of MMP1 on Aβ-induced aggregates at 22 ºC with 100 ms time resolution. (**a**) Schematics of smFRET measurements using a TIRF microscope. (**b**) One of many binding poses between MMP1 and Aβ. (**c**) Light microscopy image of Aβ-induced aggregates on a slide. (**d**) Emission intensities of Alexa555 and Alexa647 attached to active MMP1. (**e**) and (**f**) Area-normalized histograms of FRET values (~200,000 FRET values, bin size=0.005) without ligand and in the presence of tetracycline (an inhibitor), respectively, for active (blue) and inactive (orange) MMP1. All histograms are fitted to a sum of two Gaussians (active: solid black line; inactive: solid red line). (**g**) and (**h**) Normalized autocorrelations of FRET values without ligand and in the presence of tetracycline, respectively, for active (blue) and inactive (orange) MMP1. All autocorrelations are fitted to exponentials and power laws (exponential fit to active: dashed black line; power-law fit to active: dashed red line; exponential fit to inactive: solid black line; power-law fit to inactive: solid green line). The error bars in histograms and autocorrelations represent the square roots of the bin counts and the standard errors of the mean (SEM) and are too small to be seen.

4.3 A two-state Poisson process description of MMP1 dynamics on Aβ-induced aggregates

Recently, we published a quantitative analysis of MMP1 dynamics on collagen fibrils [163], fibrin [164], and aSyn aggregates. A two-state description of MMP1 dynamics allows for easier interpretation of conformational histograms and correlations. The best-fit parameters for the Gaussian fit centers define the two states S1 (low FRET)

and S2 (high FRET). The interconversion rates k1 (S1→S2) and k2 (S2→S1) between the two states from the ratio (k1/k2= the area of S2 divided by the area of S1) and sum (k1+k2= the decay rate of autocorrelation).

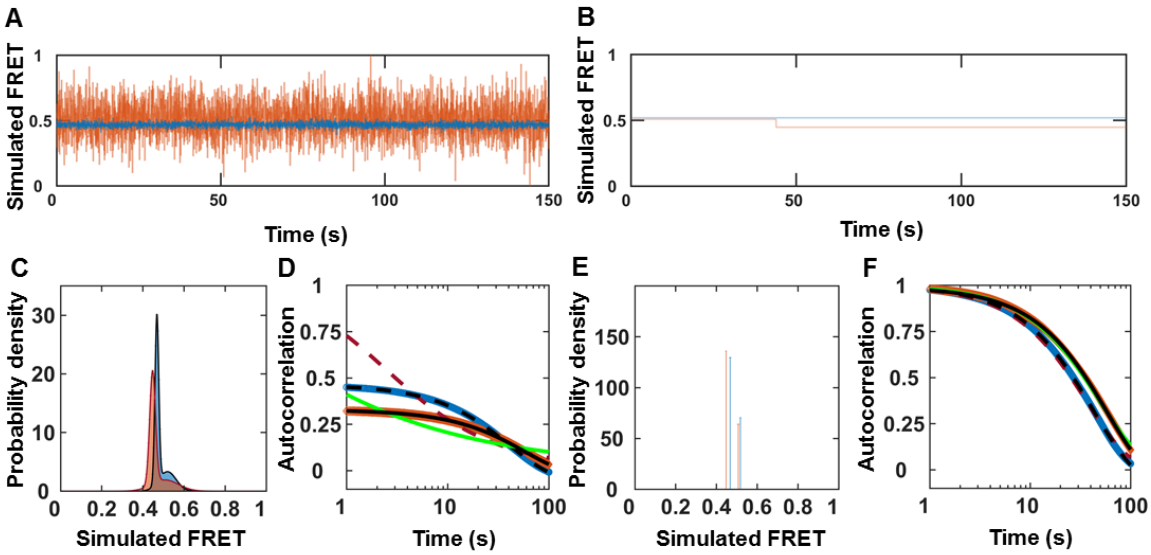

Figure 4.2. Stochastic simulation of MMP1 dynamics on Aβ as a two-state system. (**a**) and (**b**) Examples of simulated smFRET trajectories with and without noise, respectively, for active MMP1 (blue) and inactive MMP1 (orange) using experimental parameters for MMP1 without ligands. (**c**) Area-normalized histograms of simulated FRET values with noise (active: blue; inactive: orange) with best fits to a sum of two Gaussians (solid black line). (**d**) Autocorrelations of simulated FRET values with noise (active: blue; inactive: orange) with best fits to exponentials (active: dashed black line; inactive: solid black line). Power law does not fit autocorrelations (active: dashed red line; inactive: solid green line). (**e**) Area-normalized histograms of simulated FRET values without noise (active: blue; inactive: orange). (**f**) Autocorrelations of simulated FRET values without noise (active: blue; inactive: orange) with best fits to exponentials (active: dashed black line; inactive: solid black line). Both exponential and power law fit autocorrelations (active: dashed red line; inactive: solid green line). The error bars represent the standard errors of the means (SEM) for histograms and autocorrelations and are too small to be seen.

The two states are S1=0.47 and S2=0.52 on Aβ-induced aggregates for active MMP1 without ligand. In comparison, the two states are S1=0.44 and S2=0.55 on collagen [163], S1=0.42 and S2=0.51 on fibrin [164], and S1=0.46 and S2=0.52 on aSyn aggregates for active MMP1 without ligand. The correlation decay rate of 0.02 s^{-1} on Aβ-

induced aggregates for active MMP1 without ligand. In comparison, the decay rates are 0.13 s^{-1} on collagen [163], 0.08 s^{-1} on fibrin [164], and 0.08 s^{-1} on aSyn aggregates for active MMP1 without ligand.

We confirmed the validity of the two-state Poisson process approach to MMP1 dynamics by simulating and analyzing smFRET trajectories using experimentally determined S1, S2, k1, k2, and noise (widths of the histograms). We recovered the parameters by analyzing the simulated smFRET similar to the analyses of experimental smFRET.

Tetracycline changes the conformational distributions of MMP1 and associated interconversion rates, but the two-state description remains valid. Underlying noise can obscure the individual states (Figures 4.2a-b), but histograms (Figures 4.2c and Figure 4.2e) and autocorrelations (Figures 4.2d and Figure 4.2f) still recover the underlying parameters reasonably well. The presence of noise increases the width of conformational histograms, but subtly affects autocorrelations. In the absence of noise, both power-law and exponential distributions fit the autocorrelations (Figure 4.2f). However, with noise, the y-intercept of the autocorrelations decreases, and only an exponential distribution fits the autocorrelations. The decay rate of autocorrelations does not change as the noise level varies and an exponential fit recovers the underlying decay rate with and without noise. In other words, the presence of noise can convert a power-law correlation into an exponential correlation, similar to the conversion of a Lorentzian line shape into a Gaussian line shape by noise [165].

4.4 MD simulation of MMP1 dynamics

Since crystal structures of Aβ-bound MMP1 do not exist, we determined the binding poses of Aβ (PDB ID 1IYT) and MMP1 (PDB ID 4AUO) using molecular docking software ClusPro [166, 167]. We selected the best scoring pose (Figure 4.3a) and performed all-atom MD simulations at 37 °C for active and inactive MMP1. Figure 4.3b shows the distributions of S142-S366 distance, which shows that active MMP1 prefers closed conformations (high FRET) more than inactive MMP1, in agreement with experiments (Figure 4.1e).

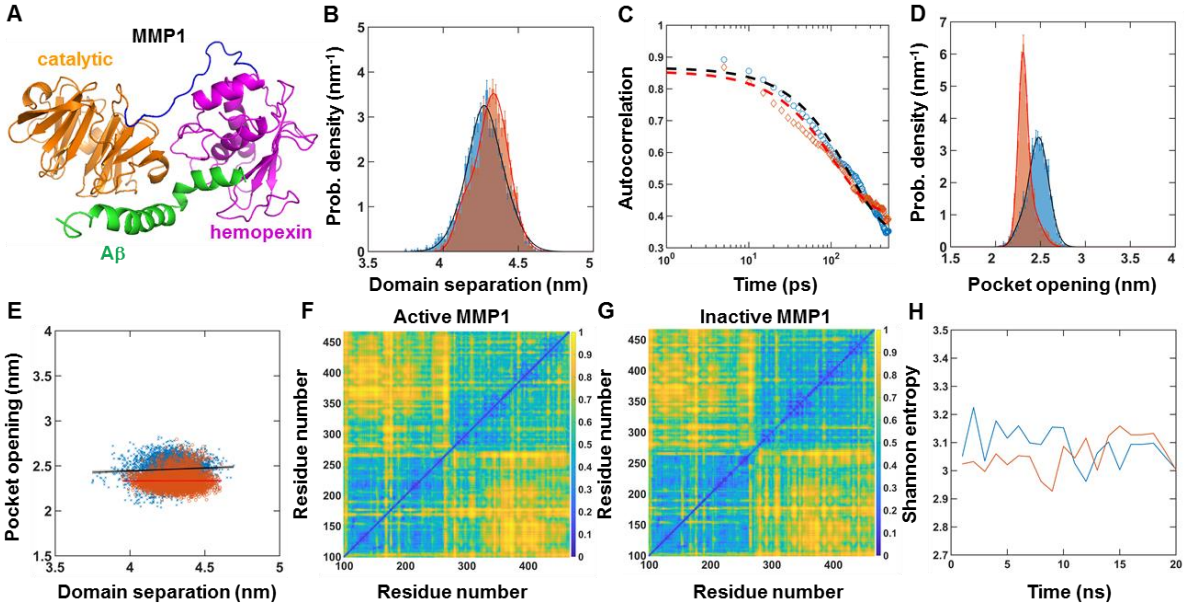

Figure 4.3. All-atom MD simulation of MMP1 interdomain dynamics on Aβ aggregates at 37 °C. (**a**) One of many binding poses between MMP1 and Aβ. (**b**) Area-normalized histograms of simulated interdomain distance (active: blue; inactive: orange) with best fits to a sum of two Gaussians (solid lines). (**c**) Autocorrelations of simulated interdomain distance (active: blue; inactive: orange) with best fits to exponentials (active: dashed black line; inactive: solid orange line). (**d**) Area-normalized histograms of simulated catalytic pocket opening (active: blue; inactive: orange) with best fits to a sum of two Gaussians (solid lines). (**e**) Linear correlation between the catalytic pocket opening and interdomain distance. (**f**) and (**g**) Correlations between residues for active and inactive MMP1, respectively. (**h**) Shannon entropy calculated from correlation plots for active (S=3.01±0.01, mean±SEM) and inactive (S=3.06±0.01, mean±SEM).

The simulated S142-S366 distance also shows correlations for active and inactive MMP1 (Figure 4.3c). We extracted further insights from simulations. First, active MMP1 shows a larger catalytic pocket opening (Figure 4.3d). A larger catalytic pocket opening likely enables substrates to get closer to the active site. Second, the correlation between the catalytic pocket opening and interdomain separation for active MMP1 is higher than inactive MMP1 (Figure 4.3e). This is consistent with previous reports of positive correlation between the catalytic pocket opening and interdomain separation for MMP1 dynamics on collagen, fibrin, and aSyn [163, 164].

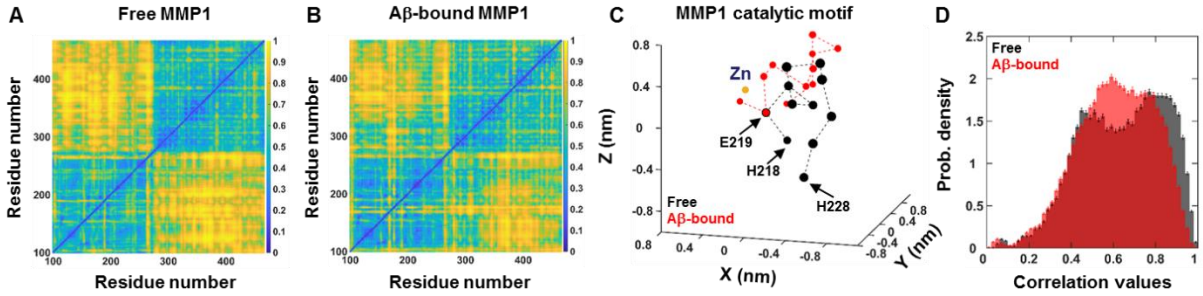

Figure 4.4. Conformational changes of the MMP1 catalytic motif and identification of Aβ-specific allosteric residues. (**a**) Normalized correlations between each pair of residue for free active MMP1 at 37 °C. (**b**) Normalized correlations between each pair of residue for Aβ-bound active MMP1 at 37 °C. (**c**) Three-dimensional configurations of the catalytic motif residues for free active MMP1 (black) and Aβ-bound MMP1 (red) at 37 °C. (**d**) Histograms of correlation values of free MMP1 (black) and Aβ-bound MMP1 (red).

We quantified fluctuations of the entire MMP1 using Shannon entropy. We calculated normalized correlations of fluctuations after subtracting the mean position from the entire time series. Figures 4.3f-g show the matrix of correlation values at lag number 1. We divided the correlation values to create 10 bins of width 0.1, calculated 10×10 gray-level co-occurrence matrix (GLCM), and defined Shannon entropy

$S = -\sum p_i \ln p_i$, where p_i is the probability of a microstate i. The catalytic domain residues (F100-Y260) have strong correlations with the hemopexin domain residues (D279-C466), suggesting allosteric communications in MMP1. The time-evolutions of Shannon entropy show similar values for active and inactive MMP1 (Figure 4.3h).

We defined the changes at the catalytic site and identification of allosteric residues on MMP1. We compared two-dimensional correlation plots of free (Figure 4.4a) and Aβ-bound MMP1 (Figure 4.4b) at 37 °C. We considered the catalytic residue E219 as the origin and plotted the pairwise distance between E219 and each of the catalytic motif residues HELGHSLGLSH in three dimensions. The symbol size at each location is proportional to the standard deviation of the pairwise distance (Figure 4.4c). The comparison reveals that the configuration at the MMP1 catalytic site changes considerably as free MMP1 binds Aβ.

Figure 4.4d shows the distributions of correlation values in Figures 4.4a-b. We used a threshold correlation value at 0.8, which is the peak probability density (~2) divided by e (~2.7). We found all the residues with normalized correlations greater than 0.8 in Figure 4.4a and Figure 4.4b with the catalytic motif residues HELGHSLGLSH. A comparison of the residues between free MMP1 and Aβ-bound MMP1 identified that 373 have exclusive correlations only for Aβ-bound MMP1. The identification of substrate-specific allosteric residues is significant because it may enable controlling one MMP1 function without affecting the other functions.

4.5 Summary

We conclude that MMP1 dynamics on Aβ aggregates depend on MMP1 activity and a two-state Poisson process describes the dynamics similar to MMP1 dynamics on collagen, fibrin, and aSyn aggregates. However, the two domains of MMP1 prefer closed conformations on Aβ aggregates, which is in contrast to the preference for open conformations on collagen fibril, fibrin, and aSyn aggregates. We calculated the kinetic rates of interconversion between the two states from histograms and correlations of FRET values. We performed molecular docking of MMP1 with Aβ using ClusPro, simulated MMP1 dynamics, and matched the experimental and simulated interdomain dynamics to identify an appropriate pose. We used simulations to create a two-dimensional map of correlations between every pair of MMP1 residues, which shows allosteric communications between the two MMP1 domains. We calculated a Gray Level Co-occurrence Matrix from the two-dimensional map of correlations and quantified MMP1 fluctuations by Shannon entropy. We identified the allosteric residues in the hemopexin domain by identifying residues having strong correlations with the catalytic motif residues. We identified that residue number 373 in MMP1 has Aβ-specific allosteric correlations with the catalytic motif by comparing residues for free and Aβ-bound MMP1. Molecular understanding of interactions between MMP1 and Aβ-induced aggregates and identified of substrate-specific allosteric residues may enable controlling MMP1 function selectively on Aβ.

4.7 Methods

This section will outline the material and methods for the experiments described in chapter 4. This includes the formation of the aggregate, the methodology for the

biochemical and biophysical analysis and conditions for MD and other *in silico* simulations.

4.7.1 Aβ aggregate formation

Gene optimization. The 42 amino acid FASTA sequence for Aβ peptide was taken from Protein Data Bank file 1IYT. To aid in the recombinant production of this protein, we optimized the amino acid sequence in Java Codon Adaptation Tool for expression in *Escherichia coli* (strain K12). This process ensured that the transcription of the DNA to RNA will produce codons that *E.coli* will accurately recognize to construct the full length 42 amino acid peptide. We inserted the optimized DNA sequence for 42-residue wild-type Aβ peptide into the pET21b+ vector between NdeI (N-terminal) and HindIII (C-terminal) restriction sites.

DAEFRHDSGYEVHHQKLVFFAEDVGSNKGAIIGLMVGGVVIA

Figure 4.5. Amino acid sequence for Aβ with 42 residues.

GACGCTGAATTCCGTCACGACTCTGGTTACGAAGTTCACCAC
CAGAAACTGGTTTTCTTCGCTGAAGACGTTGGTTCTAACAAA
GGTGCTATCATCGGTCTGATGGTTGGTGGTGTTGTTATCGCT

Figure 4.6. The DNA sequence for 42 residue Aβ peptide. Sequence optimized for expression in E.coli K12 strain using Java Codon Adaption Tool (JCat) [146].

Transformation. We prepared the plasmid containing the DNA sequence for Aβ peptide for transformation by adding Tris-EDTA buffer solution pH 8.0 (Sigma-Aldrich

Cat# 93283) to dilute the DNA to a concentration of 50 ng/µL. The transformation was carried out in *E.coli* strain Rosetta (DE3) pLysS E. coli(Millipore, Cat# 70956-4). We thawed 50 µL of cells on ice. Once thawed, we added 10 µL of plasmid at 50 ng/µL concentration and the cell-plasmid solution was kept on ice for 30 min. We then transferred cells to a hot water bath at 42 °C for 45 s and moved back to the ice for 5 min. 950 µL of super optimal broth with catabolite repression (SOC) media (Sigma-Aldrich, Cat# S1797) was added to the cells and incubated for 2 h at 37 °C. We spread 100 µL of growth on a plate containing ImMedia Amp Blue(Invitrogen, Cat# 45-0038) and incubated it for 48 h. The cells on the selection plate have ampicillin resistance from the pET21b+ vector and chloramphenicol resistance from the pLysS vector. To preserve the *E.coli* cells containing the recombinant DNA, we selected a single colony from the plate using a sterile inoculation loop and transferred it into 35 mL of sterile Luria Broth(LB) media with 35 µL of ampicillin at 100 mg/mL concentration and 35 µL of chloramphenicol at 34 mg/mL concentration. The selected colony had a distinct center with a blue tinge due to the breakdown of X-gal sugar present on the ImMedia Amp Blue selection plates. Cells grew for an additional 20 h in the LB media until OD_{600} 1.51 was reached. For long-term storage of the cells, we added 800 µL of *E. coli* culture to 500µL of 40% glycerol (Sigma-Aldrich, Cat# G5516) to create glycerol stocks that can be stored in -80 °C.

Growth of Rosetta (DE3) pLysS cells. We prepared 35 mL of seed culture in LB media (Sigma-AldrichL7658) from 3 mL of glycerol stocks. We added 35 µL of ampicillin at 100 mg/mL concentration and 35 µL of chloramphenicol at 34 mg/mL concentration. The seed culture was grown overnight for 22 h in a shaker incubator at 37 °C with 250

rpm orbital agitation until growth reached OD600 1.71 ± 0.05. The error was quantified at a 95% confidence interval (CI). We filled two 1 L conical flat-bottom glass flasks with 500 mL of LB media and sterilized them in an autoclave (Panasonic, Model# MLS-3781L) following the preset liquid sterilization program (121 °C for 15 min). Once the sterile media had cooled, we added ampicillin and chloramphenicol to the same concentration used in the seed culture. 15 mL of the seed culture was added to 500 mL sterile LB media with antibiotics and grown at 37 °C with 250 rpm orbital agitation. After the 2 hours and the growth had reach OD600 0.45 ± 0.04 (95%CI), we induced the cells in one flask with 500 µL of 1 M IPTG (ChemCruz, Cat# SC-202185B). The cells in the other flask were not induced with IPTG to serve as the negative control for IPTG-induced expression. After induction, we grew cells in both flasks for an additional 4 h in the incubator-shaker at 37 C with 250 rpm orbital agitation. We measured OD using a cell density meter (WPA Biowave, Model# C0800) to quantify the growth. The cells were harvested and centrifuged in 500 mL centrifuge tubes at 10000 rpm for 10 min using a fixed angle centrifuge (Sorvall Lynx 4000 centrifuge with F12-6X500rotor, Cat# 75006580). The IPTG induced cells yielded ~1 g of cells and the growth without IPTG yielded ~1.6 g of cells.

Protein aggregation induced by lysis and centrifugation. During attempts at purification, we learned that aggregation of Aβ peptide with *E.coli* cell components can be controlled by buffer and lysis conditions. To form the Aβ peptide aggregate, we reconstituted 1 g cell pellet in 7 mL of protein buffer with 5% Triton X-100 (50 mM Tris, 100 mM NaCl, 5% Triton X-100, pH 9.0) in a 15 mL tube. We then disrupted the cells using a sonicator (Branson Digital Sonifier, Model# BBT16031593A) at 10% amplitude

for 10 min total time (3 min 20 s with pulse ON) with a sequence of 10 s pulse ON and 20 s pulse OFF. We centrifuged the cell lysate at 10000 rpm for 10 min. A viscous string-forming aggregate was visible after centrifugation and made up ~5 mL of the total contents of the tube. We decanted the aggregate to a fresh 15 mL tube leaving a small insoluble pellet behind. We imaged the aggregate using a light microscope and found striations similar to aggregates of aSyn, another neuronal protein known to form amyloid structures, formed by a similar method of sonication and centrifugation in narrow tubes.

4.7.2 Measurements of MMP1 interdomain dynamics

For smFRET measurements of MMP1 interdomain dynamics, we mutated two serine residues in MMP1 at locations 142 and 366 to cysteines for labeling with Alexa555 and Alexa647 dyes. In addition, we introduced the E219Q mutation in the catalytic domain to create a catalytically inactive mutant of MMP1. We spread aSyn-induced aggregates and made a thin layer on a quartz slide. We made a flow cell for single-molecule experiments using a piece of double-sided adhesive tape sandwiched between the quartz slide and a glass coverslip. Labeled MMPs were flowed into the flow cell and excited at 532 nm wavelength using the evanescent wave created at the quartz slide and sample buffer interface in a Total Internal Reflection Fluorescence (TIRF) microscope. We acquired two-channel movies to detect emissions from Alexa555 and Alexa647. Any relative motion between the two MMP1 domains would lead to a non-radiative transfer of energy from Alexa555 to Alexa647 due to FRET, increasing the emission from Alexa647 (I_A) and simultaneously reducing the emission from Alexa555 (I_D). We calculated FRET efficiency by $I_A/(I_A+ I_D)$ [184]. Single-molecule experiments and analyses have been described in our previous publications [185-188].

4.7.3 All-atom simulations

We removed all zinc and calcium ions and the water molecules from PDB ID 4AUO and replaced the missing side-chain atoms using Chimera's rotamer tool. PDB files for active and inactive MMP1 were created by replacing A219 with E219 and Q219, respectively, using Pymol's mutagenesis function. We used Gromacs 2019.6 with the Gromos96 43a1 force field to perform the MD simulations. We ignore the hydrogen atoms while creating the topology file. Each simulation ran 20 ns long, simulated at 2 fs/step, and sampled every 5 ps. Each MMP1 crystal was placed in a cubic box with 3D period boundary conditions and solvated with water (using a single point charge model (SPC)) and Na counter-ions to create a neutral system. We then used the steepest descent algorithm to minimize the solution's energy. To equilibrate the solution with the protein complex, we used NVT and NPT ensemble simulations. First, we performed the NVT simulation and set the mean temperature at the desired temperature of 295 K (22 °C) or 310 K (37 °C) using a Berendsen thermostat for 100 ps. We used the Verlet cut-off scheme for neighbor searching and updated the neighbor list every 20 fs. We used the particle mesh Ewald scheme to calculate the electrostatic interactions with a cubic interpolation order of 4 and a cut-off at 1 nm. We assigned initial velocities using a Maxwell distribution from the corresponding temperature. In the NPT simulation, we maintained velocities from the NVT simulation output, and the pressure was set to 1 bar using a Parrinello-Rahman barostat for an additional 100 ps. Once the NVT and NPT simulations finished and the system equilibrated, we removed the position restraints and ran the production MD for 20 ns. We edited the final coordinates in the trajectory file to correct for periodicity and center the protein complex. The distances between the

catalytic pocket residues and the serine residues (interdomain distance) are then measured at every time step using the Gromacs distance function. We measured the interdomain separation between the nitrogen atoms of residues S142 and S366 and the catalytic pocket opening between the nitrogen atoms of residues N171 and T230. To calculate the correlation and Shannon entropy, we recorded the nitrogen atom's coordinates in each residue of MMP1.

4.7.4 Analysis of the experimental and simulated interdomain dynamics

We chose the histograms' bin width to be at least the inverse of the sample size's square root, i.e., $1/\sqrt{N}$, N is the number of data points. We calculated the error of count in each bin as the square root of the bin count. Both the bin counts and errors were divided by the area of the histogram to create the area-normalized histogram (probability density function). The area under the normalized histogram equals 1. We fitted a sum of two Gaussians to the histograms (Equation 3.1) : where a's, b's, and c's are amplitudes, centers, and widths of the Gaussians. The parameters b1 and b2 are the two states, S1 and S2.

To calculate correlations, we subtracted the average value from each trajectory and used the Equation 3.2: where C_τ is the correlation at lag number τ , N is the number of points in a FRET trajectory, and $I(t)$ is the FRET value at t. For autocorrelations, both factors in curly brackets were from the same time series. For cross-correlations, the two factors in curly brackets were from different time series.

We normalized correlations by dividing correlation values at each lag by $C_{\tau=0}$. We fitted correlations between $\tau = 1$ and $\tau = 1000$ to both power-law and exponential

distributions. For power law, we used a form of Pareto distribution [189] that satisfies the boundary conditions, i.e., $C_{\tau=0}=1$ at $t=0$ and $C_{\tau=\infty}=0$ at $t=\infty$.

We fitted the equations of power-law (Equation 3.3) and exponential functions (Equation 3.4) To quantify correlations between the catalytic pocket opening and interdomain separation from simulations, we used the interdomain distance as the single predictor variable for the catalytic pocket distance in a linear model. A linear model describes a response variable as a function of predictor variables. Linear models are often fit using a method known as statistical regression. There are different regression methods used, depending on the number of predictor variables. When using only one predictor variable, the regression method is known as the simple linear regression, which we used for quantifying correlations. We used Equation 3.5: where b_0 and b_1 are the estimated fit parameters. There are also a few different methods to estimate the parameters of the linear model. The most-used approach is the least-squares operator, which finds the slope through the data that minimizes the squared distance between the fit and the residues. There is still uncertainty in these estimations, no matter which method we used. Confidence bands visually represent the uncertainty in linear models by showing the range of possible slopes. We calculated the 95% confidence interval of each predictor value's mean

CHAPTER FIVE

SUMMARY AND FUTURE WORK

5.1 Introduction

AD and PD are often characterized by the presence of protein aggregates rich in aSyn or Aβ, respectively [6, 33]. New evidence suggests a prion-like spread of these aggregates from the enteric nervous system to the central nervous system[205]. The aggregation of these proteins into amyloid fibrils specifically provides an interesting area of study for structural biologists, neuropathologists, and medical diagnosticians as the inherent presence of aggregates does not exclusively define all these diseases but may indicate a subset of each disease that shares a common trigger and neuropathology. Matrix metalloproteases may provide this trigger while supporting the gut-brain axis of neurodegeneration.

The identification of specific triggers for these diseases will also identify therapeutic targets. For that reason, the purpose of this chapter is to propose an extension of the previous work in this thesis to fill a critical void in our understanding of AD and PD pathogenesis by exploring the gut-brain axis and identifying specific therapeutic targets in the form of metalloproteases.

5.1.1 Amyloid fibrils

Amyloid fibrils are a type of protein structure in which a protein monomer forms as β- sheet and stacks with other monomers. Amyloid fibrils are commonly seen in nature in bacterial biofilms, infectious prions, and aggregates involved in neurodegeneration [6, 28, 32, 33, 75, 76]. The amyloid fibril formation associated with

neurodegeneration is currently thought to be caused by overexpression, genetic mutation, or cleavage of precursors affecting the stability of the protein in its native form [71, 72]. A common protein found in PD and AD amyloid aggregates is aSyn and there is evidence that the C-terminal truncation of aSyn by protease leads to aggregation and fibril formation [77]. In PD and some forms of dementia, these fibrils can aggregate into larger intracellular structures known as Lewy Bodies. In terms of AD, Aβ peptide is mainly implicated in the amyloid fibril formation [33]. Aβ peptide is a fragment of a larger transmembrane protein known as APP. When this protein is cleaved and secreted into the extracellular space by secretase, it can yield the 40 and 42 amino acid fragments known as Aβ peptide which is prone to aggregation into amyloid fibrils [206]. However, the presence of Aβ42/Aβ40 does not exclusively define AD pathology as the methods of Aβ peptide aggregation, breakdown, and transport across the blood-brain barrier are also being studied as part of AD pathology [71, 72]. Balancing the levels of Aβ peptide in the brain is achieved by proteolytic degradation, and active transport out of the brain. There is a growing body of evidence that the proteolytic cleavage of Aβ peptide and its aggregate play an important role in understanding AD [73]. The proteolytic degradation may take place by a cell-mediated immune response, or proteins within the extracellular space.

5.1.2 Why MMPs

Matrix-metalloproteases are a 23-member family of zinc-dependent enzymes with a conserved catalytic motif. The proteases are commonly understood for their ability to cleave extracellular matrix proteins as well as some biomolecules [207]. Additionally, MMP1 has shown the ability to cleave other non-extracellular substrates

such as fibrin, and bacterial biofilms [30, 31]. A major component of bacterial biofilms is an amyloid aggregate structure [32]. If MMP1 can breakdown bacterial biofilms, which are rich in amyloid fibrils, this may hint at its ability to break down the amyloid aggregates present in ~50% of AD and PD patients[6, 33]. Additionally, MMPs and their analogs have also been studied for their ability to cleave aSyn, APP, and Aβ peptide [34, 35].

The structure of MMP1 makes it a suitable target and model for the MMP family. MMPs have a highly conserved catalytic motif. The structure of MMP1 includes a catalytic domain that performs the breaking of peptide bonds, a hemopexin domain that is involved in substrate specificity, a linker region joining the two, and a pro-domain that blocks the catalytic site until activation by other MMP1, plasmin, or trypsin. The linker region makes MMP1 a highly flexible molecule that exhibits interdomain distance changes on the order of 1 nm. These domain motions are also observed during molecular dynamic simulation over a 10-nanosecond time interval indicating simulations may be able to accurately represent the protein dynamics even at small time scales [29]. The hemopexin domain's involvement in substrate specificity makes it an ideal target for allosteric control [29]. MMP1 is also associated with AD and PD risk factors such as diabetes, heart disease, stroke, and periodontitis [208-215].

5.1.3 The gut-brain axis of AD and PD

The gut-brain axis describes the communication between the gut and brain through stimulation, excretion, regulation, and the physical connection along the vagus nerve. There has been a growing interest in the role of the gut-brain axis in recent years centered around the microbiome. The human microbiome contains approximately the

same number of cells as the human body [216]. Bacteria make up most of these microorganisms. Within the intestines, bacteria can produce and excrete a vast variety of proteins that aid in our digestion. *Enterococcus faecalis* is a bacterium found in our gut that can produce a bacterial analog of MMP. This protein is called gelE and has been known to activate our own endogenous MMPs and begin to degrade the lining of our intestines [217].

Just beyond the intestinal wall and past the basement membrane of our epithelial cells lies smooth muscle and the enteric nervous system. The enteric nervous system contains a region known as the myenteric plexus where nerves and their shepherding cells call enteric glial cells to regulate your secretions and excretions. Enteric glial cells are also capable of producing a variety of MMPs including MMP2, and MMP9 [218, 219].

In 2002 the Braak hypothesis was introduced which asserted that aSyn aggregates, known as Lewy Bodies, can begin in the gut and spread along the vagus nerve to the brain in PD patients [205]. This was supported by a staging of Parkinson's symptoms beginning with reduced gut motility, progressing to sleep disturbances by the involvement of the reticular formation in the brain stem, and finally the classical parkinsonian tremor by the destruction of the dopaminergic cells of the substantia nigra [205, 220, 221]. Since the introduction of this hypothesis, numerous studies have expanded upon this amyloid aggregate spreading in a prion-like manner in both PD and AD [222, 223].

Many people have theorized that the aggregation in PD is caused by genetic mutations in aSyn sequence or expression [224-226]. However, PD can develop in an

absence of these genetic traits [227]. Further association has been made with various microorganisms, but no direct cause and route have been identified [228, 229]. MMPs may be a prime candidate for this missing link tying the gut-brain axis into both PD and AD. MMPs can use their ability to restructure the extracellular matrix to cross the boundary between the intestinal lumen and vulnerable neuronal cells. Additionally, the expression of MMPs within our immune system keeps them in close proximity to our nervous system. MMPs may provide the perfect bridge for the gut-brain axis of PD and AD.

5.1.4 *C. elegans* as a model organism

C. elegans have long been used as biological models specifically for neurodegeneration [230-232]. All neurons and their lineage have been mapped within *C. elegans* [233]. This includes 8 dopaminergic neurons, which are the neurons specifically affected by the aSyn aggregates of PD[234, 235]. Additionally, humans share approximately 80% homology with proteins present in *C. elegans* [236]. APP does have a homolog in *C. elegans*, but there is no homolog of aSyn present in *C. elegans* [232]. Using transgenic systems, aSyn has been introduced to *C. elegans* to study PD.

However, of all the *C. elegans* models of PD, none are suitable to exam whether C-terminal truncation by MMPs can lead to a toxic amyloid seed being produced that can further seed aggregation. This is because all models are conjugated with fluorescent proteins such as GFP, YFP, and mCherry [237]. C-terminal truncation of these aSyn molecules would separate the dye make the aggregate untraceable by typical fluorescence. Hence, we will create our model of PD in *C. elegans* without

fluorescent proteins with the intent to further explore the modulation of MMP-1 activity on preventing and causing aggregation.

5.2 Seeding amyloid fibril formation

We hypothesize that MMPs expressed in the myenteric plexus by enteric glial cells can cleave monomeric aSyn and Aβ peptide to produce a toxic species capable of seeding amyloid formation. Our premise relies on studies that show MMP1 is capable of cleaving aSyn and APP. Spillantini et al. has shown that C-terminal truncation of aSyn leads to aggregation [77]. The presence of aSyn can increase MMP expression [238]. MMPs are capable of C-terminal truncation of aSyn and increasing aSyn aggregation, but we do not know if these fragments can seed further aggregation in full form aSyn [239]. Studies indicate that aggregates can spread in a prion-like fashion in both AD and PD patients discussed previously. This is further supported by *in vitro* models in which an amyloid seed is added to monomeric aSyn or Aβ peptide and promotes fibril formation [240-242]. The ability for MMP and its analogs to initiate amyloid seeding is crucial to being able to implicate MMPs as a trigger for the gut-brain axis of PD and AD. The gut-brain connection is not an abstract concept, but rather the physical connection of the enteric nervous system and central nervous system by the vagus nerve. If a misfolded toxic amyloid fragment can enter the nervous system, it will spread along synapses to the brain. This is theorized to be the reason many PD patients show a progression of symptoms beginning with lack of motility in the intestines and progressing to sleep disturbances and finally the classical parkinsonian symptoms of tremor [205]. In anatomical terms, this neural dysfunction in an ascending fashion from the gut, through the brain stem, and into the substantia nigra. These experiments will

allow us to determine if MMP1, other MMPs, or MMP analogs can form an initial amyloid seed that can induce amyloid fibril formation in monomeric aSyn and Aβ peptide. Furthermore, this study will allow us to rapidly screen inhibitors and complements of the proteolytic process leading to toxic aggregate formation. We will study MMP1, MMP9, bacterial collagenase gelE, and the viral protease from SARS-CoV-2 called 3CLpro.

5.2.1 Observe partial cleavage of aSyn and Aβ by MMPs

To see if MMP1 is capable of creating amyloid fibrils, we will first assess MMP1's ability to cleave aSyn and Aβ peptide as C-terminal truncation of aSyn specifically has been implicated in promoting its aggregation. We will test this by serial diluting MMP-1 and use it to treat 50 µg/mL of monomeric aSyn and Aβ peptide. The digestions will be incubated at 37 °C and sampled every 30 minutes for 6 hours. Once a sample is collected, it will be treated with SDS containing Lamelli sample dye and stored in -20 °C to halt the reaction. Once all reactions are collected, SDS-PAGE will be used to analyze the fragmentation of aSyn and Aβ peptide. The experiment will be repeated with inactive MMP-1 and in the presence of inhibitors such as tetracycline. Additionally, the experiment will be repeated with MMP-9, gelE and 3CLpro.

We expect that after 6 hours of treatment MMP1 will fully digest aSyn and Aβ peptide. However, at some combination of dilution and treatment time, aSyn and Aβ peptide will be only partially cleaved. This is the dilution and time we will use in section 5.2.2 to attempt to seed amyloid fibril formation. Observing fragments may be difficult by traditional SDS-PAGE so we may alternatively use Tricine SDS-PAGE as it has been shown to more effectively small molecular weight proteins [243]. It may also be possible

that no fragmentation is observed at all in aSyn or Aβ peptide. In this case, it may be that fragments are too small to observe, or MMP1 will not cleave the monomeric forms of the proteins. In this case, we will still proceed with the study discussed in section 5.2.2 for interaction other than cleavage with MMP1 may form an amyloid fibril capable of seeding further formation.

5.2.2 Seed amyloid fibril formation

Using the MMP dilution we determined in section 5.2.1 results, we will treat 3 mL of 50 μg/mL monomeric aSyn, Aβ peptide. Treatment will be again performed at 37 °C. Additionally, control samples will include a sample without MMP added and a sample without either monomeric aSyn or Aβ peptide. After time determined in study 5.2.1, the sample will be removed from incubation and placed in a centrifuge filter tube capable of filtering the protease while allowing aSyn or Aβ peptide to pass through. In the case of MMP1, gelE, and 3CLpro, this will be to 30 kDa cutoff tube. For MMP9, a 50 kDa cutoff filter tube will be used. After timed digestion, samples will be centrifuged at 5,000 RPM for 20 minutes. The flow-through should now contain fragments of either aSyn or Aβ peptide that we will explore as toxic fragments capable of seeding amyloid. We will use the seeding solution to treat monomeric aSyn and Aβ peptide in the presence of 50 μM thioflavin T (ThT) as this has been established as a dye capable of staining amyloid fibrils [244]. ThT is a dye that ThT emits a stronger fluorescence upon binding to the β-sheet conformation of amyloid fibrils. We will use a Total Internal Reflection Fluorescence Microscope (TIRFM), and UV-Vis to quantify amyloid fibril formation in the presence of ThT [245]. Fibrilization kinetics will be measured according to previous

publications [245]. During this experiment, we will also explore whether an aSyn fibril seed can seed amyloid fibril formation in Aβ peptide and vice versa.

We expect to see fibril formation in monomeric aSyn and Aβ peptide as indicated by increased fluorescence in UV-vis and by direct tracking of fibril length in the TIRFM. Data from the TIRFM will provide use not only fibrilization kinetics but also insight into possible abnormalities in the amyloid structure such as branching. An area of concern is the use of ThT because it has been suggested that ThT changes fibrilization kinetics [246]. ThT concentration may also need adjustment for proper detection in TIRFM. Congo red may be used as an alternative for ThT in UV-vis but its use in TIRFM on amyloid fibrils has not been established. Additionally, congo red does not change fluorescence upon binding as ThT does so quantification of fibrilization kinetics would not be possible unless serious modification to experiment design was made to include effective washing of excess dye. We expect this experiment to provide evidence that MMPs expressed in the presence of aSyn or Aβ peptide in the myenteric plexus can result in the formation of a toxic amyloid fibril capable of further seeding amyloid formation. Thus, implicating MMPs as a trigger for PD and AD along the gut-brain axis

5.3 Screen allosteric inhibitors of MMP1 activity on formation of amyloid fibril seeds

We hypothesize we can exert allosteric control of MMP1 and inhibit its ability to partially cleave aSyn and Aβ peptide while leaving its ability to degrade amyloid fibrils and collagen intact. Our premise relies on preliminary studies where we can determine regions in the hemopexin domain of MMP1 that have a high correlation with the catalytic motif. These allosteric sites in the hemopexin domain are unique to different substrate

binding and can hence be targeted by different molecules in virtual screening. Molecules identified as targets within this virtual screening can be tested in the methods described 5.2.1 and 5.2.2. If a molecule is identified that limits the ability for MMP1 to form a toxic amyloid aggregate, while maintaining its ability to degrade aggregates, it could be valuable therapeutic worth testing in animal models such as *C. elegans* and mice.

5.3.1 Lead molecule screening against MMP-1 binding to different substrates

First, molecular docking of MMP1 (PDB ID: 4AUO) and Aβ peptide (PDB ID 1IYT) will be performed using ClusPro selecting for poses that place the catalytic site of MMP1 on Aβ peptide. Additional docking will be done with MMP-1 and the fibril forms of aSyn (PDB ID 2N0A) and Aβ peptide (PDB ID 2MXU) selecting for poses that place the catalytic site of MMP-1 along the stacked β-sheets of the fibrils. Molecular dynamic simulations will be performed as previously reported. We will track the domain separation and catalytic pocket opening of each selected pose and eliminate poses that do not have a positive correlation between the two as we believe this represents the functional dynamics of MMP1 needed for cleavage. We will perform auto-correlation on all amino acids as previously reported and isolate residues in the hemopexin domain that are highly correlated to the catalytic motif. We will use these allosteric residues as targets for virtual drug screening against 1400 FDA-approved lead molecules as previously reported. We will finally find overlap between screenings and attempt to find molecules with a high affinity that can inhibit MMP1 activity on monomeric aSyn and Aβ peptide while leaving the ability to cleave amyloid fibrils intact. These results will be validated *in vitro* in section 5.2, and eventually in a *C. elegans* model described in

section 5.4. This will provide evidence for the gut-brain connection of PD and AD while also screening for therapeutic targets.

We expect unique allosteric targets will be found for each substrate studied in MMP1. The residues should have an auto-correlation value greater than 0.8 and will be used as targets in ligand binding software. A limitation of this experiment may well be the computational power available. Previously, MD simulation and virtual screening have been performed on home workstations. Moving forward, we will utilize the High-Performance Computing group at Colorado School of Mines to get access to a node on a supercomputer capable of much faster simulations.

5.4 Construct a *C. elegans* model to demonstrate amyloid fibril spreading facilitated by MMPs

We hypothesize that a *C. elegans* model of amyloid spreading in PD can be created without conjugating fluorescent dyes and the aggregation can be seeded from the external environment. The purpose of this model is that dye conjugated aSyn will not behave in a similar structural way to native aSyn and cannot support a model where C-terminal truncation initiates amyloid formation. Our premise relies on previous studies that have introduced aSyn into the expression of the 8 dopaminergic neurons of *C. elegans*. These neurons serve as motor-sensory neurons that interface with the outside environment. Previous studies using *C.elegnas* have had limited success in observing fibril formation without introducing a genetic mutation into the aSyn sequence. We will then feed nematodes *E.coli* rich in amyloid aggregates. By using immunofluorescence, we can image the amyloid aggregates in the amyloid-fed *C. elegans* and compare them to a control group.

5.4.1 Image protein aggregates in *C. elegans*

We will first determine how to image amyloid structures in *C. elegans* using the TIRFM at the disposal of our lab group or a confocal microscope. Nematodes will be handled and cultured under standard methods [247]. We will culture *C. elegans* already showing amyloid fibril formation such as strain PE871 for aSyn which is available for purchase from the Caenorhabditis Genetics Center (CGC). *C.elegnas* will be fixed using paraformaldehyde as previously described to immobilize and prepare them for immunofluorescence measurements [248]. *C. elegans* will be treated with primary antibodies from abcam (ab209538) for aSyn, following previous protocols. Secondary antibodies used will be conjugated with Alexa Flour555. We will try imaging in quartz flow cells and flow cells with microfluidic channels for the TIRFM. If we are unsuccessful, we will use traditional methods of confocal microscopy reported in numerous publications imaging amyloid aggregates in *C. elegans* [249-255]**.**

5.4.2 Feeding *C. elegans* amyloid ladened *E.coli*

Next, we will determine if *C. elegans* can uptake amyloid fibrils by eating amyloid ladened *E.coli*. Wild type *C. elegans* (N2 Bristol) being fed the amyloid containing *E.coli* will be imaged every 2 days for uptake into their nervous system or the enterocytes surrounding the intestinal lumen. Because *C. elegans* have no aSyn orthologs, the initial amyloid seed will not spread through the nervous system unless the gene is introduced. We will create a plasmid suitable for *C. elegans* that express aSyn in dopaminergic neurons under the control of the dat-1 promoter according to previous methods, however, GFP will not be added [251, 256]. The plasmid will be injected into the gonads of young adult hermaphrodite N2 worms and integrated into chromosomes using UV

irradiation as previously described [256]. *C. elegans* will be cultured into stable stocks for storage. Once stocks are established, transgenic *C. elegans* will be cultured and then lysed using mechanical lysis. Lysates will be run in SDS-PAGE and Western Blotting using aSyn antibody to confirm expression. Once the expression is established, the transgenic *C. elegans* will now feed the *E.coli* ladened with amyloid aggregates while others will be fed a control *E.coli*. *C. elegans* cultures will be sampled every 2 days and imaged using immunofluorescence described previously. In summary, our goal is to first determine if we can image amyloid aggregates in *C. elegans* within our lab. We will next see if amyloid fibrils can be uptake into the nervous system from the outside environment or intestinal lumen. Finally, we will create a *C. elegans* strain that expresses aSyn in dopaminergic neurons and determine if amyloid fibrils present in the environment can seed enhanced aggregation across neurons as compared to *C. elegans* not being feed amyloid aggregates.

5.4.3 Native MMP overexpression

C. elegans have 6 matrix metalloprotease orthologs that are capable of cleaving MMP peptide substrates and they are inhibited by human tissue inhibitors of MMP, suggesting that the catalytic sites are closely related [257-259]. We hypothesize that we can suppress or overexpress these genes to modulate amyloid fibril propagation in *C. elegans* either expressing aSyn in dopaminergic neurons, or *C. elegans* being fed amyloid fibrils.

5.5 Summary

While MMPs are essential to the development and wound healing of many organisms, there is still much we do not know the full spectrum of its functions and dynamics. We have also shown that MMP1 can act on a variety of different substrates besides extracellular matrix components. Using biophysical methods to study the contribution of MMPs to different disease states increases our understanding of MMP dynamics and the diseases themselves. The findings in Chapters 3 and 4 have shown that the dynamics of MMP1 can vary based on the substrate chosen where the smaller sized Aβ peptide needs the domains of MMP1 to be in a more closed conformation during cleavage as compared with the more open conformation shown on aSyn. The flexibility, dynamics, and allosteric communication of MMP1 allow it to have a variety of uses *in vivo* that can possibly be modulated by the binding of small molecules such as tetracycline, and Plerixafor.

Regarding the gut-brain axis of neurodegeneration, MMPs should be closely considered for future study. The ability for MMPs to break down extracellular matrix provides a route of infiltration of the CNS through both the intestinal lining and even the blood-brain barrier. While initial studies have shown MMPs can partially cleave aSyn and APP leading to aggregation, we can expand on this understanding by implementing the methods of smFRET, molecular docking, all-atom simulations, and autocorrelations discussed in this document. The MMP-mediated gut-brain axis of PD and AD would be strengthened by the ability to visualize amyloid fibril formation and spreading in a living system. The future work discussed in section 5.4 may allow for this visualization in *C. elegans* and will advance the hypothesis put forth by Braak et al. in 2002.

Understanding the source of diseases has been at the center of improving human health since germ theory was proposed in 1762. With there being nearly 7 million patients diagnosed with PD or AD and a large aging population, elucidating and modulating the route of disease progression will have an impact on many lives. The properties of MMPs as a flexible broad-spectrum protease with allosteric communication make it an ideal target for study as a mechanism of the gut-brain axis. The findings of this thesis suggest the interactions of MMP1 with the amyloid fibrils present in some AD and PD patients is worth further study for both academic and medical purposes.

REFERENCES

[1] L. W. Harwell. "The Challenge of Neurodegenerative Diseases." Harvard MeuroDiscovery Center. https://neurodiscovery.harvard.edu/challenge (accessed 05/01/2021, 2021).

[2] A. J. Espay *et al.*, "Revisiting protein aggregation as pathogenic in sporadic Parkinson and Alzheimer diseases," *Neurology,* vol. 92, no. 7, pp. 329-337, 2019.

[3] J. E. Siegler and S. Galetta, "Editors' note: Revisiting protein aggregation as pathogenic in sporadic Parkinson and Alzheimer diseases," *Neurology,* vol. 94, no. 3, pp. 143-143, 2020.

[4] P. Nelson, "Reader response: Revisiting protein aggregation as pathogenic in sporadic Parkinson and Alzheimer diseases," *Neurology,* vol. 94, no. 3, pp. 143-144, 2020, doi: 10.1212/wnl.0000000000008821.

[5] E. J. Chung, G. M. Babulal, S. E. Monsell, N. J. Cairns, C. M. Roe, and J. C. Morris, "Clinical features of Alzheimer disease with and without Lewy bodies," *JAMA neurology,* vol. 72, no. 7, pp. 789-796, 2015.

[6] L. Parkkinen, T. Pirttilä, and I. Alafuzoff, "Applicability of current staging/categorization of α-synuclein pathology and their clinical relevance," *Acta neuropathologica,* vol. 115, no. 4, pp. 399-407, 2008.

[7] J.-P. Taylor *et al.*, "New evidence on the management of Lewy body dementia," *The Lancet Neurology,* vol. 19, no. 2, pp. 157-169, 2020.

[8] W. M. Holmes, C. L. Klaips, and T. R. Serio, "Defining the limits: Protein aggregation and toxicity in vivo," *Critical reviews in biochemistry and molecular biology,* vol. 49, no. 4, pp. 294-303, 2014.

[9] P. Yan *et al.*, "Matrix metalloproteinase-9 degrades amyloid-β fibrils in vitro and compact plaques in situ," *Journal of Biological Chemistry,* vol. 281, no. 34, pp. 24566-24574, 2006.

[10] D. Rodríguez, C. J. Morrison, and C. M. Overall, "Matrix metalloproteinases: what do they not do? New substrates and biological roles identified by murine models and proteomics," *Biochimica et Biophysica Acta (BBA)-Molecular Cell Research,* vol. 1803, no. 1, pp. 39-54, 2010.

[11] C. J. Morrison, G. S. Butler, D. Rodríguez, and C. M. Overall, "Matrix metalloproteinase proteomics: substrates, targets, and therapy," *Current opinion in cell biology,* vol. 21, no. 5, pp. 645-653, 2009.

[12] P. G. Jobin, G. S. Butler, and C. M. Overall, "New intracellular activities of matrix metalloproteinases shine in the moonlight," *Biochimica et Biophysica Acta (BBA)-Molecular Cell Research,* vol. 1864, no. 11, pp. 2043-2055, 2017.

[13] M. R. Acharya, J. Venitz, W. D. Figg, and A. Sparreboom, "Chemically modified tetracyclines as inhibitors of matrix metalloproteinases," *Drug Resistance Updates,* vol. 7, no. 3, pp. 195-208, 2004.

[14] C. Balducci and G. Forloni, "Doxycycline for Alzheimer's disease: fighting β-amyloid oligomers and neuroinflammation," *Frontiers in pharmacology,* vol. 10, 2019.

[15] M. Bortolanza *et al.*, "Tetracycline repurposing in neurodegeneration: focus on Parkinson's disease," *Journal of Neural Transmission,* vol. 125, no. 10, pp. 1403-1415, 2018.

[16] H. Mizoguchi, K. Yamada, and T. Nabeshima, "Matrix metalloproteinases contribute to neuronal dysfunction in animal models of drug dependence, Alzheimer's disease, and epilepsy," *Biochemistry research international,* vol. 2011, 2011.

[17] A. Leake, C. Morris, and J. Whateley, "Brain matrix metalloproteinase 1 levels are elevated in Alzheimer's disease," *Neuroscience letters,* vol. 291, no. 3, pp. 201-203, 2000.

[18] J. Levin *et al.*, "Increased α-synuclein aggregation following limited cleavage by certain matrix metalloproteinases," *Experimental neurology,* vol. 215, no. 1, pp. 201-208, 2009.

[19] J. Y. Sung *et al.*, "Proteolytic cleavage of extracellular secreted α-synuclein via matrix metalloproteinases," *Journal of Biological Chemistry,* vol. 280, no. 26, pp. 25216-25224, 2005.

[20] G. A. Rosenberg, "Matrix metalloproteinases and their multiple roles in neurodegenerative diseases," *The Lancet Neurology,* vol. 8, no. 2, pp. 205-216, 2009.

[21] M. Ahmad, T. Takino, H. Miyamori, T. Yoshizaki, M. Furukawa, and H. Sato, "Cleavage of amyloid-β precursor protein (APP) by membrane-type matrix metalloproteinases," *Journal of biochemistry,* vol. 139, no. 3, pp. 517-526, 2006.

[22] S. Higashi and K. Miyazaki, "Novel processing of β-amyloid precursor protein catalyzed by membrane type 1 matrix metalloproteinase releases a fragment lacking the inhibitor domain against gelatinase A," *Biochemistry,* vol. 42, no. 21, pp. 6514-6526, 2003.

[23] M. Gough, C. Parr-Sturgess, and E. Parkin, "Zinc metalloproteinases and amyloid Beta-Peptide metabolism: the positive side of proteolysis in Alzheimer's disease," *Biochemistry research international,* vol. 2011, 2011.

[24] M. Hernandez-Guillamon *et al.*, "Sequential amyloid-β degradation by the matrix metalloproteases MMP-2 and MMP-9," *Journal of Biological Chemistry,* vol. 290, no. 24, pp. 15078-15091, 2015.

[25] T. Saido and M. A. Leissring, "Proteolytic degradation of amyloid β-protein," *Cold Spring Harbor perspectives in medicine,* vol. 2, no. 6, p. a006379, 2012.

[26] M.-C. Liao and W. E. Van Nostrand, "Degradation of soluble and fibrillar amyloid β-protein by matrix metalloproteinase (MT1-MMP) in vitro," *Biochemistry,* vol. 49, no. 6, pp. 1127-1136, 2010.

[27] C. Marras *et al.*, "Prevalence of Parkinson's disease across North America," *npj Parkinson's Disease,* vol. 4, no. 1, 2018, doi: 10.1038/s41531-018-0058-0.

[28] "Facts and Figures." Alzheimer's Association. https://www.alz.org/alzheimers-dementia/facts-figures (accessed 05/01/2121, 2021).

[29] S. Kamboj *et al.*, "Quantification of allosteric communications in matrix metalloprotease-1 on alpha-synuclein aggregates and substrate-dependent virtual screening," Colorado School of Mines, 2021.

[30] L. Kumar, C. R. Cox, and S. K. Sarkar, "Matrix metalloprotease-1 inhibits and disrupts Enterococcus faecalis biofilms," *PLOS ONE,* vol. 14, no. 1, p. e0210218, 2019, doi: 10.1371/journal.pone.0210218.

[31] L. Kumar *et al.*, "Activity-dependent interdomain dynamics of matrix metalloprotease-1 on fibrin," *Scientific Reports,* vol. 10, no. 1, 2020, doi: 10.1038/s41598-020-77699-3.

[32] M. Andreasen *et al.*, "Physical Determinants of Amyloid Assembly in Biofilm Formation," *mBio,* vol. 10, no. 1, 2019, doi: 10.1128/mbio.02279-18.

[33] E. J. Chung, G. M. Babulal, S. E. Monsell, N. J. Cairns, C. M. Roe, and J. C. Morris, "Clinical Features of Alzheimer Disease With and Without Lewy Bodies," *JAMA Neurology,* vol. 72, no. 7, p. 789, 2015, doi: 10.1001/jamaneurol.2015.0606.

[34] M. Ahmad, T. Takino, H. Miyamori, T. Yoshizaki, M. Furukawa, and H. Sato, "Cleavage of Amyloid-β Precursor Protein (APP) by Membrane-Type Matrix Metalloproteinases," *The Journal of Biochemistry,* vol. 139, no. 3, pp. 517-526, 2006, doi: 10.1093/jb/mvj054.

[35] M. Brkic, S. Balusu, C. Libert, and R. E. Vandenbroucke, "Friends or Foes: Matrix Metalloproteinases and Their Multifaceted Roles in Neurodegenerative Diseases," *Mediators of Inflammation,* vol. 2015, pp. 1-27, 2015, doi: 10.1155/2015/620581.

[36] A. Lukes, S. Mun-Bryce, M. Lukes, and G. A. Rosenberg, "Extracellular matrix degradation by metalloproteinases and central nervous system diseases," *Molecular neurobiology,* vol. 19, no. 3, pp. 267-284, 1999.

[37] B. Cauwe and G. Opdenakker, "Intracellular substrate cleavage: a novel dimension in the biochemistry, biology and pathology of matrix metalloproteinases," *Critical reviews in biochemistry and molecular biology,* vol. 45, no. 5, pp. 351-423, 2010.

[38] S. Zucker *et al.*, "Measurement of matrix metalloproteinases and tissue inhibitors of metalloproteinases in blood and tissues: clinical and experimental applications," *Annals of the New York Academy of Sciences,* vol. 878, no. 1, pp. 212-227, 1999.

[39] D. Schuppan and E. Hahn, "MMPs in the gut: inflammation hits the matrix," *Gut,* vol. 47, no. 1, pp. 12-14, 2000.

[40] J. Dzwonek, M. Rylski, and L. Kaczmarek, "Matrix metalloproteinases and their endogenous inhibitors in neuronal physiology of the adult brain," *FEBS letters,* vol. 567, no. 1, pp. 129-135, 2004.

[41] R. G. Rempe, A. M. Hartz, and B. Bauer, "Matrix metalloproteinases in the brain and blood–brain barrier: versatile breakers and makers," *Journal of Cerebral Blood Flow & Metabolism,* vol. 36, no. 9, pp. 1481-1507, 2016.

[42] G. MURPHY *et al.*, "Mechanisms for pro matrix metalloproteinase activation," *Apmis,* vol. 107, no. 1-6, pp. 38-44, 1999.

[43] E. M. Weekman and D. M. Wilcock, "Matrix metalloproteinase in blood-brain barrier breakdown in dementia," *Journal of Alzheimer's Disease,* vol. 49, no. 4, pp. 893-903, 2016.

[44] S. Saito *et al.*, "Role of matrix metalloproteinases 1, 2, and 9 and tissue inhibitor of matrix metalloproteinase-1 in chronic venous insufficiency," (in English), *Journal of Vascular Surgery,* vol. 34, no. 5, pp. 930-937, Nov 2001. [Online]. Available: <Go to ISI>://000172305700045.

[45] M. Asahi, K. Asahi, J. C. Jung, G. J. del Zoppo, M. E. Fini, and E. H. Lo, "Role for matrix metalloproteinase 9 after focal cerebral ischemia, effects of gene knockout and enzyme inhibition with BB-94," (in English), *Journal of Cerebral Blood Flow*

and Metabolism, vol. 20, no. 12, pp. 1681-1689, Dec 2000. [Online]. Available: <Go to ISI>://000165696700007.

[46] M. Fujimura, Y. Gasche, Y. Morita-Fujimura, J. Massengale, M. Kawase, and P. H. Chan, "Early appearance of activated matrix metalloproteinase-9 and blood-brain barrier disruption in mice after focal cerebral ischemia and reperfusion," (in English), *Brain Research,* vol. 842, no. 1, pp. 92-100, Sep 18 1999. [Online]. Available: <Go to ISI>://000082809300011.

[47] R. Hanemaaijer, H. Visser, Y. T. Konttinen, P. Koolwijk, and J. H. Verheijen, "A novel and simple immunocapture assay for determination of gelatinase-B (MMP-9) activities in biological fluids: Saliva from patients with Sjogren's syndrome contain increased latent and active gelatinase-B levels," (in English), *Matrix Biology,* vol. 17, no. 8-9, pp. 657-665, Dec 1998. [Online]. Available: <Go to ISI>://000078705300011.

[48] L. Kumar, W. Colomb, J. Czerski, C. R. Cox, and S. K. Sarkar, "Efficient protease based purification of recombinant matrix metalloprotease-1 in E. coli," *Protein Expression and Purification,* vol. 148, pp. 59-67, 2018, doi: 10.1016/j.pep.2018.04.001.

[49] W. B. Saunders, "MMP-1 activation by serine proteases and MMP-10 induces human capillary tubular network collapse and regression in 3D collagen matrices," *Journal of Cell Science,* vol. 118, no. 10, pp. 2325-2340, 2005, doi: 10.1242/jcs.02360.

[50] S. W. Manka *et al.*, "Structural insights into triple-helical collagen cleavage by matrix metalloproteinase 1," *Proceedings of the National Academy of Sciences,* vol. 109, no. 31, pp. 12461-12466, 2012, doi: 10.1073/pnas.1204991109.

[51] W. S. Davidson, A. Jonas, D. F. Clayton, and J. M. George, "Stabilization of α-synuclein secondary structure upon binding to synthetic membranes," *Journal of Biological Chemistry,* vol. 273, no. 16, pp. 9443-9449, 1998.

[52] P. H. Weinreb, W. Zhen, A. W. Poon, K. A. Conway, and P. T. Lansbury, "NACP, a protein implicated in Alzheimer's disease and learning, is natively unfolded," *Biochemistry,* vol. 35, no. 43, pp. 13709-13715, 1996.

[53] F. N. Emamzadeh, "Alpha-synuclein structure, functions, and interactions," *J Res Med Sci,* vol. 21, p. 29, 2016, doi: 10.4103/1735-1995.181989.

[54] M. L. Choi and S. Gandhi, "Crucial role of protein oligomerization in the pathogenesis of Alzheimer's and Parkinson's diseases," *The FEBS Journal,* vol. 285, no. 19, pp. 3631-3644, 2018, doi: 10.1111/febs.14587.

[55] C. W. Olanow and S. B. Prusiner, "Is Parkinson's disease a prion disorder?," *Proceedings of the National Academy of Sciences,* vol. 106, no. 31, pp. 12571-12572, 2009, doi: 10.1073/pnas.0906759106.

[56] R. Barbour *et al.*, "Red blood cells are the major source of alpha-synuclein in blood," *Neurodegener Dis,* vol. 5, no. 2, pp. 55-9, 2008, doi: 10.1159/000112832.

[57] L. Maroteaux, J. Campanelli, and R. Scheller, "Synuclein: a neuron-specific protein localized to the nucleus and presynaptic nerve terminal," *The Journal of Neuroscience,* vol. 8, no. 8, pp. 2804-2815, 1988, doi: 10.1523/jneurosci.08-08-02804.1988.

[58] W. E. Hughes, Z. Elgundi, P. Huang, M. A. Frohman, and T. J. Biden, "Phospholipase D1 Regulates Secretagogue-stimulated Insulin Release in Pancreatic β-Cells," *Journal of Biological Chemistry,* vol. 279, no. 26, pp. 27534-27541, 2004, doi: 10.1074/jbc.m403012200.

[59] S. Chandra, G. Gallardo, R. Fernández-Chacón, O. M. Schlüter, and T. C. Südhof, "α-Synuclein Cooperates with CSPα in Preventing Neurodegeneration," *Cell,* vol. 123, no. 3, pp. 383-396, 2005, doi: 10.1016/j.cell.2005.09.028.

[60] A. Abeliovich *et al.*, "Mice lacking α-synuclein display functional deficits in the nigrostriatal dopamine system," *Neuron,* vol. 25, no. 1, pp. 239-252, 2000.

[61] D. E. Cabin *et al.*, "Synaptic Vesicle Depletion Correlates with Attenuated Synaptic Responses to Prolonged Repetitive Stimulation in Mice Lacking α-Synuclein," *The Journal of Neuroscience,* vol. 22, no. 20, pp. 8797-8807, 2002, doi: 10.1523/jneurosci.22-20-08797.2002.

[62] D. D. Murphy, S. M. Rueter, J. Q. Trojanowski, and V. M. Y. Lee, "Synucleins Are Developmentally Expressed, and α-Synuclein Regulates the Size of the Presynaptic Vesicular Pool in Primary Hippocampal Neurons," *The Journal of Neuroscience,* vol. 20, no. 9, pp. 3214-3220, 2000, doi: 10.1523/jneurosci.20-09-03214.2000.

[63] M. H. R. Ludtmann, P. R. Angelova, N. N. Ninkina, S. Gandhi, V. L. Buchman, and A. Y. Abramov, "Monomeric Alpha-Synuclein Exerts a Physiological Role on Brain ATP Synthase," *Journal of Neuroscience,* vol. 36, no. 41, pp. 10510-10521, 2016, doi: 10.1523/jneurosci.1659-16.2016.

[64] E. J. Coulson, K. Paliga, K. Beyreuther, and C. L. Masters, "What the evolution of the amyloid protein precursor supergene family tells us about its function," (in eng), *Neurochem Int,* vol. 36, no. 3, pp. 175-84, Mar 2000, doi: 10.1016/s0197-0186(99)00125-4.

[65] R. J. Guerreiro, D. R. Gustafson, and J. Hardy, "The genetic architecture of Alzheimer's disease: beyond APP, PSENs and APOE," (in eng), *Neurobiol*

Aging, vol. 33, no. 3, pp. 437-56, Mar 2012, doi: 10.1016/j.neurobiolaging.2010.03.025.

[66] W. E. Van Nostrand, A. J. Rozemuller, R. Chung, C. W. Cotman, and S. M. Saporito-Irwin, "Amyloid β-protein precursor in cultured leptomeningeal smooth muscle cells," *Amyloid,* vol. 1, no. 1, pp. 1-7, 1994.

[67] J. Hardy, "Amyloid, the presenilins and Alzheimer's disease," (in eng), *Trends Neurosci,* vol. 20, no. 4, pp. 154-9, Apr 1997, doi: 10.1016/s0166-2236(96)01030-2.

[68] C. Priller, T. Bauer, G. Mitteregger, B. Krebs, H. A. Kretzschmar, and J. Herms, "Synapse formation and function is modulated by the amyloid precursor protein," (in eng), *J Neurosci,* vol. 26, no. 27, pp. 7212-21, Jul 5 2006, doi: 10.1523/jneurosci.1450-06.2006.

[69] P. R. Turner, K. O'Connor, W. P. Tate, and W. C. Abraham, "Roles of amyloid precursor protein and its fragments in regulating neural activity, plasticity and memory," (in eng), *Prog Neurobiol,* vol. 70, no. 1, pp. 1-32, May 2003, doi: 10.1016/s0301-0082(03)00089-3.

[70] C. W. Xie and J. Tang, "[Enlightenment gained from the discovery of the cardiac endocrine function]," (in chi), *Sheng Li Ke Xue Jin Zhan,* vol. 17, no. 1, pp. 6-8, Jan 1986.

[71] G.-F. Chen *et al.*, "Amyloid beta: structure, biology and structure-based therapeutic development," *Acta Pharmacologica Sinica,* vol. 38, no. 9, pp. 1205-1235, 2017, doi: 10.1038/aps.2017.28.

[72] N. Iwata *et al.*, "Identification of the major Abeta1-42-degrading catabolic pathway in brain parenchyma: suppression leads to biochemical and pathological deposition," *Nat Med,* vol. 6, no. 2, pp. 143-50, Feb 2000, doi: 10.1038/72237.

[73] S.-S. Yoon and S.-M. Ahnjo, "Mechanisms of Amyloid-β Peptide Clearance: Potential Therapeutic Targets for Alzheimer's Disease," *Biomolecules and Therapeutics,* vol. 20, no. 3, pp. 245-255, 2012, doi: 10.4062/biomolther.2012.20.3.245.

[74] N. G. Sgourakis, Y. Yan, S. A. McCallum, C. Wang, and A. E. Garcia, "The Alzheimer's peptides Abeta40 and 42 adopt distinct conformations in water: a combined MD / NMR study," (in eng), *J Mol Biol,* vol. 368, no. 5, pp. 1448-57, May 18 2007, doi: 10.1016/j.jmb.2007.02.093.

[75] A. F. Hill *et al.*, "Molecular classification of sporadic Creutzfeldt–Jakob disease," *Brain,* vol. 126, no. 6, pp. 1333-1346, 2003, doi: 10.1093/brain/awg125.

[76] L. Cracco *et al.*, "Gerstmann-Sträussler-Scheinker disease revisited: accumulation of covalently-linked multimers of internal prion protein fragments," *Acta Neuropathologica Communications,* vol. 7, no. 1, 2019, doi: 10.1186/s40478-019-0734-2.

[77] M. G. Spillantini, M. L. Schmidt, V. M. Y. Lee, J. Q. Trojanowski, R. Jakes, and M. Goedert, "α-Synuclein in Lewy bodies," *Nature,* vol. 388, no. 6645, pp. 839-840, 1997, doi: 10.1038/42166.

[78] L. Kumar *et al.*, "Allosteric Communications between Domains Modulate the Activity of Matrix Metalloprotease-1," *Biophysical Journal,* 2020/06/17/ 2020, doi: https://doi.org/10.1016/j.bpj.2020.06.010.

[79] F. M. LaFerla, K. N. Green, and S. Oddo, "Intracellular amyloid-β in Alzheimer's disease," *Nature Reviews Neuroscience,* vol. 8, no. 7, pp. 499-509, 2007.

[80] B. Levine and D. J. Klionsky, "Development by self-digestion: molecular mechanisms and biological functions of autophagy," *Developmental cell,* vol. 6, no. 4, pp. 463-477, 2004.

[81] A.-C. Hoffmann *et al.*, "Extracellular aggregated alpha synuclein primarily triggers lysosomal dysfunction in neural cells prevented by trehalose," *Scientific reports,* vol. 9, no. 1, p. 544, 2019..

[82] D. Sevlever, P. Jiang, and S.-H. C. Yen, "Cathepsin D is the main lysosomal enzyme involved in the degradation of α-synuclein and generation of its carboxy-terminally truncated species," *Biochemistry,* vol. 47, no. 36, pp. 9678-9687, 2008.

[83] R. P. McGlinchey and J. C. Lee, "Cysteine cathepsins are essential in lysosomal degradation of α-synuclein," *Proceedings of the National Academy of Sciences,* vol. 112, no. 30, pp. 9322-9327, 2015.

[84] Y. Wang, W. Luo, and G. Reiser, "Trypsin and trypsin-like proteases in the brain: proteolysis and cellular functions," *Cellular and Molecular Life Sciences,* vol. 65, no. 2, pp. 237-252, 2008.

[85] B. M. Dufty *et al.*, "Calpain-cleavage of α-synuclein: connecting proteolytic processing to disease-linked aggregation," *The American journal of pathology,* vol. 170, no. 5, pp. 1725-1738, 2007.

[86] A. J. Mishizen-Eberz *et al.*, "Distinct cleavage patterns of normal and pathologic forms of α-synuclein by calpain I in vitro," *Journal of neurochemistry,* vol. 86, no. 4, pp. 836-847, 2003.

[87] A. Iwata *et al.*, "Alpha-synuclein degradation by serine protease neurosin: implication for pathogenesis of synucleinopathies," *Human molecular genetics,* vol. 12, no. 20, pp. 2625-2635, 2003.

[88] T. Kasai *et al.*, "Cleavage of normal and pathological forms of α-synuclein by neurosin in vitro," *Neuroscience letters,* vol. 436, no. 1, pp. 52-56, 2008.

[89] H. Tatebe *et al.*, "Extracellular neurosin degrades α-synuclein in cultured cells," *Neuroscience research,* vol. 67, no. 4, pp. 341-346, 2010.

[90] Z. Zhang *et al.*, "Asparagine endopeptidase cleaves α-synuclein and mediates pathologic activities in Parkinson's disease," *Nature structural & molecular biology,* vol. 24, no. 8, p. 632, 2017.

[91] D.-H. Choi, Y.-J. Kim, Y.-G. Kim, T. H. Joh, M. F. Beal, and Y.-S. Kim, "Role of matrix metalloproteinase 3-mediated α-synuclein cleavage in dopaminergic cell death," *Journal of Biological Chemistry,* vol. 286, no. 16, pp. 14168-14177, 2011.

[92] L. Stefanis, E. Emmanouilidou, M. Pantazopoulou, D. Kirik, K. Vekrellis, and G. K. Tofaris, "How is alpha-synuclein cleared from the cell?," *Journal of neurochemistry,* vol. 150, no. 5, pp. 577-590, 2019.

[93] S.-J. Lee, "Origins and effects of extracellular α-synuclein: implications in Parkinson's disease," *Journal of Molecular Neuroscience,* vol. 34, no. 1, pp. 17-22, 2008.

[94] R. Borghi *et al.*, "Full length α-synuclein is present in cerebrospinal fluid from Parkinson's disease and normal subjects," *Neuroscience letters,* vol. 287, no. 1, pp. 65-67, 2000.

[95] O. M. El-Agnaf *et al.*, "α-Synuclein implicated in Parkinson's disease is present in extracellular biological fluids, including human plasma," *The FASEB Journal,* vol. 17, no. 13, pp. 1-16, 2003.

[96] O. M. El-Agnaf *et al.*, "Detection of oligomeric forms of α-synuclein protein in human plasma as a potential biomarker for Parkinson's disease," *The FASEB journal,* vol. 20, no. 3, pp. 419-425, 2006.

[97] H.-J. Lee, S. Patel, and S.-J. Lee, "Intravesicular localization and exocytosis of α-synuclein and its aggregates," *Journal of Neuroscience,* vol. 25, no. 25, pp. 6016-6024, 2005.

[98] F. M. LaFerla, K. N. Green, and S. Oddo, "Intracellular amyloid-β in Alzheimer's disease," *Nature Reviews Neuroscience,* vol. 8, no. 7, pp. 499-509, 2007.

[99] T. Koshiba *et al.*, "Detection of matrix metalloproteinase activity in human pancreatic cancer," (in English), *Surgery Today-the Japanese Journal of Surgery,*

vol. 27, no. 4, pp. 302-304, 1997. [Online]. Available: <Go to ISI>://A1997WP47100003.

[100] N. Sakalihasan, P. Delvenne, B. V. Nusgens, R. Limet, and C. M. Lapiere, "Activated forms of MMP(2) and MMP(9) in abdominal aortic aneurysms," (in English), *Journal of Vascular Surgery,* vol. 24, no. 1, pp. 127-133, Jul 1996. [Online]. Available: <Go to ISI>://A1996VA17000016.

[101] H. Braak, K. Del Tredici, U. Rüb, R. A. De Vos, E. N. J. Steur, and E. Braak, "Staging of brain pathology related to sporadic Parkinson's disease," *Neurobiology of aging,* vol. 24, no. 2, pp. 197-211, 2003.

[102] S. Holmqvist *et al.*, "Direct evidence of Parkinson pathology spread from the gastrointestinal tract to the brain in rats," *Acta neuropathologica,* vol. 128, no. 6, pp. 805-820, 2014.

[103] A.-C. Hoffmann *et al.*, "Extracellular aggregated alpha synuclein primarily triggers lysosomal dysfunction in neural cells prevented by trehalose," *Scientific reports,* vol. 9, no. 1, p. 544, 2019.

[104] T. Harach *et al.*, "Reduction of Abeta amyloid pathology in APPPS1 transgenic mice in the absence of gut microbiota," *Scientific reports,* vol. 7, p. 41802, 2017.

[105] B. I. Ratnikov *et al.*, "Basis for substrate recognition and distinction by matrix metalloproteinases," *Proceedings of the National Academy of Sciences,* vol. 111, no. 40, pp. E4148-E4155, 2014, doi: 10.1073/pnas.1406134111.

[106] K. I. Shimokawa, "Matrix metalloproteinase (MMP)-2 and MMP-9 activities in human seminal plasma," *Molecular Human Reproduction,* vol. 8, no. 1, pp. 32-36, 2002, doi: 10.1093/molehr/8.1.32.

[107] M. G. Spillantini, M. L. Schmidt, V. M.-Y. Lee, J. Q. Trojanowski, R. Jakes, and M. Goedert, "α-Synuclein in Lewy bodies," *Nature,* vol. 388, no. 6645, p. 839, 1997.

[108] J. M. George, H. Jin, W. S. Woods, and D. F. Clayton, "Characterization of a novel protein regulated during the critical period for song learning in the zebra finch," *Neuron,* vol. 15, no. 2, pp. 361-372, 1995.

[109] U. Dettmer, A. J. Newman, E. S. Luth, T. Bartels, and D. Selkoe, "In vivo cross-linking reveals principally oligomeric forms of α-synuclein and β-synuclein in neurons and non-neural cells," *Journal of Biological Chemistry,* vol. 288, no. 9, pp. 6371-6385, 2013.

[110] P. J. Kahle *et al.*, "Subcellular localization of wild-type and Parkinson's disease-associated mutant α-synuclein in human and transgenic mouse brain," *Journal of Neuroscience,* vol. 20, no. 17, pp. 6365-6373, 2000.

[111] A. Iwai *et al.*, "The precursor protein of non-Aβ component of Alzheimer's disease amyloid is a presynaptic protein of the central nervous system," *Neuron,* vol. 14, no. 2, pp. 467-475, 1995.

[112] R. Jakes, M. G. Spillantini, and M. Goedert, "Identification of two distinct synucleins from human brain," *FEBS letters,* vol. 345, no. 1, pp. 27-32, 1994.

[113] G. S. Withers, J. M. George, G. A. Banker, and D. F. Clayton, "Delayed localization of synelfin (synuclein, NACP) to presynaptic terminals in cultured rat hippocampal neurons," *Developmental brain research,* vol. 99, no. 1, pp. 87-94, 1997.

[114] S.-J. Lee, H. Jeon, and K. V. Kandror, "Alpha-synuclein is localized in a subpopulation of rat brain synaptic vesicles," *Acta Neurobiol Exp (Wars),* vol. 68, no. 4, pp. 509-515, 2008.

[115] L. Zhang *et al.*, "Semi-quantitative analysis of α-synuclein in subcellular pools of rat brain neurons: an immunogold electron microscopic study using a C-terminal specific monoclonal antibody," *Brain research,* vol. 1244, pp. 40-52, 2008.

[116] K. E. Larsen *et al.*, "α-Synuclein overexpression in PC12 and chromaffin cells impairs catecholamine release by interfering with a late step in exocytosis," *Journal of Neuroscience,* vol. 26, no. 46, pp. 11915-11922, 2006.

[117] V. M. Nemani *et al.*, "Increased expression of α-synuclein reduces neurotransmitter release by inhibiting synaptic vesicle reclustering after endocytosis," *Neuron,* vol. 65, no. 1, pp. 66-79, 2010.

[118] L. Yavich, H. Tanila, S. Vepsäläinen, and P. Jäkälä, "Role of α-synuclein in presynaptic dopamine recruitment," *Journal of Neuroscience,* vol. 24, no. 49, pp. 11165-11170, 2004.

[119] L. Yavich, P. Jäkälä, and H. Tanila, "Abnormal compartmentalization of norepinephrine in mouse dentate gyrus in α-synuclein knockout and A30P transgenic mice," *Journal of neurochemistry,* vol. 99, no. 3, pp. 724-732, 2006.

[120] F. Cheng, G. Vivacqua, and S. Yu, "The role of alpha-synuclein in neurotransmission and synaptic plasticity," *Journal of chemical neuroanatomy,* vol. 42, no. 4, pp. 242-248, 2011.

[121] K. A. Conway, J. D. Harper, and P. T. Lansbury, "Accelerated in vitro fibril formation by a mutant α-synuclein linked to early-onset Parkinson disease," *Nature medicine,* vol. 4, no. 11, p. 1318, 1998.

[122] I. F. Tsigelny *et al.*, "Mechanisms of hybrid oligomer formation in the pathogenesis of combined Alzheimer's and Parkinson's diseases," *PloS one,* vol. 3, no. 9, p. e3135, 2008.

[123] A. Oueslati, M. Fournier, and H. A. Lashuel, "Role of post-translational modifications in modulating the structure, function and toxicity of α-synuclein: implications for Parkinson's disease pathogenesis and therapies," in *Progress in brain research*, vol. 183: Elsevier, 2010, pp. 115-145.

[124] G. Taschenberger, M. Garrido, Y. Tereshchenko, M. Bähr, M. Zweckstetter, and S. Kügler, "Aggregation of αSynuclein promotes progressive in vivo neurotoxicity in adult rat dopaminergic neurons," *Acta neuropathologica,* vol. 123, no. 5, pp. 671-683, 2012.

[125] M. M. Dedmon, K. Lindorff-Larsen, J. Christodoulou, M. Vendruscolo, and C. M. Dobson, "Mapping long-range interactions in α-synuclein using spin-label NMR and ensemble molecular dynamics simulations," *Journal of the American Chemical Society,* vol. 127, no. 2, pp. 476-477, 2005.

[126] V. N. Uversky *et al.*, "Biophysical properties of the synucleins and their propensities to fibrillate inhibition of α-synuclein assembly by β-and γ-synucleins," *Journal of Biological Chemistry,* vol. 277, no. 14, pp. 11970-11978, 2002.

[127] C. M. Pfefferkorn, Z. Jiang, and J. C. Lee, "Biophysics of α-synuclein membrane interactions," *Biochimica et Biophysica Acta (BBA)-Biomembranes,* vol. 1818, no. 2, pp. 162-171, 2012.

[128] H. A. Lashuel, C. R. Overk, A. Oueslati, and E. Masliah, "The many faces of α-synuclein: from structure and toxicity to therapeutic target," *Nature Reviews Neuroscience,* vol. 14, no. 1, p. 38, 2013.

[129] B. I. Giasson, K. Uryu, J. Q. Trojanowski, and V. M.-Y. Lee, "Mutant and wild type human α-synucleins assemble into elongated filaments with distinct morphologies in vitro," *Journal of Biological Chemistry,* vol. 274, no. 12, pp. 7619-7622, 1999.

[130] L. Narhi *et al.*, "Both familial Parkinson's disease mutations accelerate α-synuclein aggregation," *Journal of Biological Chemistry,* vol. 274, no. 14, pp. 9843-9846, 1999.

[131] A. L. Biere *et al.*, "Parkinson's disease-associated α-synuclein is more fibrillogenic than β-and γ-synuclein and cannot cross-seed its homologs," *Journal of Biological Chemistry,* vol. 275, no. 44, pp. 34574-34579, 2000.

[132] A. E. Powers and D. S. Patel, "Expression and Purification of Untagged α-Synuclein," in *Alpha-Synuclein*: Springer, 2019, pp. 261-269.

[133] J. Y. Choi *et al.*, "Rapid purification and analysis of α-synuclein proteins: C-terminal truncation promotes the conversion of α-synuclein into a protease-sensitive form in Escherichia coli," *Biotechnology and applied biochemistry,* vol. 36, no. 1, pp. 33-40, 2002.

[134] V. N. Uversky, J. Li, and A. L. Fink, "Evidence for a partially folded intermediate in α-synuclein fibril formation," *Journal of Biological Chemistry,* vol. 276, no. 14, pp. 10737-10744, 2001.

[135] C. Huang, G. Ren, H. Zhou, and C.-c. Wang, "A new method for purification of recombinant human α-synuclein in Escherichia coli," *Protein expression and purification,* vol. 42, no. 1, pp. 173-177, 2005.

[136] K. D. Kloepper, W. S. Woods, K. A. Winter, J. M. George, and C. M. Rienstra, "Preparation of α-synuclein fibrils for solid-state NMR: expression, purification, and incubation of wild-type and mutant forms," *Protein expression and purification,* vol. 48, no. 1, pp. 112-117, 2006.

[137] L. Caldinelli, D. Albani, and L. Pollegioni, "One single method to produce native and Tat-fused recombinant human α-synuclein in Escherichia coli," *BMC biotechnology,* vol. 13, no. 1, p. 32, 2013.

[138] H. R. Gerding *et al.*, "Reductive modification of genetically encoded 3-nitrotyrosine sites in alpha synuclein expressed in E. coli," *Redox biology,* vol. 26, p. 101251, 2019.

[139] E. S. Luth, T. Bartels, U. Dettmer, N. C. Kim, and D. J. Selkoe, "Purification of α-synuclein from human brain reveals an instability of endogenous multimers as the protein approaches purity," *Biochemistry,* vol. 54, no. 2, pp. 279-292, 2014.

[140] T. Bartels, J. G. Choi, and D. J. Selkoe, "α-Synuclein occurs physiologically as a helically folded tetramer that resists aggregation," *Nature,* vol. 477, no. 7362, p. 107, 2011.

[141] M. Karampetsou *et al.*, "Phosphorylated exogenous alpha-synuclein fibrils exacerbate pathology and induce neuronal dysfunction in mice," *Scientific reports,* vol. 7, no. 1, p. 16533, 2017.

[142] E. I. Yakupova, L. G. Bobyleva, I. M. Vikhlyantsev, and A. G. Bobylev, "Congo Red and amyloids: history and relationship," *Bioscience reports,* vol. 39, no. 1, 2019.

[143] P. Frid, S. V. Anisimov, and N. Popovic, "Congo red and protein aggregation in neurodegenerative diseases," *Brain Research Reviews,* vol. 53, no. 1, pp. 135-160, 2007.

[144] C. E.-H. Moussa, C. Wersinger, M. Rusnak, Y. Tomita, and A. Sidhu, "Abnormal migration of human wild-type α-synuclein upon gel electrophoresis," *Neuroscience letters,* vol. 371, no. 2-3, pp. 239-243, 2004.

[145] K. Weber, J. Pringle, and M. Osborn, "Measurement of molecular weights by electrophoresis on SDS-acrylamide gel," in *Methods in enzymology*, vol. 26: Elsevier, 1972, pp. 3-27.

[146] A. Grote *et al.*, "JCat: a novel tool to adapt codon usage of a target gene to its potential expression host," (in eng), *Nucleic Acids Res,* vol. 33, no. Web Server issue, pp. W526-31, Jul 1 2005, doi: 10.1093/nar/gki376.

[147] P. Edman, E. Högfeldt, and L. G. Sillén, "Method for determination of the amino acid sequence in peptides," *Acta chem. scand,* vol. 4, no. 7, pp. 283-293, 1950.

[148] P. Edman and G. Begg, "A protein sequenator," in *European Journal of Biochemistry*: Springer, 1967, pp. 80-91.

[149] P. Edman, "Sequence determination," in *Protein sequence determination*: Springer, 1970, pp. 211-255.

[150] M. Xilouri, O. R. Brekk, and L. Stefanis, "Alpha-synuclein and protein degradation systems: a reciprocal relationship," *Molecular neurobiology,* vol. 47, no. 2, pp. 537-551, 2013.

[151] I. Horvath *et al.*, "Mechanisms of protein oligomerization: inhibitor of functional amyloids templates α-synuclein fibrillation," *Journal of the American Chemical Society,* vol. 134, no. 7, pp. 3439-3444, 2012.

[152] D. J. Selkoe, "Cell biology of protein misfolding: the examples of Alzheimer's and Parkinson's diseases," *Nature cell biology,* vol. 6, no. 11, p. 1054, 2004.

[153] G. Forloni *et al.*, "Protein misfolding in Alzheimer’s and Parkinson’s disease: genetics and molecular mechanisms," *Neurobiology of aging,* vol. 23, no. 5, pp. 957-976, 2002.

[154] P. T. Lansbury and H. A. Lashuel, "A century-old debate on protein aggregation and neurodegeneration enters the clinic," *Nature,* vol. 443, no. 7113, pp. 774-779, 2006.

[155] R. Greenwald, L. Golub, N. Ramamurthy, M. Chowdhury, S. Moak, and T. Sorsa, "In vitro sensitivity of the three mammalian collagenases to tetracycline inhibition: relationship to bone and cartilage degradation," *Bone,* vol. 22, no. 1, pp. 33-38, 1998.

[156] T. J. Federici, "The non-antibiotic properties of tetracyclines: clinical potential in ophthalmic disease," *Pharmacological research,* vol. 64, no. 6, pp. 614-623, 2011.

[157] E. Nuti, T. Tuccinardi, and A. Rossello, "Matrix metalloproteinase inhibitors: new challenges in the era of post broad-spectrum inhibitors," *Current pharmaceutical design,* vol. 13, no. 20, pp. 2087-2100, 2007.

[158] V. Mohan, D. Talmi-Frank, V. Arkadash, N. Papo, and I. Sagi, "Matrix metalloproteinase protein inhibitors: highlighting a new beginning for metalloproteinases in medicine," *Metalloproteinases in medicine,* vol. 3, pp. 31-47, 2016.

[159] B. Sloan and N. Scheinfeld, "The use and safety of doxycycline hyclate and other second-generation tetracyclines," *Expert opinion on drug safety,* vol. 7, no. 5, pp. 571-577, 2008.

[160] U. Eckhard *et al.*, "Active site specificity profiling of the matrix metalloproteinase family: Proteomic identification of 4300 cleavage sites by nine MMPs explored with structural and synthetic peptide cleavage analyses," *Matrix Biology,* vol. 49, pp. 37-60, 2016.

[161] B. I. Ratnikov *et al.*, "Basis for substrate recognition and distinction by matrix metalloproteinases," *Proceedings of the National Academy of Sciences,* vol. 111, no. 40, pp. E4148-E4155, 2014.

[162] C. M. Overall, "Molecular determinants of metalloproteinase substrate specificity," *Molecular biotechnology,* vol. 22, no. 1, pp. 51-86, 2002.

[163] L. Kumar *et al.*, "Allosteric Communications between Domains Modulate the Activity of Matrix Metalloprotease-1," *Biophysical Journal,* vol. 119, no. 2, pp. 360-374, 2020, doi: 10.1016/j.bpj.2020.06.010.

[164] L. Kumar *et al.*, "Activity-dependent interdomain dynamics of matrix metalloprotease-1 on fibrin," *Scientific reports,* vol. 10, no. 1, pp. 1-14, 2020.

[165] G. Wertheim, M. Butler, K. West, and D. Buchanan, "Determination of the Gaussian and Lorentzian content of experimental line shapes," *Review of Scientific Instruments,* vol. 45, no. 11, pp. 1369-1371, 1974.

[166] D. Kozakov *et al.*, "The ClusPro web server for protein–protein docking," *Nature protocols,* vol. 12, no. 2, p. 255, 2017.

[167] S. R. Comeau, D. W. Gatchell, S. Vajda, and C. J. Camacho, "ClusPro: a fully automated algorithm for protein–protein docking," *Nucleic acids research,* vol. 32, no. suppl_2, pp. W96-W99, 2004.

[168] N. Yanamala, K. C. Tirupula, and J. Klein-Seetharaman, "Preferential binding of allosteric modulators to active and inactive conformational states of metabotropic glutamate receptors," in *BMC bioinformatics*, 2008, vol. 9, no. 1: BioMed Central, p. S16.

[169] N. M. Goodey and S. J. Benkovic, "Allosteric regulation and catalysis emerge via a common route," *Nature chemical biology,* vol. 4, no. 8, p. 474, 2008.

[170] G. G. Hammes, "Multiple conformational changes in enzyme catalysis," *Biochemistry,* vol. 41, no. 26, pp. 8221-8228, 2002.

[171] D. Kern and E. R. Zuiderweg, "The role of dynamics in allosteric regulation," *Current opinion in structural biology,* vol. 13, no. 6, pp. 748-757, 2003.

[172] R. D. Vale and R. A. Milligan, "The way things move: looking under the hood of molecular motor proteins," *Science,* vol. 288, no. 5463, pp. 88-95, 2000.

[173] M. Schliwa and G. Woehlke, "Molecular motors," *Nature,* vol. 422, no. 6933, pp. 759-765, 2003.

[174] S. Hammes-Schiffer and S. J. Benkovic, "Relating protein motion to catalysis," *Annu. Rev. Biochem.,* vol. 75, pp. 519-541, 2006.

[175] P. Csermely, R. Palotai, and R. Nussinov, "Induced fit, conformational selection and independent dynamic segments: an extended view of binding events," *Trends in biochemical sciences,* vol. 35, no. 10, pp. 539-546, 2010.

[176] Y. Sugita and Y. Okamoto, "Replica-exchange molecular dynamics method for protein folding," *Chemical physics letters,* vol. 314, no. 1-2, pp. 141-151, 1999.

[177] V. A. Jarymowycz and M. J. Stone, "Fast time scale dynamics of protein backbones: NMR relaxation methods, applications, and functional consequences," *Chemical reviews,* vol. 106, no. 5, pp. 1624-1671, 2006.

[178] T. Schreiber, "Measuring information transfer," *Physical review letters,* vol. 85, no. 2, p. 461, 2000.

[179] H. Kamberaj and A. van der Vaart, "Extracting the causality of correlated motions from molecular dynamics simulations," *Biophysical journal,* vol. 97, no. 6, pp. 1747-1755, 2009.

[180] V. M. Burger, D. J. Arenas, and C. M. Stultz, "A structure-free method for quantifying conformational flexibility in proteins," *Scientific reports,* vol. 6, p. 29040, 2016.

[181] T. Lenaerts, J. Ferkinghoff-Borg, F. Stricher, L. Serrano, J. W. Schymkowitz, and F. Rousseau, "Quantifying information transfer by protein domains: analysis of the Fyn SH2 domain structure," *BMC structural biology,* vol. 8, no. 1, p. 43, 2008.

[182] Z. Wang *et al.*, "Combined strategies in structure-based virtual screening," *Physical Chemistry Chemical Physics,* vol. 22, no. 6, pp. 3149-3159, 2020.

[183] S. Kamboj *et al.*, "A method of purifying alpha-synuclein in E. coli without chromatography," *Heliyon,* vol. 7, no. 1, p. e05874, 2021/01/01/ 2021, doi: https://doi.org/10.1016/j.heliyon.2020.e05874.

[184] X. Zhuang *et al.*, "A single-molecule study of RNA catalysis and folding," *Science,* vol. 288, no. 5473, pp. 2048-2051, 2000.

[185] J. Czerski, W. Colomb, F. Cannataro, and S. Sarkar, "Spectroscopic identification of individual fluorophores using photoluminescence excitation spectra," *Journal of microscopy,* vol. 270, no. 3, pp. 261-271, 2018.

[186] W. Colomb, J. Czerski, J. Sau, and S. Sarkar, "Estimation of microscope drift using fluorescent nanodiamonds as fiducial markers," *Journal of microscopy,* vol. 266, no. 3, pp. 298-306, 2017.

[187] A. Dittmore, J. Silver, S. K. Sarkar, B. Marmer, G. I. Goldberg, and K. C. Neuman, "Internal strain drives spontaneous periodic buckling in collagen and regulates remodeling," *Proceedings of the National Academy of Sciences,* p. 201523228, 2016.

[188] S. K. Sarkar, B. Marmer, G. Goldberg, and K. C. Neuman, "Single-molecule tracking of collagenase on native type I collagen fibrils reveals degradation mechanism," *Current biology : CB,* vol. 22, no. 12, pp. 1047-56, Jun 19 2012, doi: 10.1016/j.cub.2012.04.012.

[189] B. C. Arnold, "Pareto distribution," *Wiley StatsRef: Statistics Reference Online,* pp. 1-10, 2014.

[190] R. M. Haralick, K. Shanmugam, and I. H. Dinstein, "Textural features for image classification," *IEEE Transactions on systems, man, and cybernetics,* no. 6, pp. 610-621, 1973.

[191] C. E. Shannon, "A mathematical theory of communication," *The Bell system technical journal,* vol. 27, no. 3, pp. 379-423, 1948.

[192] C. Haass and D. J. Selkoe, "Soluble protein oligomers in neurodegeneration: lessons from the Alzheimer's amyloid β-peptide," *Nature reviews Molecular cell biology,* vol. 8, no. 2, pp. 101-112, 2007.

[193] B. De Strooper, "Proteases and proteolysis in Alzheimer disease: a multifactorial view on the disease process," *Physiological reviews,* vol. 90, no. 2, pp. 465-494, 2010.

[194] J. Ghiso and B. Frangione, "Amyloidosis and Alzheimer's disease," *Advanced drug delivery reviews,* vol. 54, no. 12, pp. 1539-1551, 2002.

[195] M. Chen, "The maze of APP processing in Alzheimer's disease: where did we go wrong in reasoning?," *Frontiers in Cellular Neuroscience,* vol. 9, p. 186, 2015.

[196] N. E. Pryor, M. A. Moss, and C. N. Hestekin, "Unraveling the early events of amyloid-β protein (Aβ) aggregation: techniques for the determination of Aβ aggregate size," *International Journal of Molecular Sciences,* vol. 13, no. 3, pp. 3038-3072, 2012.

[197] I. W. Hamley, "The amyloid beta peptide: a chemist's perspective. Role in Alzheimer's and fibrillization," *Chemical reviews,* vol. 112, no. 10, pp. 5147-5192, 2012.

[198] C. Tallant, A. Marrero, and F. X. Gomis-Rüth, "Matrix metalloproteinases: fold and function of their catalytic domains," *Biochimica et Biophysica Acta (BBA)-Molecular Cell Research,* vol. 1803, no. 1, pp. 20-28, 2010.

[199] X.-X. Wang, M.-S. Tan, J.-T. Yu, and L. Tan, "Matrix metalloproteinases and their multiple roles in Alzheimer's disease," *BioMed research international,* vol. 2014, 2014.

[200] B. Mroczko, M. Groblewska, and M. Barcikowska, "The role of matrix metalloproteinases and tissue inhibitors of metalloproteinases in the pathophysiology of neurodegeneration: a literature study," *Journal of Alzheimer's Disease,* vol. 37, no. 2, pp. 273-283, 2013.

[201] S. Lorenzl, K. Buerger, H. Hampel, and M. F. Beal, "Profiles of matrix metalloproteinases and their inhibitors in plasma of patients with dementia," *International psychogeriatrics,* vol. 20, no. 1, p. 67, 2008.

[202] J. R. Backstrom, G. P. Lim, M. J. Cullen, and Z. A. Tökés, "Matrix metalloproteinase-9 (MMP-9) is synthesized in neurons of the human hippocampus and is capable of degrading the amyloid-β peptide (1–40)," *Journal of Neuroscience,* vol. 16, no. 24, pp. 7910-7919, 1996.

[203] Z. Li *et al.*, "Essential roles of enteric neuronal serotonin in gastrointestinal motility and the development/survival of enteric dopaminergic neurons," *Journal of Neuroscience,* vol. 31, no. 24, pp. 8998-9009, 2011.

[204] K. N. Porter, S. N. Sarkar, D. A. Dakhlallah, M. E. Vannoy, D. D. Quintana, and J. W. Simpkins, "Medroxyprogesterone Acetate Impairs Amyloid Beta Degradation in a Matrix Metalloproteinase-9 Dependent Manner," *Frontiers in aging neuroscience,* vol. 12, p. 92, 2020.

[205] H. Braak, K. Del Tredici, U. Rub, R. A. de Vos, E. N. Jansen Steur, and E. Braak, "Staging of brain pathology related to sporadic Parkinson's disease," *Neurobiol Aging,* vol. 24, no. 2, pp. 197-211, Mar-Apr 2003, doi: 10.1016/s0197-4580(02)00065-9.

[206] L. Gu and Z. Guo, "Alzheimer's Aβ42 and Aβ40 peptides form interlaced amyloid fibrils," *Journal of Neurochemistry,* vol. 126, no. 3, pp. 305-311, 2013, doi: 10.1111/jnc.12202.

[207] N. Cui, M. Hu, and R. A. Khalil, "Biochemical and Biological Attributes of Matrix Metalloproteinases," Elsevier, 2017, pp. 1-73.

[208] K. Abbayya, N. Y. Puthanakar, S. Naduwinmani, and Y. S. Chidambar, "Association between Periodontitis and Alzheimer's Disease," *N Am J Med Sci,* vol. 7, no. 6, pp. 241-6, Jun 2015, doi: 10.4103/1947-2714.159325.

[209] J. Chang, A. Stanfill, and T. Pourmotabbed, "The Role of Matrix Metalloproteinase Polymorphisms in Ischemic Stroke," *International Journal of Molecular Sciences,* vol. 17, no. 8, p. 1323, 2016, doi: 10.3390/ijms17081323.

[210] G. Hu, P. Jousilahti, S. Bidel, R. Antikainen, and J. Tuomilehto, "Type 2 Diabetes and the Risk of Parkinson's Disease," *Diabetes Care,* vol. 30, no. 4, pp. 842-847, 2007, doi: 10.2337/dc06-2011.

[211] Y.-P. Huang *et al.*, "Parkinson’s Disease Is Related to an Increased Risk of Ischemic Stroke—A Population-Based Propensity Score-Matched Follow-Up Study," *PLoS ONE,* vol. 8, no. 9, p. e68314, 2013, doi: 10.1371/journal.pone.0068314.

[212] P. Liu, M. Sun, and S. Sader, "Matrix metalloproteinases in cardiovascular disease," *Canadian Journal of Cardiology,* vol. 22, pp. 25B-30B, 2006, doi: 10.1016/s0828-282x(06)70983-7.

[213] J.-H. Park *et al.*, "Association of Parkinson Disease With Risk of Cardiovascular Disease and All-Cause Mortality," *Circulation,* vol. 141, no. 14, pp. 1205-1207, 2020, doi: 10.1161/circulationaha.119.044948.

[214] S. A. Peeters *et al.*, "Plasma matrix metalloproteinases are associated with incident cardiovascular disease and all-cause mortality in patients with type 1 diabetes: a 12-year follow-up study," *Cardiovascular Diabetology,* vol. 16, no. 1, 2017, doi: 10.1186/s12933-017-0539-1.

[215] F. B. Teixeira *et al.*, "Periodontitis and Alzheimer's Disease: A Possible Comorbidity between Oral Chronic Inflammatory Condition and Neuroinflammation," *Frontiers in Aging Neuroscience,* vol. 9, 2017, doi: 10.3389/fnagi.2017.00327.

[216] R. Sender, S. Fuchs, and R. Milo, "Revised Estimates for the Number of Human and Bacteria Cells in the Body," *PLOS Biology,* vol. 14, no. 8, p. e1002533, 2016, doi: 10.1371/journal.pbio.1002533.

[217] N. Steck *et al.*, "Enterococcus faecalis Metalloprotease Compromises Epithelial Barrier and Contributes to Intestinal Inflammation," *Gastroenterology,* vol. 141, no. 3, pp. 959-971, 2011, doi: 10.1053/j.gastro.2011.05.035.

[218] T. R. Lin, W. Zhang, and M. W. Mulholland, "Cytokine stimulation of matrix metalloproteinase secretion in myenteric glia," *Journal of Surgical Research,* vol. 114, no. 2, p. 267, 2003, doi: 10.1016/j.jss.2003.08.215.

[219] Y.-B. Yu, "Enteric glial cells and their role in the intestinal epithelial barrier," *World Journal of Gastroenterology,* vol. 20, no. 32, p. 11273, 2014, doi: 10.3748/wjg.v20.i32.11273.

[220] D. W. Dickson, "Parkinson's Disease and Parkinsonism: Neuropathology," *Cold Spring Harbor Perspectives in Medicine,* vol. 2, no. 8, pp. a009258-a009258, 2012, doi: 10.1101/cshperspect.a009258.

[221] A. E. Lang, "The progression of Parkinson disease: a hypothesis," *Neurology,* vol. 68, no. 12, pp. 948-52, Mar 20 2007, doi: 10.1212/01.wnl.0000257110.91041.5d.

[222] J. Ma, J. Gao, J. Wang, and A. Xie, "Prion-Like Mechanisms in Parkinson's Disease," *Frontiers in Neuroscience,* vol. 13, 2019, doi: 10.3389/fnins.2019.00552.

[223] L. C. Walker, "Prion-like mechanisms in Alzheimer disease," Elsevier, 2018, pp. 303-319.

[224] D. G. Hernandez, X. Reed, and A. B. Singleton, "Genetics in Parkinson disease: Mendelian versus non-Mendelian inheritance," *Journal of Neurochemistry,* vol. 139, pp. 59-74, 2016, doi: 10.1111/jnc.13593.

[225] C. Klein and A. Westenberger, "Genetics of Parkinson's Disease," *Cold Spring Harbor Perspectives in Medicine,* vol. 2, no. 1, pp. a008888-a008888, 2012, doi: 10.1101/cshperspect.a008888.

[226] A. B. Singleton, M. J. Farrer, and V. Bonifati, "The genetics of Parkinson's disease: Progress and therapeutic implications," *Movement Disorders,* vol. 28, no. 1, pp. 14-23, 2013, doi: 10.1002/mds.25249.

[227] "Genetics and Parkinson's." Parkinson's Foundation. https://www.parkinson.org/understanding-parkinsons/causes/genetics (accessed 2021).

[228] C. Jiang, G. Li, P. Huang, Z. Liu, and B. Zhao, "The Gut Microbiota and Alzheimer's Disease," *J Alzheimers Dis,* vol. 58, no. 1, pp. 1-15, 2017, doi: 10.3233/JAD-161141.

[229] Z. D. Wallen *et al.*, "Characterizing dysbiosis of gut microbiome in PD: evidence for overabundance of opportunistic pathogens," *npj Parkinson's Disease,* vol. 6, no. 1, 2020, doi: 10.1038/s41531-020-0112-6.

[230] F. Calahorro and M. Ruiz-Rubio, "Caenorhabditis elegans as an experimental tool for the study of complex neurological diseases: Parkinson's disease, Alzheimer's disease and autism spectrum disorder," *Invertebrate Neuroscience,* vol. 11, no. 2, pp. 73-83, 2011, doi: 10.1007/s10158-011-0126-1.

[231] J. F. Cooper and J. M. Van Raamsdonk, "Modeling Parkinson's Disease in C. elegans," *Journal of Parkinson's Disease,* vol. 8, no. 1, pp. 17-32, 2018, doi: 10.3233/jpd-171258.

[232] C. D. Link, "C. elegans models of age-associated neurodegenerative diseases: Lessons from transgenic worm models of Alzheimer's disease," *Experimental Gerontology,* vol. 41, no. 10, pp. 1007-1013, 2006, doi: 10.1016/j.exger.2006.06.059.

[233] J. G. White, E. Southgate, J. N. Thomson, and S. Brenner, "The structure of the nervous system of the nematode Caenorhabditis elegans," *Philos Trans R Soc Lond B Biol Sci,* vol. 314, no. 1165, pp. 1-340, Nov 12 1986, doi: 10.1098/rstb.1986.0056.

[234] M. Naoi and W. Maruyama, "Cell death of dopamine neurons in aging and Parkinson's disease," *Mech Ageing Dev,* vol. 111, no. 2-3, pp. 175-88, Nov 1999, doi: 10.1016/s0047-6374(99)00064-0.

[235] J. Sulston, M. Dew, and S. Brenner, "Dopaminergic neurons in the nematode Caenorhabditis elegans," *J Comp Neurol,* vol. 163, no. 2, pp. 215-26, Sep 15 1975, doi: 10.1002/cne.901630207.

[236] C. H. Lai, "Identification of Novel Human Genes Evolutionarily Conserved in Caenorhabditis elegans by Comparative Proteomics," *Genome Research,* vol. 10, no. 5, pp. 703-713, 2000, doi: 10.1101/gr.10.5.703.

[237] A. Gaeta, K. Caldwell, and G. Caldwell, "Found in Translation: The Utility of C. elegans Alpha-Synuclein Models of Parkinson's Disease," *Brain Sciences,* vol. 9, no. 4, p. 73, 2019, doi: 10.3390/brainsci9040073.

[238] E. J. Lee *et al.*, "Alpha-synuclein activates microglia by inducing the expressions of matrix metalloproteinases and the subsequent activation of protease-activated receptor-1," *J Immunol,* vol. 185, no. 1, pp. 615-23, Jul 1 2010, doi: 10.4049/jimmunol.0903480.

[239] J. Levin *et al.*, "Increased alpha-synuclein aggregation following limited cleavage by certain matrix metalloproteinases," *Exp Neurol,* vol. 215, no. 1, pp. 201-8, Jan 2009, doi: 10.1016/j.expneurol.2008.10.010.

[240] M. R. H. Krebs, L. A. Morozova-Roche, K. Daniel, C. V. Robinson, and C. M. Dobson, "Observation of sequence specificity in the seeding of protein amyloid fibrils," *Protein Science,* vol. 13, no. 7, pp. 1933-1938, 2004, doi: 10.1110/ps.04707004.

[241] A. L. Mahul-Mellier *et al.*, "Fibril growth and seeding capacity play key roles in α-synuclein-mediated apoptotic cell death," *Cell Death & Differentiation,* vol. 22, no. 12, pp. 2107-2122, 2015, doi: 10.1038/cdd.2015.79.

[242] A. K. Paravastu, I. Qahwash, R. D. Leapman, S. C. Meredith, and R. Tycko, "Seeded growth of -amyloid fibrils from Alzheimer's brain-derived fibrils produces a distinct fibril structure," *Proceedings of the National Academy of Sciences,* vol. 106, no. 18, pp. 7443-7448, 2009, doi: 10.1073/pnas.0812033106.

[243] H. Schägger, "Tricine–SDS-PAGE," *Nature Protocols,* vol. 1, no. 1, pp. 16-22, 2006/06/01 2006, doi: 10.1038/nprot.2006.4.

[244] R. Khurana *et al.*, "Mechanism of thioflavin T binding to amyloid fibrils," *Journal of Structural Biology,* vol. 151, no. 3, pp. 229-238, 2005, doi: 10.1016/j.jsb.2005.06.006.

[245] T. Ban and Y. Goto, "Direct observation of amyloid growth monitored by total internal reflection fluorescence microscopy," *Methods Enzymol,* vol. 413, pp. 91-102, 2006, doi: 10.1016/S0076-6879(06)13005-0.

[246] C. Xue, T. Y. Lin, D. Chang, and Z. Guo, "Thioflavin T as an amyloid dye: fibril quantification, optimal concentration and effect on aggregation," *Royal Society open science,* vol. 4, no. 1, p. 160696, 2017.

[247] T. Stiernagle, *WormBook: The Online Review of C. elegans Biology* (Maintenance of C. elegans). University of Minnesota, Minneapolis, MN, 55455, USA: Caenorhabditis Genetics Center, 2006.

[248] J. S. Duerr, "Immunohistochemistry," *WormBook,* pp. 1-61, Jun 19 2006, doi: 10.1895/wormbook.1.105.1.

[249] L. Breimann, F. Preusser, and S. Preibisch, "Light-microscopy methods in C. elegans research," *Current Opinion in Systems Biology,* vol. 13, pp. 82-92, 2019, doi: 10.1016/j.coisb.2018.11.004.

[250] J. K. Heppert *et al.*, "Comparative assessment of fluorescent proteins for in vivo imaging in an animal model system," *Molecular Biology of the Cell,* vol. 27, no. 22, pp. 3385-3394, 2016, doi: 10.1091/mbc.e16-01-0063.

[251] T. Kuwahara *et al.*, "Familial Parkinson Mutant α-Synuclein Causes Dopamine Neuron Dysfunction in Transgenic Caenorhabditis elegans*," *Journal of Biological Chemistry,* vol. 281, no. 1, pp. 334-340, 2006, doi: 10.1074/jbc.m504860200.

[252] T. Kuwahara *et al.*, "A systematic RNAi screen reveals involvement of endocytic pathway in neuronal dysfunction in α-synuclein transgenic C . elegans," *Human Molecular Genetics,* vol. 17, no. 19, pp. 2997-3009, 2008, doi: 10.1093/hmg/ddn198.

[253] M. Lakso *et al.*, "Dopaminergic neuronal loss and motor deficits in Caenorhabditis elegans overexpressing human α-synuclein," *Journal of Neurochemistry,* vol. 86, no. 1, pp. 165-172, 2004, doi: 10.1046/j.1471-4159.2003.01809.x.

[254] N. Li, R. Zhao, Y. Sun, Z. Ye, K. He, and X. Fang, "Single-molecule imaging and tracking of molecular dynamics in living cells," *National Science Review,* vol. 4, no. 5, pp. 739-760, 2017, doi: 10.1093/nsr/nww055.

[255] T. J. Van Ham, K. L. Thijssen, R. Breitling, R. M. W. Hofstra, R. H. A. Plasterk, and E. A. A. Nollen, "C. elegans Model Identifies Genetic Modifiers of α-Synuclein Inclusion Formation During Aging," *PLoS Genetics,* vol. 4, no. 3, p. e1000027, 2008, doi: 10.1371/journal.pgen.1000027.

[256] R. Nass, D. H. Hall, D. M. Miller, and R. D. Blakely, "Neurotoxin-induced degeneration of dopamine neurons in Caenorhabditis elegans," *Proceedings of the National Academy of Sciences,* vol. 99, no. 5, pp. 3264-3269, 2002, doi: 10.1073/pnas.042497999.

[257] B. Altincicek *et al.*, "Role of matrix metalloproteinase ZMP-2 in pathogen resistance and development in Caenorhabditis elegans," (in eng), *Dev Comp Immunol,* vol. 34, no. 11, pp. 1160-9, Nov 2010, doi: 10.1016/j.dci.2010.06.010.

[258] M. Fischer, E. Fitzenberger, R. Kull, M. Boll, and U. Wenzel, "The zinc matrix metalloproteinase ZMP-2 increases survival of Caenorhabditis elegans through interference with lipoprotein absorption," *Genes & Nutrition,* vol. 9, no. 4, 2014, doi: 10.1007/s12263-014-0414-6.

[259] K. Wada, H. Sato, H. Kinoh, M. Kajita, H. Yamamoto, and M. Seiki, "Cloning of three Caenorhabditis elegans genes potentially encoding novel matrix metalloproteinases," *Gene,* vol. 211, no. 1, pp. 57-62, 1998, doi: 10.1016/s0378-1119(98)00076-6.

APPENDIX A

Content for Chapter 2 was taken from:

S. Kamboj, C. Harms, L. Kumar, D. Creamer, C. West, J. Klein-Seethatraman, S. Sarkar, "A method of purifying alpha-synuclein in E. coli without chromatography," *Heliyon,* vol. 7, no. 1, p. e05874, 2021/01/01/ 2021, doi: https://doi.org/10.1016/j.heliyon.2020.e05874.

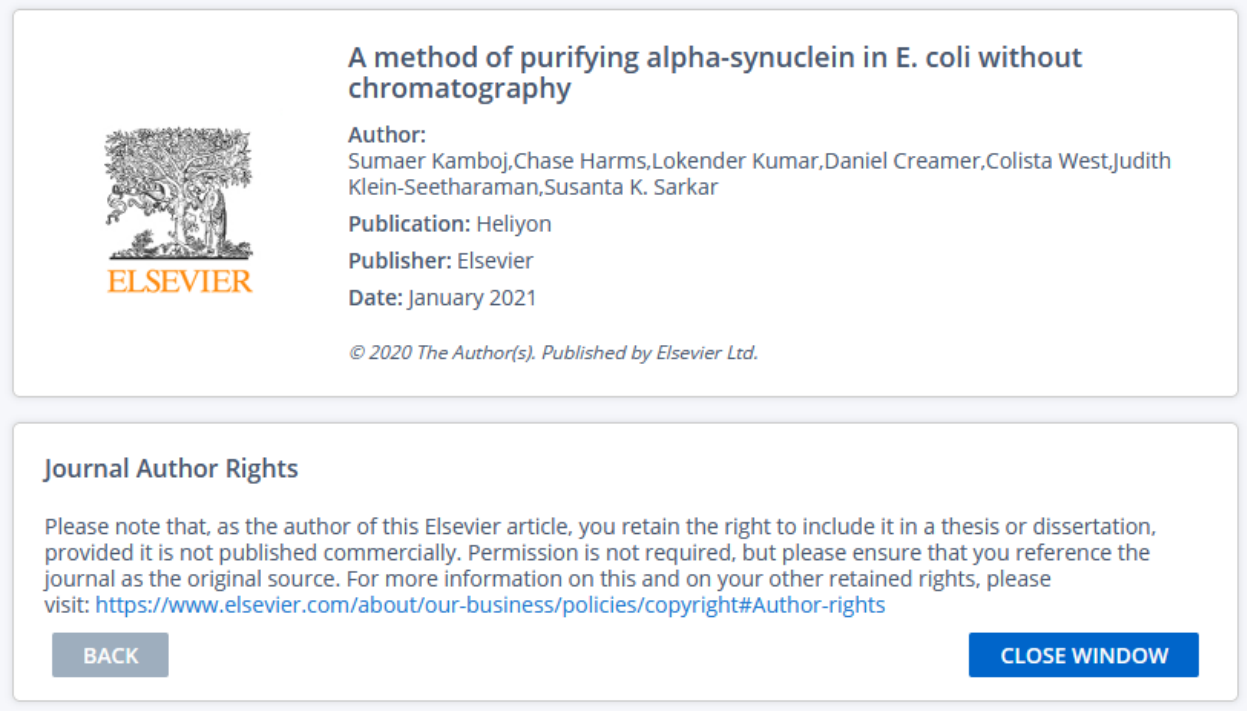

A method of purifying alpha-synuclein in E. coli without chromatography

Author:
Sumaer Kamboj,Chase Harms,Lokender Kumar,Daniel Creamer,Colista West,Judith Klein-Seetharaman,Susanta K. Sarkar

Publication: Heliyon

Publisher: Elsevier

Date: January 2021

© 2020 The Author(s). Published by Elsevier Ltd.

Journal Author Rights

Please note that, as the author of this Elsevier article, you retain the right to include it in a thesis or dissertation, provided it is not published commercially. Permission is not required, but please ensure that you reference the journal as the original source. For more information on this and on your other retained rights, please visit: https://www.elsevier.com/about/our-business/policies/copyright#Author-rights

BACK

CLOSE WINDOW